

University of Denver

Digital Commons @ DU

---

Electronic Theses and Dissertations

Graduate Studies

---

2020

## Ultrasonic-Based Condition Assessment of Wooden Utility Poles

Yishi Lee

*University of Denver*

Follow this and additional works at: <https://digitalcommons.du.edu/etd>



Part of the [Electrical and Computer Engineering Commons](#), [Mechanical Engineering Commons](#), and the [Structural Materials Commons](#)

---

### Recommended Citation

Lee, Yishi, "Ultrasonic-Based Condition Assessment of Wooden Utility Poles" (2020). *Electronic Theses and Dissertations*. 1788.

<https://digitalcommons.du.edu/etd/1788>

This Dissertation is brought to you for free and open access by the Graduate Studies at Digital Commons @ DU. It has been accepted for inclusion in Electronic Theses and Dissertations by an authorized administrator of Digital Commons @ DU. For more information, please contact [jennifer.cox@du.edu](mailto:jennifer.cox@du.edu), [dig-commons@du.edu](mailto:dig-commons@du.edu).

Ultrasonic-based Condition Assessment of Wooden Utility Poles

---

A Dissertation

Presented to

the Faculty of the Daniel Felix Ritchie School of

Engineering and Computer Science

University of Denver

---

In Partial Fulfillment

of the Requirements for the Degree

Doctor of Philosophy

---

by

Yishi Lee

December 2020

Advisor: Mohammad H. Mahoor, Ph.D.

Author: Yishi Lee  
Title: Ultrasonic-based Condition Assessment of Wooden Utility Poles  
Advisor: Mohammad H. Mahoor, Ph.D.  
Degree Date: December 2020

## Abstract

More than 300 million utility poles shoulder the utility grid in the United States. However, the ineffectiveness of the current inspection process causes roughly a third of utility poles removed from the service deemed suitable for reuse. Due to the utterly essential role of the power infrastructure, budget shrinkage, and the structural degradation of the modern distribution grid, this Ph.D. dissertation addresses the challenges by proposing a physics-based signal analysis method with a jointly developed ultrasonic UB1000 system<sup>©</sup> to enhance the objectivity in ultrasonic-based nondestructive evaluation (NDE). The proposed methodology has been deployed commercially in the field and featured in articles by the Missouri Public Utility Alliance and the Western Cooperative Electric.

This dissertation proposes embedded waveguide as an ultrasonic radiation source. A systematic analytical model is developed based on the classical elastodynamic formulation to study the excitation and the propagation characteristics of the resulted elastic wave. Based on the steady-state assumption with a set of half-space boundary and interface loading conditions, the obtained closed-form displacement field yields the diffusive property of the shell region propagation as a function of the Poisson's ratio. The diffusive property is discovered under the quasi-steady load condition, a reasonable model to describe the behavior of a narrow-band ultrasonic transducer. The estimated diffusive propagation is demonstrated through the numerical finite element method (FEM).

This study developed the first high-fidelity numerical model of a wooden pole cross-sectional region. It is capable of modeling a porous orthotropic medium under the cylin-

drical symmetry enabling high moisture content and/or incipient decay conditions to be simulated. Using a transient imposed boundary condition, the model uncovers different arrival wave modes resulted from propagating in various regions within the cross-section. By dissecting the waveform and isolating the corresponding arrival wave, it allows a direct examination of the wave energy content within the shell region, which is a critical area in the cross-section that dictates the overall strength of a wooden pole. By modifying the physical and the poroelastic properties of the medium to simulate the incipient decay and high moisture content, this study discovers a correlation between the selected features within the received waveform and the physical property of the medium (e.g., modulus of elasticity and the moisture saturation levels).

The findings from both the numerical and analytical approaches motivate the proposed physics-based signal analysis to extract both the temporal and spectral information at the resonant frequency of the ultrasonic wave via the time and frequency (TF) transformation. A comparative study using the numerical results was performed to examine the *Short Time Fourier Transformation* (STFT) and *Gabor Continuous wavelet transform* (GCWT). Due to its superior temporal and spectral resolution, the GCWT is selected to analyze signals from different simulated conditions. The results produce a pronounced difference in the selected features in all the different simulated cases, suggesting a viable analysis approach for characterizing the medium.

Based on the proposed physics-based signal analysis approach, this work develops and details a corresponding pole analysis algorithm. The experiments were carried out with specimens of different known *Groundline* (GL) conditions (healthy, decay and high-moisture) to examine the efficacy of the proposed waveguide design and the associated analysis algorithm. The collected signals are fed through the GCWT analysis algorithm to extract the features sensitive to those conditions. The results suggest a high moisture content pole would have a typical energy attenuation of around 35% compared to a healthy



pole with low moisture content, while the time when the peak energy occurs is relatively the same in both cases. In a decay wood specimen, the result suggests an 11% latency in peak energy *time-of-flight* (TOF), 50% energy reduction and a 50% increase in diffusivity by measuring the full width half maximum (FWHM) around the energy peak. A further refinement of the analysis places the peak energy TOF and energy reduction levels as the selected features on a feature space to assess fifteen poles with known categories. A clear decision boundary is discovered prompting a future research opportunity of using linear and/or non-linear classifiers to determine the wooden pole at the GL region.

# Acknowledgements

The journey of pursuing a Ph.D. degree has been the most difficult but the most rewarding one. Coming to the program as a naive master student hoping that Ph.D. will be the same as a master degree, I was utterly wrong. Being a scholar in the field of science and engineering demands a tremendous amount of commitment, perseverance, patience, and a certain amount of luck. As I recall a quote from one of my formal faculty advisors, "if you don't dream about your research at night, you are not doing your Ph.D. right.". On top of that, you will constantly be asked by your peers, "when are you graduating?". On the other hand, for someone who entered a Ph.D. program is able to make it out in one piece, and you will come out with a transformation of more profound understanding and respect to the true scale of a rigorous scientific and engineering endeavor.

I want to dedicate this to my mom for her sacrifice and devotion. I also want to thank my advisor, Professor Mohammad Mahoor, for the encouragement and trust in my ability. Without his dedication to graduate student research, this work will never come to fruition. I also want to thank the industrial partner "Utility Asset Management Inc." and the Industry-University Cooperative Research Centers (IUCRC) at the University of Denver, who supported this research financially by providing the equipment, data, and funding for this work. The Ph.D. committee is a non-separable component of the Ph.D. degree process. I have been fortunate enough to have outstanding committee supports to ensure the review process was performed with the highest professionalism possible. Hence, I want to give my sincere thanks to my committee, Professor Mohammad Mahoor, Professor Peter Laz, Professor Mohammad Abdul Matin, and Professor Douglas Allen for their invaluable service. I want to finally thank the University of Denver for creating an academically challenging and nurturing environment for all our graduate students.

# Table of Contents

<b>List of Abbreviations</b>		<b>xiv</b>
<b>1 Introduction</b>		<b>1</b>
1.1 Purpose . . . . .		1
1.1.1 Shell Region Inspection . . . . .		2
1.1.2 Subsurface Narrow-band Excitation . . . . .		4
1.1.3 Physics-based Signal Analysis . . . . .		5
1.2 Outline of Dissertation . . . . .		5
1.3 Contributions . . . . .		6
<b>2 Background and Literature Review</b>		<b>8</b>
2.1 Background of Wooden Utility Poles . . . . .		10
2.1.1 Hierarchical View of Wood and Porosity . . . . .		13
2.1.2 Brief Overview of Decay Fungi . . . . .		15
2.1.3 Preparation and Preservatives . . . . .		19
2.2 Literature Review of Ultrasonic-based Evaluation . . . . .		21
2.2.1 Wave Pattern . . . . .		22
2.2.2 Elastodynamics Model . . . . .		25
2.2.3 Hardware Implementation . . . . .		26
2.2.4 Signal Processing . . . . .		35
<b>3 Estimation of Half-space and Subsurface Excitation</b>		<b>37</b>
3.1 Electrodynamics in Isotropic Medium . . . . .		37
3.2 Formulation of Diffusive Propagation . . . . .		40
3.2.1 Half-space Response . . . . .		42
3.2.2 Subsurface Response . . . . .		46
3.3 Numerical Plane Geometry Model . . . . .		48
3.3.1 Model Environment . . . . .		49
3.3.2 Diffusive Propagation . . . . .		50
3.3.3 Poisson’s Ratio Dependency . . . . .		53
3.3.4 Steady-State Waveguide Estimation. . . . .		54
3.4 Field Approximation under the Quasi-steady Limit . . . . .		57
3.4.1 Transient Response of Langevin Transducer . . . . .		58
3.4.2 The Spatial and Poisson’s Ratio Dependencies . . . . .		62
3.4.3 Dual Waveguide Estimation of Transient Wave . . . . .		64
3.5 Summary and Discussion . . . . .		65

<b>4</b>	<b>Numerical Model of the Orthotropic Porous Medium</b>	<b>68</b>
4.1	Numerical Model of Orthotropic Medium . . . . .	69
4.1.1	Constitutive Equation of Motion . . . . .	69
4.1.2	Forcing Boundary . . . . .	70
4.1.3	Effective Properties and Computation Upscaling . . . . .	71
4.1.4	Time stepping and Numerical Stability . . . . .	72
4.1.5	Case Study: Time Domain Analysis . . . . .	73
4.1.6	Case Study: Variations in Mechanical Properties . . . . .	80
4.2	The Poroelastic Formulation . . . . .	81
4.2.1	Case Study: Unsaturated vs. Saturated Porous Matrices . . . . .	84
4.2.2	Case Study: Variations in Porosity . . . . .	85
4.3	Summary and Discussion . . . . .	87
<b>5</b>	<b>Holistic Signal Synthesis</b>	<b>89</b>
5.1	TF Domain Representation . . . . .	89
5.1.1	Short-time Fourier Transform . . . . .	90
5.1.2	Continuous Gabor Wavelet Transformation . . . . .	92
5.2	Model-based Signal Analysis . . . . .	94
5.3	Case Study: Cylindrical Medium Without Attenuation . . . . .	96
5.4	Case Study: Cylindrical Medium with Viscous Damping . . . . .	99
5.5	Proposed Algorithm . . . . .	102
5.6	Summary and Discussion . . . . .	102
<b>6</b>	<b>Empirical Study of Proposed Techniques</b>	<b>105</b>
6.1	A Brief Description of the UB1000 System . . . . .	106
6.1.1	Embedded Waveguide . . . . .	107
6.2	Signal From a Healthy Wooden Utility Pole . . . . .	108
6.3	Effects of Saturated and Unsaturated Media . . . . .	113
6.3.1	Preparation and Procedures . . . . .	113
6.3.2	T-F Domain Analysis . . . . .	114
6.4	Effects of Mechanical Degradation . . . . .	116
6.4.1	NESC Standard for Shell Rot . . . . .	118
6.4.2	Preparation and Procedures . . . . .	119
6.4.3	TF Domain Analysis . . . . .	119
6.5	Possible Classification of the Selected Features . . . . .	128
6.6	Summary and Discussion . . . . .	130
<b>7</b>	<b>Conclusions and Future Work</b>	<b>132</b>
7.1	Concluding Remarks . . . . .	132
7.2	Contributions Summary of this work . . . . .	133
7.3	Future Work . . . . .	137
7.3.1	Contact-based Ultrasonic Waveguide Excitation . . . . .	137
7.3.2	Narrow-band vs. broad-band analysis . . . . .	139

7.3.3	Analytical Formulation of Transient Poroelastic Wave . . . . .	139
7.3.4	Signal Decomposition and Arrival Wave Identification . . . . .	140
7.3.5	Ray Tracing and Tomographic Inversion . . . . .	141
7.3.6	Nonseparable Pattern Classification . . . . .	142

**Bibliography** **143**

**APPENDICES**

A	Navier’s Equation for Elastic Model . . . . .	157
B	GL Signal Consistency Study . . . . .	160

# List of Tables

4.1	Entries of the Christoffel acoustic tensor (Lee et al., 2020). . . . .	70
4.2	Maximum element size for each species in order to employ the computational upscaling technique (Lee et al., 2020). . . . .	72
4.3	The arrival time of the different wave modes . . . . .	79
4.4	Parameters describing the poroelastic medium . . . . .	84
4.5	Estimated parameters of an attenuation regression model between the unsaturated and moisture saturated medium . . . . .	85
4.6	Parameter estimation of power regression of different porosity values . . . .	87
6.1	Time of flight (TOF) and peak energy information from the empirical signal.	113
6.2	The energy attenuation and the time-of-flight (TOF) between Pole A (low moisture) and Pole C (high moisture). . . . .	117
6.3	Extracted TOFs and peak energy levels between an healthy pole (16529) and a suspected shell rot pole (16530) . . . . .	126
6.4	A comparative result between the hardness test and the resultant TF domain analysis . . . . .	130

# List of Figures

2.1	An example of a resistor graph and empirical correlation to density (Isik and Li, 2003) . . . . .	10
2.2	An illustration of the pole structure . . . . .	11
2.3	Pole failure location with respect to the ground level at zero. Figure was extracted from (Sandoz and Vanackere, 1997). . . . .	12
2.4	A loading zone of utility poles in the United States . . . . .	13
2.5	Hierarchical order of a wooden structure (Bucur, 2006). . . . .	15
2.6	Enlarged view of fibers in Douglas-fir (Morrell, 2012). . . . .	16
2.7	Cell structure (Haygreen et al., 1996). . . . .	17
2.8	Mechanical properties of the cell walls obtained from the nanoidentation technique. (Gindl et al., 2004). . . . .	18
2.9	The composition of the removal due to various circumstances (Morrell et al., 2006) . . . . .	18
2.10	Relative decay risk in the United States divided by region (1 = low risk, 5 = high risk)(Morrell, 2008) . . . . .	19
2.11	Empirical result of the relations between MOE, MOR and weight loss (%) (Winandy and Morrell, 1993). . . . .	20
2.12	Process for impregnation of preservatives into wood. . . . .	21
2.13	Experimental result of modulus of elasticity versus velocity squared. (Sandoz, 1989) . . . . .	23
2.14	Experimental set up using pulse-echo technique (Bucur and Böhnke, 1994) . . . . .	24
2.15	Dilatational wave motion produced by (Senalik, 2013) column 1 and (Payton, 2003) in column 2 at a) 43 $\mu$ s, b) 116 $\mu$ s, c) 129 $\mu$ s and d) 172 $\mu$ s . . . . .	26
2.16	Alignment of the domain displacement before and after a poling treatment is applied. (Gallego-Juarez, 1989) . . . . .	28
2.17	Piezoelectric resonance modes and the corresponding coupling factors(Uchino, 2012), the shaded areas are the applied electric field. . . . .	29
2.18	Piezoelectric properties of typical PZTs (Uchino, 2012) . . . . .	31
2.19	Piezoelectric properties of typical PZTs (Gallego-Juarez, 1989) . . . . .	31
2.20	A sectional view of a Langevin transducer (Gallego-Juarez, 1989) . . . . .	32
2.21	A simplified circuit diagram of the power stage circuit(Salazar et al., 2003) . . . . .	33
3.1	A simplified diagram of the problem. . . . .	41
3.2	Diffusive relation between wavenumber of the fast and slow modes and the Poisson's ratio . . . . .	45
3.3	Simulation Geometry using COMSOL. . . . .	50
3.4	A piece-wise forcing function creating quasi-stable oscillation . . . . .	51

3.5	Simulated steady-state with $W$ mode propagation in (a) and $U$ mode propagation in (b). . . . .	52
3.6	Placements of the displacement probes represented by the red dots. . . . .	53
3.7	$W$ displacement fields measured at a) 50 mm, b) 100 mm and c) 200 mm from the source. . . . .	54
3.8	$U$ displacement fields measured at a) 50 mm, b) 100 mm and c) 200 mm from the source . . . . .	55
3.9	$W$ displacement field at the half-space with different $\nu$ values. . . . .	56
3.10	$U$ displacement field at the half-space with different $\nu$ values. . . . .	56
3.11	Two waveguide configuration. . . . .	57
3.12	The waveguide response compared to the ideal response of the half-space displacement. . . . .	58
3.13	a) Design schematic of Langvin transducer. b) Exposed view of a manufactured Langvin transducer. (Cochran et al., 2012). . . . .	60
3.14	Time transient response of a pizeoelectric plate (Cochran et al., 2012). . . . .	61
3.15	An illustration of the insertable waveguide. . . . .	61
3.16	Spectral Response of the waveguide . . . . .	62
3.17	a) Temporal and b) spectral responses of the waveguide with $\nu = 0.4$ . . . . .	64
3.18	A comparison of the measured amplitudes between the steady-state and quasi-steady excitation mode with $\nu = 0.4$ . . . . .	65
3.19	A comparison of the measured waveforms between the steady-state and quasi-steady excitation mode with $\nu = 0.4$ . . . . .	66
3.20	Transient response estimation of the waveguide. Subplot a and c show the ideal waveform in both temporal and spectral domains. Subplot b and d shows the waveform estimation using the proposed embedded waveguide design. . . . .	67
4.1	Geometry of the problem. . . . .	70
4.2	Homogeneity and convergence of physical properties from Douglas-fir (Lee et al., 2020). . . . .	72
4.3	Relative error of different step sizes (Lee et al., 2020). . . . .	74
4.4	Imposed transient response to simulate a typical narrow-band ultrasonic transducer . . . . .	74
4.5	Magnitude of the displacement fields at a) orthotropic medium where the dotted white lines denote the beam width boundary and the white arrow denotes the energy vector. b) Isotropic medium using average properties. . . . .	76
4.6	Received time-domain signal with the corresponding states of wave propagation at a) $t = 360$ us, b) $t = 560$ us and c) $t = 890$ us. (Lee et al., 2020) . . . . .	78
4.7	Received time-domain signal with the corresponding states of wave propagation at a) $t = 360$ us, b) $t = 560$ us and c) $t = 890$ us. (Lee et al., 2020) . . . . .	79
4.8	An excerpt illustrating the correlations between decay on various mechanical properties (Curling et al., 2002). . . . .	80



4.9	A comparative result of waveforms between healthy pole and pole with simulated incipient decay. . . . .	82
4.10	A comparison of the energy attenuation rates between the unsaturated and moisture saturated medium . . . . .	85
4.11	A scanning electron micrograph of wood that has been decayed by white rot (Blanchette et al., 2004). . . . .	86
4.12	Spectral response of the received signal under different porosity . . . . .	87
5.1	An overlapped Blackman window.(Zhivomirov et al., 2019) . . . . .	91
5.2	Illustration of process work flow of the STFT. (Zhivomirov et al., 2019) . . . . .	91
5.3	An example of the STFT resolution scheme. . . . .	92
5.4	An example of the Wavelet resolution scheme. . . . .	94
5.5	Relating physical properties to the TF domain analysis. . . . .	95
5.6	Temporal response. . . . .	97
5.7	STFT vs. Gabor Wavelet, a) STFT with $\nu = 0.2$ , b) STFT with $\nu = 0.4$ , c) Gabor wavelet with $\nu = 0.2$ and d) Gabor wavelet with $\nu = 0.4$ . . . . .	97
5.8	Time domain responses at the resonance at 50 kHz using the a) Gabor CWT and b) STFT . . . . .	98
5.9	Waveform with an imposed viscous damping . . . . .	99
5.10	Waveform with an imposed viscous damping . . . . .	100
5.11	Time domain energy response at 50 kHz, with imposed viscous damping to simulate energy attenuation using a) STFT transformation and b) Gabor CWT transformation . . . . .	101
5.12	Flow chart of the algorithm . . . . .	103
6.1	Overall internal view of the UB1000 (Hall et al., 2020) . . . . .	107
6.2	Flow diagram of the main circuit. . . . .	107
6.3	The physical layout of the entire UB1000 system . . . . .	108
6.4	Waveguide (Lee and Hall, 2020). . . . .	109
6.5	Waveguide Spectral Response. . . . .	109
6.6	An image of the 40-inch circumference pole and the raw signal obtained by the UB1000 system, courtesy of UAM. . . . .	110
6.7	The Gabor domain representation of the a) simulated signal and b) GL signal. . . . .	112
6.8	Illustration of the experimental setup to examine the moisture effects on the acoustic signal response. . . . .	114
6.9	Images of the experimental setup a) front view of pole A, b) a view of the GL level of pole A with two UB1000 probes mounted, c) front view of pole C and d) a view of the GL level of pole C with two UB1000 probes mounted. . . . .	115
6.10	ADC filtered values. . . . .	116
6.11	Wavelet domain. . . . .	117
6.12	Temporal response at 60 kHz . . . . .	118
6.13	Shell Rot Demonstration. . . . .	120
6.14	NESC standard for shell rot. . . . .	121

6.15	Two UB1000 at the GL region of the two selected poles and their geographical locations provided by (Hall, 2016). . . . .	122
6.16	Raw ADC signal generated by the UB1000. . . . .	123
6.17	T-F domain representation of Pole ID: 16529. a) Gabor wavelet domain representation and b) temporal response at the resonant frequency. . . . .	125
6.18	T-F domain representation of Pole ID: 16530. a) Gabor wavelet domain representation and b) temporal response at the resonant frequency. . . . .	126
6.19	Feature comparison of the different arrival wavemode between the two cases. a) and c) are the TF representation of pole ID 16529. b) and d) are the TF representation of Pole ID 16530. . . . .	127
6.20	Temporal response at the resonance for pole 16530 (Marginal Pass) and 16529 (OK) . . . . .	128
6.21	A feature plot of the extracted features and their resulted designation from the described expert assessment. . . . .	130
7.1	An example application using contact-based waveguide excitation with the UB1000 system . . . . .	138
7.2	Tomographic Inversion using the UB1000 system (Hall, 2016). . . . .	142
B.1	Test Configuration from a) the top view and b) the actual setup. . . . .	161
B.2	Results from 10 different measurements. . . . .	163
B.3	Temporal energy response from a) 90-270 and b) 0-180 . . . . .	164

# List of Abbreviations

- ACU** air-coupled ultrasonic. 34
- ADC** analog-to-digital converter. 106, 108, 114
- ASA** Acoustical Society of America. 136
- AU** acousto-ultrasonic. 23
- AWT** analytic wavelet transformation. 93
- BDF** backward differentiation formula. 70
- CT** computed tomography. 8, 24
- CWT** continuous wavelet transform. xii, 94, 98, 100–102
- DAE** differential algebraic equation. 48, 49, 70
- DC** direct current. 106
- DFT** discrete Fourier transform. 90
- EAR** expected arrival region. 102
- EOM** equation of motion. 37, 38, 40, 87, 139
- FEM** finite element method. ii, 25, 59, 108, 133, 134
- FWHM** full width half maximum. iv, 65, 78, 79, 81, 102, 127, 128, 133, 137
- GCWT** Gabor continuous wavelet transform. iii
- GL** groundline. iii, iv, viii, xii, xiii, 6, 11, 34, 71, 88, 95, 101, 102, 108, 112, 114, 119, 122, 128, 129, 131, 132, 134, 136, 139, 160, 162
- MFA** microfibril angle. 14
- MOE** modulus of elasticity. x, 17, 20, 80, 137
- MOL** method of line. 49, 70
- MOR** modulus of rupture. x, 17, 20, 80, 137
- MOSFET** metal-oxide semiconductor field-effect transistor. 33

**NDE** ultrasonicbased nondestructive evaluation. ii, 3, 5, 9, 21, 89

**NESC** national electric safety code. vii, xii, 118, 119, 121, 128, 129, 131, 135, 141, 142

**NR** normalized ratio. 77

**PDE** partial differential equation. 73

**PML** perfectly matched layer. 49

**PZT** lead zirconate titanate. 30, 31, 41

**RMS** root mean square. 24, 35

**Rx** Receiving. 106

**SNR** signal-to-noise. 102, 109, 114, 121

**STFT** short time Fourier transformation. iii, xii, 89–92, 96–102

**SVM** support vector machine. 4, 5

**TC** time centroid. 36

**TF** time and frequency. iii, vii, xiii, 5, 24, 89, 94, 95, 100, 105, 111, 119, 121, 124, 127, 133, 135, 142

**TOF** time-of-flight. iv, ix, 22, 35, 77, 79, 94, 111, 113–115, 117, 124–130, 133, 135, 160, 162

**Tx** Transmission. 106

**UAM** Utility Asset Management Inc.. 26

**USDA** U.S. Department of Agriculture. 69

**WOM** work to maximum load. 80

# Chapter 1

## Introduction

### 1.1 Purpose

The United States uses about 300 million wooden poles to support two of the most critical infrastructures: power and communication distribution networks. Their structural integrity poses a vital concern for the sustainability of the system. Its undeniable importance demands a rigorous life-cycle monitoring program to prevent unexpected structural failure that could incur costly unplanned maintenance and repair work (Bodig et al., 1982). In 2013, data collected by the Oregon State University suggested the average service life of a wood pole is far beyond the initial estimate of 30 to 40 years due to the improvement in the quality of wooden utility poles. Data even suggested that an average pole service life could easily reach 80 years in many areas (Morrell, 2008) and (Datla and Pandey, 2006). The current inspection process for determining a pole condition results in over a third of removed poles are deemed to be in good structural condition for service, causing the utility companies roughly 9 billions of dollars annually. This wasteful consequence suggests inadequacies in the current inspection, and it presents the opportunity for an improved assessment process with better accuracy and consistency.

The traditional inspection technique relies primarily on drilling and resistance micro-drilling (Bhuyan, 1998) and (Morrell et al., 1996). These processes drill into the structure to extract the wood fibers. Although it is a direct method of assessing the internal condition, the removal of material can inadvertently damage the previously established internal chemical and physical balances. This process is termed *destructive evaluation*. Investigations into the use of non-destructive evaluation have piqued many interests in scientific and engineering communities (Galligan, 1964). This study focuses on two immediate concerns surrounding the wooden pole inspections that have not been thoroughly addressed: A detailed exploration of the ultrasonic wave in the shell region using a novel embedded waveguide method and the physics-based signal analysis technique. The following sections will briefly introduce and discuss some of the unsolved issues related to each of the topics.

### **1.1.1 Shell Region Inspection**

Traditional inspection relies heavily on human subjectivity to determine the condition of poles. The traditional process prior to the introduction of nondestructive evaluation has been described in detail by (Morrell, 2012). According to the Rural Utility Service Bulletin 1730B-121 from (Loan and Guarantee, 2006), the initial determination of the pole condition is based on the inspector's personal experience. That includes listening to the sounds and feel of the hammer striking a pole. This process is inevitably subjective, producing a massive variation in terms of the determination of the condition. Due to the importance of the shell region condition to the overall structural integrity of the pole, which will be further discussed in Chapter 2.1, the technique of using a hammer is incapable of resolving the physical condition of the shell region. An improved technique employs shell-thickness indicator (often termed the shell rot gauge) (Morrell, 2012) to determine the surface hardness of the pole. This process disturbs the existing environmental condition at the groundline

region. To mitigate the risk of interrupting the delicate balance while reducing subjectivity, the NDE has been gaining more and more traction in the industry.

Among them, ultrasonic NDE is deemed to be an effective and deployable technology for the field (Goodman and Stewart, 1990). Henceforth, this research will focus on utilizing ultrasonic NDE technology for wooden pole inspection. Pioneers in the ultrasonic elastic inspection primarily focused on the analysis of initial arrival of the wave. By measuring the time difference between the transmission and receiving sensors, the physical properties such as the density and the modulus of elasticity can be inferred (Suzuki et al., 1990). However, this technique only evaluates the region of the shortest distance between the sensors, and the subsequent responses (or arrivals) in the waveform was not thoroughly analyzed and understood. In the early work, a lack of computational power limited the understanding of the wave characteristics in the cross-sectional region to be confined to an analytical model developed by (Payton, 2003). Later, a numerical model was developed by (Senalik et al., 2010) and (Bulleit and Falk, 1985) employing the NDE to characterize the wooden poles by assuming the homogeneous and isotropic medium. Despite the critical role of the physical condition in the shell region, the excitation and propagation characteristics of this region were not thoroughly investigated. The trajectory of elastic wave propagation and how it is related to the complex mechanical properties were not fully explored.

### **Objectives Related to Shell Region Inspection**

This research revisits the first principle of the elastic wave equation to derive the close-form analytical expression of the Rayleigh wave propagation in the shell region. This work systematically explores the embedded waveguide excitation mechanism through analytical formation and numerical estimation. An optimal embedded waveguide design through field experiments is used to verify the findings. The propagation model is assumed to be an orthotropic porous medium based on the Biot's model (Biot, 1956). The associated findings

give a more qualitative and quantitative understanding of the propagation mechanism in wood.

### **1.1.2 Subsurface Narrow-band Excitation**

The ultrasonic signal analysis primarily focuses on broad-band excitation to generate a broad spectral profile. The broad spectral graph produces a dispersive relation that characterizes the physical condition. This is often referred to as the impulse response. While it produces a huge amount of information regarding the physical condition, it is often difficult to analyze. Advanced signal processing techniques such as the pattern classification and *support vector machine* (SVM) were employed (Dackermann et al., 2014). Data-driven algorithms require a large amount of data and reliable labeling techniques. In the utility pole inspection industry, accurate labeling of the pole condition presents a challenge. There is also an issue of emitting consistent ultrasonic wave as the emitting wave depends on the interface condition. The uneven impact surfaces can affect the emission characteristics, especially in the frequency domain, producing artifacts in the dispersive relation that can be difficult to distinguish. This issue presents another challenge when the spectral analysis is deployed (Han and Birkeland, 1992). The energy deposition of the induced surface propagation through the surface impact is normally very shallow (Viktorov, 1967), making the ultrasonic assessment of the shell region ineffective.

#### **Objective of Subsurface Narrow-band excitation**

This research utilizes a narrow-band piezoelectric transducer to generate consistent elastic disturbance. Using the embedded waveguide specifically designed for this project, the ultrasonic elastic wave is generated in the subsurface region of the medium. In turn, this proposed technique eliminates any emission inconsistency and increases the energy



deposition of the surface wave. The result enables the obtained waveform to be analyzed in both temporal and spectral domains.

### **1.1.3 Physics-based Signal Analysis**

Signal analysis is the main part of the NDE. Many studies in this area focus on data-driven pattern classification through SVM or machine learning techniques and empirical data to uncover the underlying features associated with the material characterization (Dackermann et al., 2014). A number of studies have employed similar empirical approach. Based on the issues discussed previously, the integrity of the data and the high variance in the excitation technique can result in unreliable classification results.

#### **Objectives related to Physics-based signal analysis**

The signal analysis is built upon the understanding of the comprehensive formulation for the shell region wave propagation. Employing the TF domain analysis, different arrival wavepackets are identified and analyzed through the continuous wavelet analysis. The result of the analysis provides both mechanical and moisture characteristics of the propagating medium.

## **1.2 Outline of Dissertation**

Chapter 2 outlines the research and development landscape of using NDE wooden utility pole assessments.

Chapter 3 introduces the theoretical formulation of the embedded waveguide excitation technique. This chapter introduces the constitutive equations under the steady-state assumption. It yields theoretical findings that help characterize wave propagation and their

relations to be propagating medium. This analysis is then used as the basis to estimate the time transient model that mimics a typical ultrasonic transducer response.

Chapter 4 describes the implementation of a more precise numerical model containing the wave interaction between the embedded waveguide and the orthotropic porous medium that characterizes wood. The wave mode that dominates the shell region is thoroughly investigated. The sensitivity of different signal characteristics is explored through different simulated scenarios.

Chapter 5 introduces the employed signal analysis technique to help extract the discovered features from Chapter 4. The extracted features are then used to coordinate with the imposed scenarios, including mechanical degradation and high moisture concentration in the porous medium.

Chapter 6 introduces a proposed preparation and procedures to conduct control experiments. Using the developed hardware and proposed signal analysis technique, empirical data are studied to validate the theoretical and numerical model. Further deployment of the algorithm resulted in a feature plot help classify the GL condition.

Chapter 7 gives concluding remarks and suggests further avenues of research related to this work.

## **1.3 Contributions**

Specific contributions of this research are summarized below:

- A novel embedded ultrasonic waveguide capable of emitting subsurface elastic wave disturbance (Chapter 3).
- Detailed analytical investigations of the embedded ultrasonic waveguide excitation under the steady and quasi-steady state limits (Chapter 3).

- A comprehensive numerical model to describe the wave characteristics in the orthotropic and porous medium (Chapter 4).
- Detailed investigation of the Rayleigh mode propagation in the shell region using the proposed embedded waveguide excitation (Chapters 3 and 4).
- Detailed analysis of the wave disturbance estimation using dual waveguide configuration under both Cartesian and cylindrical symmetries (Chapters 3 and 4).
- Discovery of the arrival wave mode and the development of a dedicated signal analysis algorithm (Chapter 5).
- Moisture content and mechanical property determination using scalogram and the extraction of the corresponding features (Chapters 5 and 6).
- Selected features were tested using empirical data, and a clear decision boundary was determined in the proposed feature space. (Chapter 6).

# Chapter 2

## Background and Literature Review

Non-destructive evaluation methods of wooden utility poles are categorized into the following groups: radiographic, chemical, resistograph, thermographic and ultrasound. The radiographic technique uses radioactive source to generate penetrating radiation through the material. As the radioactive photons are ejected from the source, the energy deposition is proportional to the material along the ray trajectory. The first x-ray-based examination was introduced by (Zucker et al., 1940). Over the years, continuous attempts have been made to automate the process from rotating computed tomography (CT) scans to analytical software to derive physical properties based on the radiograph results (Davis et al., 1993) and (Schmoldt et al., 1993). However, systems are normally very heavy and require extensive setup time.

A technique of using the chemical inspection approach was early published by Eslyn (Eslyn, 1970). Chemicals such as bromocresol green and methyl orange, chrome azurol-s create discoloration as an indicator for the presence of rot in a wood specimen. However, this method presents a limitation because it is merely a binary indicator without information about the severity and the size of the decay. It is also limited to surface detection and offers no information about the interior of the pole.

Infrared due to external heating was also examined by remote sensing the radiating infrared signal, thermographic technique was developed to infer physical properties. Most of the work was performed by Wyckhuysse (Wyckhuysse and Maldague, 2001). However, this technique has a number of issues. The low conductivity of wood only allows the infrared to penetrate about 9.5 mm, limiting the detection of internal decay. Extracting information of the moisture content based on the heat signature does not always warrant the decay of wood, as decay occurs when temperature, moisture content and even pressure are at particular levels.

The *resistograph* was introduced by Rinn et al. in 1996 (Rinn et al., 1996). This technique exploits the difference in density between the healthy and decayed wood using a simple drilling device with a small drill bit. Healthy wood and decayed wood have distinct differences in terms of physical properties. The resistance from the counter-torque experiences by the drill bit can be correlated to the material density (Winistorfer et al., 1995). In other words, When a drill bit encounters a healthy wooden medium, which has a higher density than a decayed wood, the removal of denser material corresponds to more mass. It results in an elevated resistance that counteracts the rotational motion generated by the drill. By measuring this counter-torque by a means of the change in electrical load as it penetrates through different regions, the resulted amplitude profile versus the depth of penetration is the resistograph depicted in Fig. 2.1. This technique presents a few limitations. It is required to drill into the heart region of the pole and the examination of the local area does not necessarily correspond to the global condition of the entire region of interest.

This study focuses on the employment of elastic wave propagation to characterize the medium. This technique is often referred to as the ultrasonic-based NDE. It begins by understanding the wooden pole structure, the medium, and the widely accepted decay mechanisms. The current state of the ultrasonic-based NDE will be introduced, including the governing model, the required hardware implementation and the signal analysis schemes.

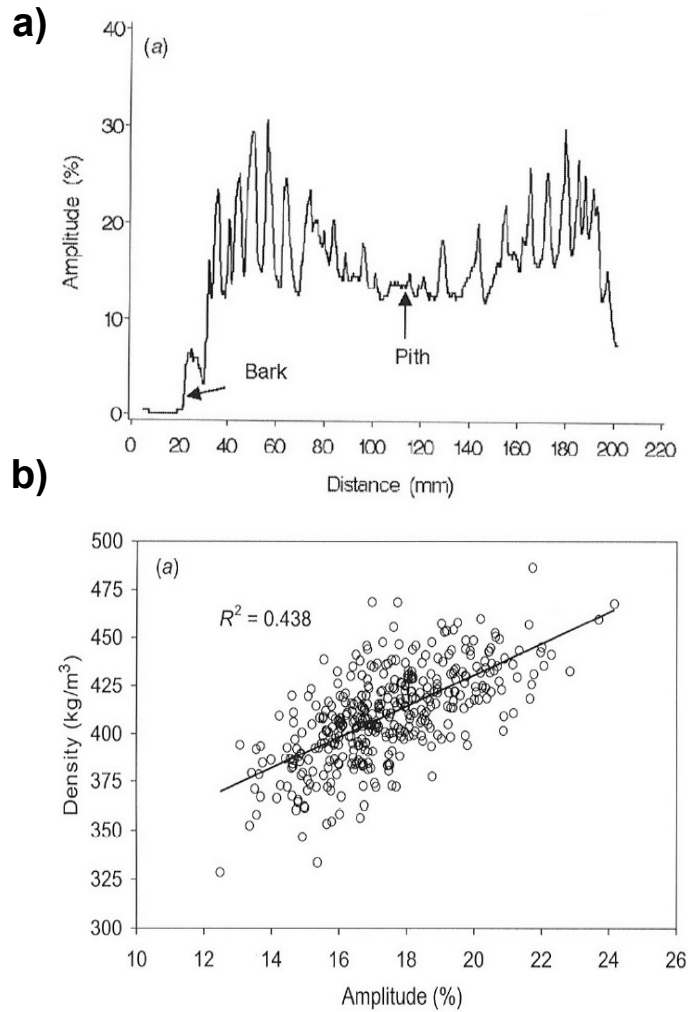


Figure 2.1: An example of a resistor graph and empirical correlation to density (Isik and Li, 2003)

## 2.1 Background of Wooden Utility Poles

Wooden utility poles constitute the majority of all utility poles in the United States (Bolin and Smith, 2011). Based on the standard provided by the United States Department of Agriculture (Wolfe and Moody, 1997), Southern Pine, Douglas Fir, Cedar and Northern Red Pine are the most common species due to their excellent mechanical properties (fiber strength, Young's Modulus etc) that meet or exceed the minimum quality specifications. Wooden utility poles, as depicted in Fig. 2.2, resembles a *cantilever beam structure*. It

consists of the above-ground and the underground segments, separated by the GL. The initial commissioning of wooden utility poles was done to distribute communication signal from Washington D.C. Capitol Building to Baltimore railroad station. Invented by Samuel Morse in 1843, the design of a wooden pole has not been revolved too much (Bernhardt, 2017). The specifications and dimensions for modern wood utility pole are governed by the *American National Standard for Wood Utility Products* (ANSI, 2017).

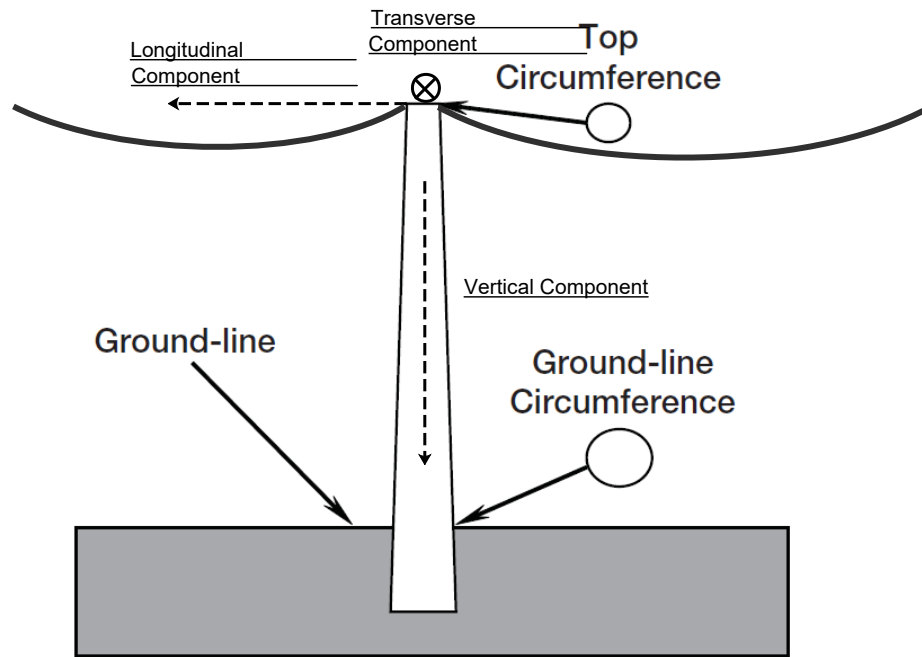


Figure 2.2: An illustration of the pole structure

According to the standard, approximately 10% of its length plus 4 feet must be buried under ground. With an established soil condition, the groundline region bears a significant amount of *bending stress* which is determined by the following (Hibbeler and Fan, 2004),

$$\sigma_{\max} = \frac{Mc}{I}, \quad (2.1)$$

where  $M$  is the bending moment, and is a function of the loading condition imposed on the pole.  $c$  is the perpendicular distance from the axis of symmetry to a point farthest away

from the neutral axis.  $I$  is the *moment of inertial* of the cross-sectional area with respect to the longitudinal axis. For a cylindrical object like a utility pole,  $I = mR^2/2$ , where  $m$  is the mass of the object and  $R$  represents the radius. This analytical expression reveals that under a specific load condition, the groundline region experiences the most bending moment. Furthermore, the bending stress is concentrated at the circumferential region. An experiment conducted by (Sandoz and Vanackere, 1997) employed 200 used poles and observed the locations of failures. Among the sample population, it appears that the failure often occurs few centimeter above the goundline. The result is illustrated in Fig. 2.3.

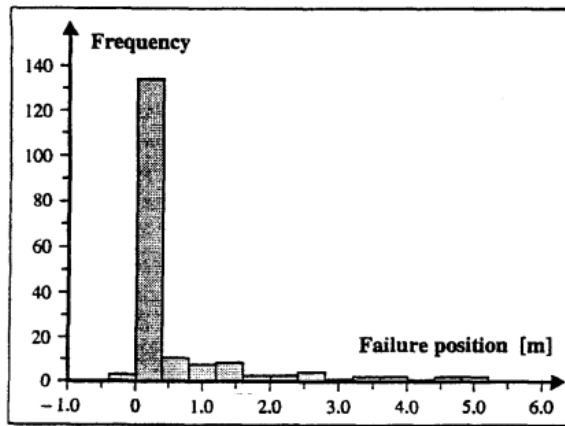


Figure 2.3: Pole failure location with respect to the ground level at zero. Figure was extracted from (Sandoz and Vanackere, 1997).

Normally, the load supported by an utility pole consists of three components: vertical, longitudinal and transverse component (shown in Fig. 2.2) (Keller, 2010) and (Wolfe and Moody, 1994). The vertical load is in line with the axis of symmetry along with the direction of gravitation. This load is the sum of the weight of the pole, the weight of the conductors, and other attached electrical and communication equipment might be present on the top of a pole. The longitudinal load corresponds to the horizontal component from the weight of the conductors. It is a function of the sag and tension values of the conductors. It largely depends on the geometry of the attached conductors. Environmental factors



such as ice and wind can generate an additional load perpendicular to the plane formed by the vertical and the longitudinal components. This is defined as the transverse load. The environmental or climatic condition depends heavily on the geographical location. A map designating different transverse load zones based on the geographical location is depicted in Fig. 2.4.

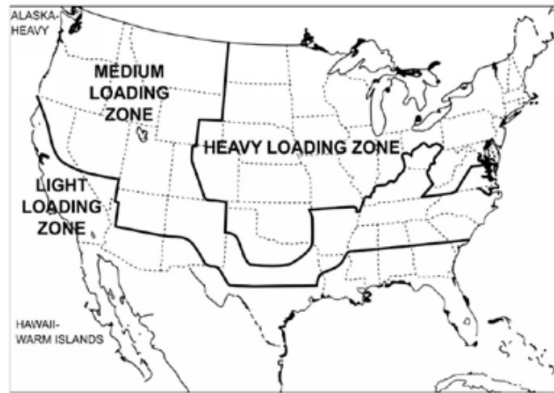


Figure 2.4: A loading zone of utility poles in the United States

### 2.1.1 Hierarchical View of Wood and Porosity

A tree of a preferred species is milled to a defined specification to produce a wooden utility pole. The background information about the wood structure is important for the later Chapters. Fig.2.5 progressively dissects a tree from the macroscopic to the microscopic level. In the macroscopic view, the difference in growth rates in the spring and the autumn results in different wood densities. The density variation creates the so-called *annual ring*. Such a variation can be as large as 50% according to (Koubaa et al., 2002). The annual ring grows every year in the radial direction. This growth process renders the mechanical properties to have the directional dependency in the radial, tangential and longitudinal directions, which it is often termed the *orthotropic* medium. By zooming into each annual ring, we can explore the cell level in the millimeter scale. In Fig. 2.5, a bound-

ary separating the spring and fall woods is clearly shown. There are two different fibrial structures forming a network of channels to support the growth. The ray cells constitutes about 10% of the wood) orienting in the radial direction, and the remaining fibers positioning in the longitudinal direction transports water and nutrients from the roots to the leaves. The cellular structures of the fibers form a porous medium that is governed by another set of principles which will be discussed in Chapter 4. Further magnification reveals the primary and secondary cell walls shown in Fig. 2.7. This structure is considered as a composite material. The progression of growth starts with the construction of the primary wall, followed by the three secondary walls. Each cell wall is constructed by the *microfibrils* material.  $S_2$  is the thickest layer dominating the effective mechanical property.  $S_2$  contains microfibrils that are oriented closely along the longitudinal direction. It is the orientation of the microfibrils material that contributes to the unique physical properties, and the main load-bearing elements in wood. Through the technique of *nanoindentation* conducted by (Gindl et al., 2004), the mechanical properties of the wood cell can be examined. Fig. 2.8 shows the distribution of the mechanical properties based on the microfibril angle (MFA). It suggests a correlation between mean MFA and mechanical properties. This insight into the microscopic properties will be later used in Chapter 4.1.3 to develop a numerical technique transforming the microfibril properties into effective mechanical properties in the macroscopic level. A further looking into the molecular level, the fundamental constituents of wood are the cellulose, hemicellulose and lignin (Shmulsky and Jones, 2019). Cellulose is a replication of the molecule ( $C_6H_{10}O_5$ ) jointed together to form the polymer. Each polymer can have a long-chain of at least 10,000 molecules. A familiar example of cellulose is cotton which is 99% pure cellulose. It is a polymer synthesized within the living cells from the glucose-based sugar nucleotide through *photosynthesis* process converting water and carbon dioxide into glucose and other simple sugars. The second constituent is Hemicellulose. It is a product of other sugar derivatives from the leaves such as glucuronic acid.

They are relatively smaller polymers compared to cellulose. These hemicellulose polymers are made from about hundreds of sugar units. The final constituent is the Lignin. It is composed of carbon, hydrogen and oxygen, forming a stable structure linking different wood cells. Within each cell wall, lignin intimately intertwines with cellulose and hemicelluloses giving further rigidity to the medium. Furthermore, Lignin contains toxic chemicals, which forms a layer of protection against decay and insect attacks.

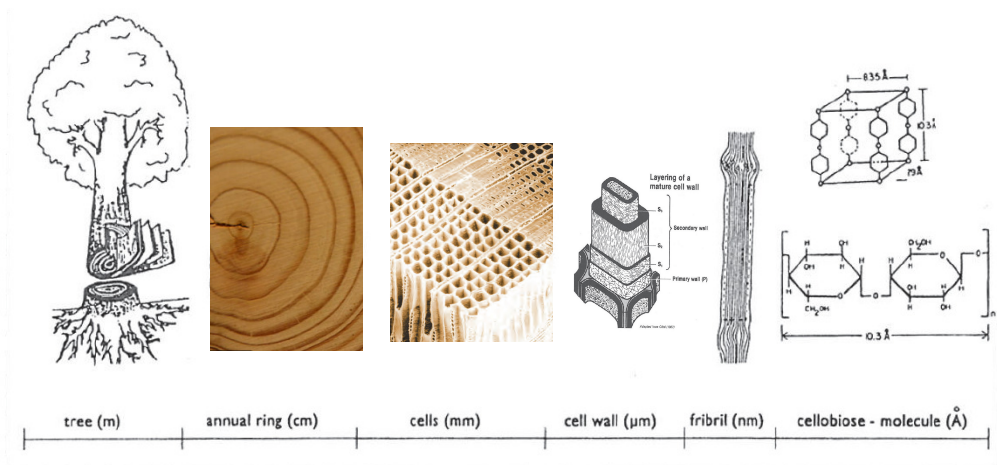


Figure 2.5: Hierarchical order of a wooden structure (Bucur, 2006).

### 2.1.2 Brief Overview of Decay Fungi

One of the primary processes that degrades the quality of wood fiber and ultimately makes them unsuitable for service is the natural decay process. Statistically, more than 50% of pole removal is done due to decay as shown in Fig. 2.9. In general, brown-rot and white-rot are the two primary types of rotting processes that attack softwood. Regardless of which rotting process is occurring, proper moisture content and temperature are required to support the fungal growth. The decay occurs when the moisture content is above 30% (Green III et al., 1995). In addition, the favorable temperature needs to be between 35°F and 100°F (Eaton et al., 1993). Based on the favorable environmental condition for fungal

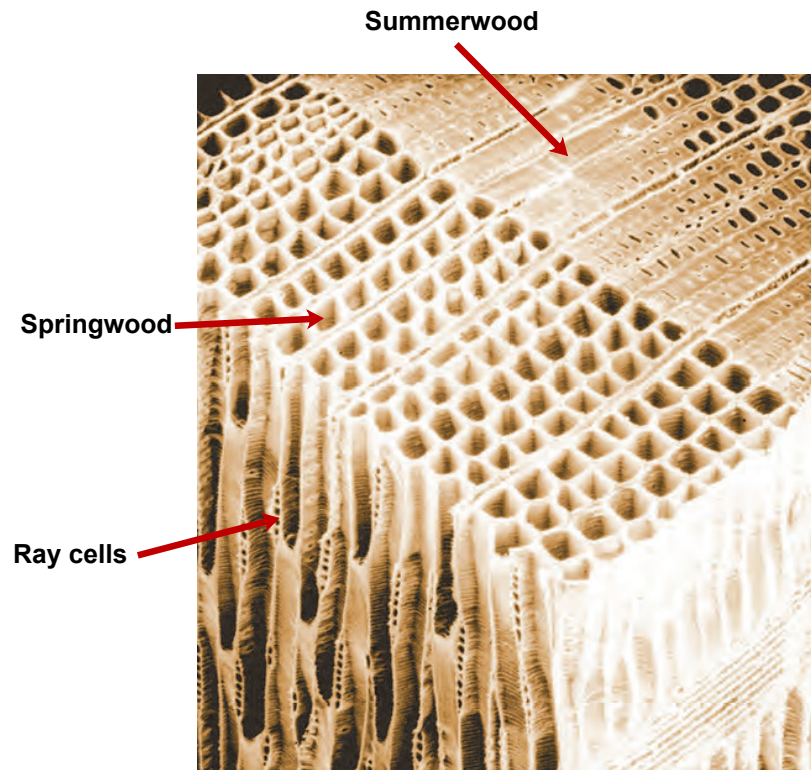


Figure 2.6: Enlarged view of fibers in Douglas-fir (Morrell, 2012).

growth, Fig. 2.10 shows a map of the United States divided according to the risk level of decay. The decay process affects both the microscopic and macroscopic integrity.

Microscopically, when white-rot associated fungi is introduced into the wood, a network of hyphae begins to digest the cell wall material resulting in cell wall thinning. Through a slow decomposition process, the wooden material begins to shrink, forming cavities within the cell walls (Cowling, 1961). Normally, white-rot does not exhibit any dark-colored residual material.

Unlike white-rot, the cells that are attacked by solitary hyphae are classified as brown-rot. The decomposition is rapid, and uniform and dark-colored appear in the infected material. Prior studies suggest that the brown-rotted wood does not experience wall thinning until in later stages (Cartwright and Findlay, 1943). Since solitary hyphae plays a major role in the decay process, irregular decomposition from cell to cell can often be observed.

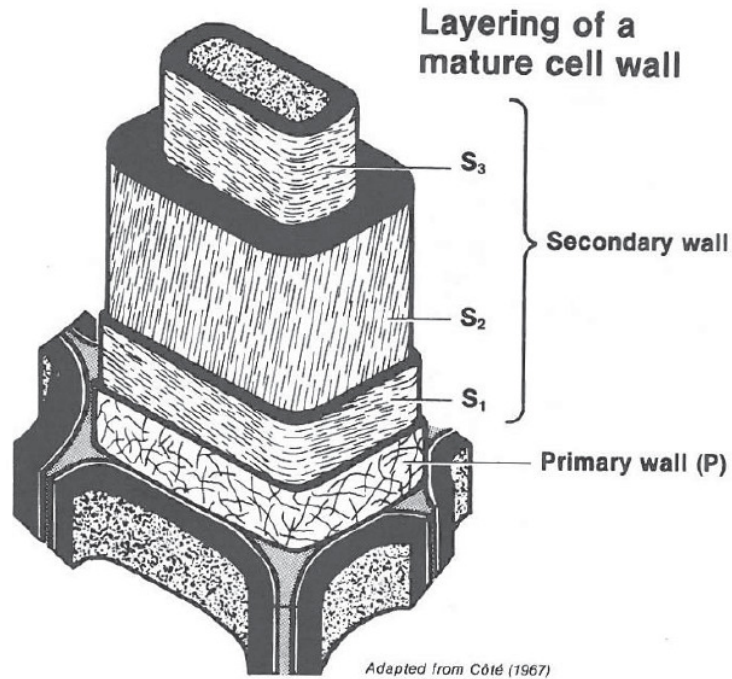
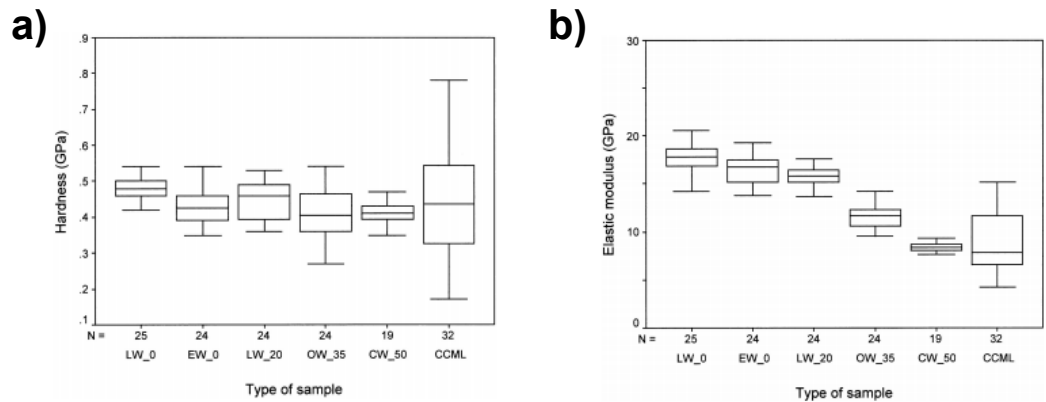


Figure 2.7: Cell structure (Haygreen et al., 1996).

In the moderate stage of brown rot, cracking within the cell wall can often be seen until it is completely penetrated in the later stages. In the advanced stage, the cell wall can be completely destroyed (Pechmann and Schaile, 1950). In both cases, the subsequent reduction in porosity at the submicrobial level can be measured. (Cowling, 1961).

The processes of translating the microscopic degradation to macroscopic degradation are detailed in other studies. The latest experiment using the so-called "cake-pan" method was performed (Winandy et al., 2000). The experiment exposes several wood specimens to two monocultures of brown fungi (*Gloeophyllum trabeum* and *Postia Placenta*) for a period between 3 to 12 days. Based on the different incubation period, the exposed specimen are mechanically tested to evaluate the correlation between the progression of decay and the mechanical properties. Fig.2.11 suggests that when the fungi are introduced, the mechanical properties, modulus of elasticity (MOE) and modulus of rupture (MOR) and density are reduced. Weight loss associated with the digestion of the cell wall also occurs but at a



Sample description	Mean MFA (°)	Sample code
Normal early wood from a spruce stem	0	EW_0
Normal late wood from a spruce stem	0	LW_0
Normal late wood from a spruce stem	20	LW_20
Opposite wood from a spruce branch	35	OW_35
Compression wood from a spruce branch	50	CW_50

Figure 2.8: Mechanical properties of the cell walls obtained from the nanoindentation technique. (Gindl et al., 2004).

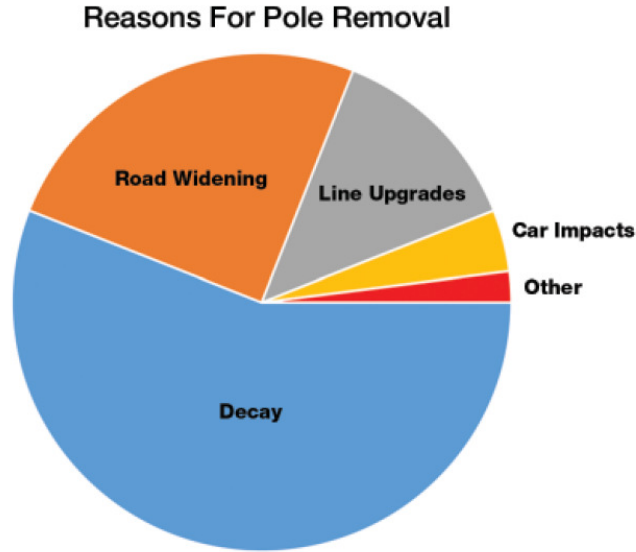


Figure 2.9: The composition of the removal due to various circumstances (Morrell et al., 2006)

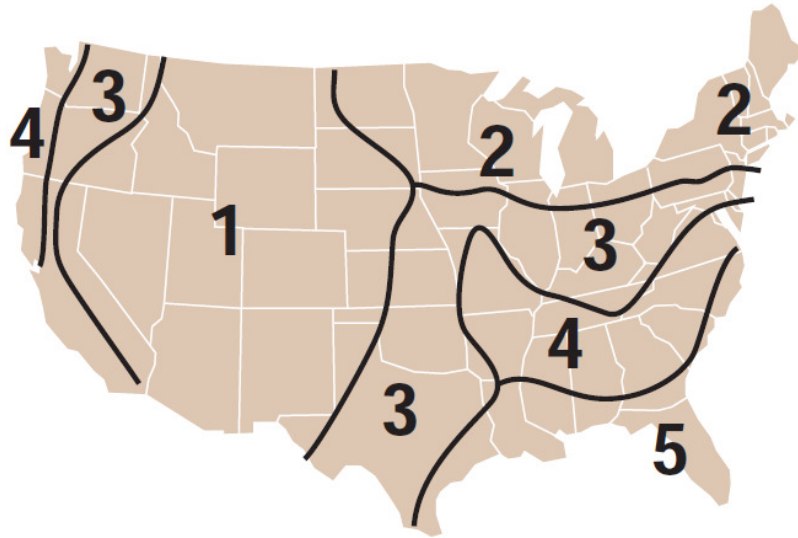


Figure 2.10: Relative decay risk in the United States divided by region (1 = low risk, 5 = high risk)(Morrell, 2008)

slower rate compared to the mechanical properties. This important finding has a significant implications in elastic wave propagation which will be further explored in Chapter 3.

### 2.1.3 Preparation and Preservatives

In the final stage of the manufacturing process, wood poles are subjected to chemical treatment in order to prolong their service lives. Cycling through the decompression and compression processes, the preservatives are forced into wood interior to a desired depth of penetration at a level of retention. As an example, a full-cell process begins with the vacuum pressure (below atmospheric pressure) to draw the air out from the wood fiber matrix. Then, preservatives are introduced with an increase in pressure to around 100 to 150 psi, infusing the chemical into the wood. The desirable amount of chemical penetration depends on exposure time in the high-pressure environment. In order to prevent any chemical from bleeding out, which is called *kickback*, subsequent vacuum pressure is applied to minimize the effect (Barnes, 2007) when it is exposed to the atmospheric environment. The mini-

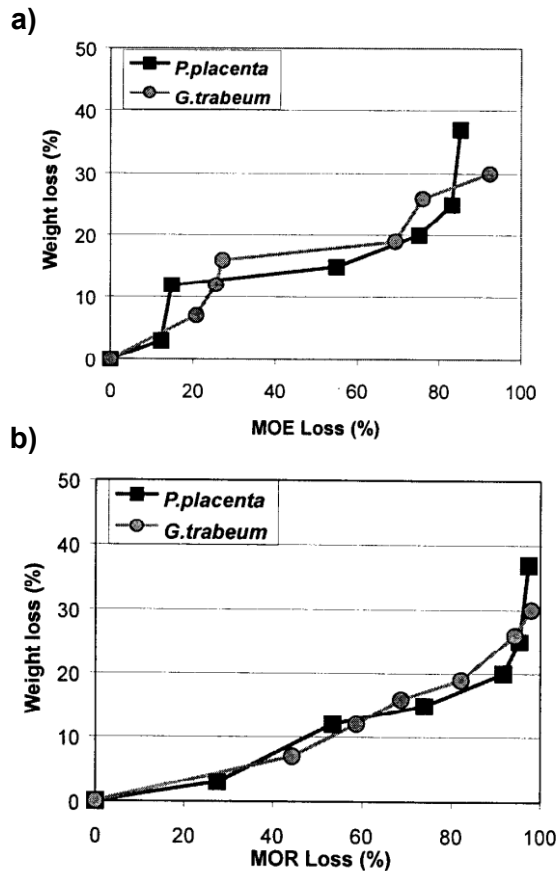


Figure 2.11: Empirical result of the relations between MOE, MOR and weight loss (%) (Winandy and Morrell, 1993).

imum levels for penetration and retention of preservatives are defined under the AWAP. A figure provided by (Morrell, 2008) illustrates the compression and decompression cycles.

There are two different categories of preservatives: oil-based and water-based (Morrell, 2008) and (Filter, 1984). The main active ingredient in the oil-based preservatives are arecreosote, pentachlorophenol (penta), and copper naphthenate. Due to the toxicity of oil-based preservatives, its use is highly regulated and monitored. Water-based preservative, on the other hand, is not as restricted as the oil-based preservative. It contains at least 90% water and only 10% toxic chemicals and produces clean, residue-free surfaces. The primary active ingredient includes copper, zinc and arsenate. The wider use of water-based



preservative increases its moisture content within the wood cells. The distinction between elevations due to natural moisture and treatment needs to be distinguished to prevent *false positive* detection of potential decay. This issue has been noticed in the industry about distinguishing a decay accompanied by high moisture content and a simple high moisture content due to treatment. In this study, this challenge will be addressed in Chapter 4 and 6 .

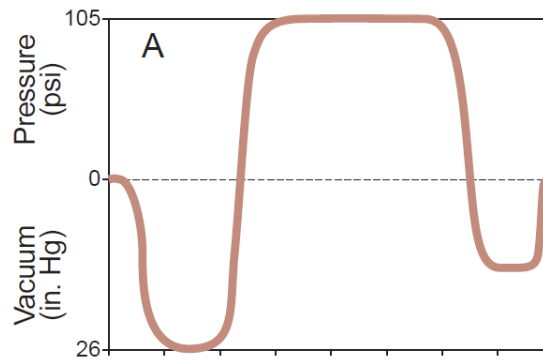


Figure 2.12: Process for impregnation of preservatives into wood.

## 2.2 Literature Review of Ultrasonic-based Evaluation

By definition, acoustic and ultrasonic techniques utilize the propagation of elastic deformation to characterize the material property. It has been a standard NDE technique in the industry to evaluate and characterize metals. The first study of evaluating various NDE performance for wooden material characterization started in 1981 by Szymani (Szymani and McDonald, 1981) and Gerhard (Gerhards, 1982). Among various NDE techniques, Szymani concludes that the ultrasound is the most promising technique that can quickly assess utility poles if the sensor coupling could be overcome. Due to the porous and uneven features on the wooden surfaces, it is a technical and logistic challenge of how to bypass the resulting signal variation. This study precisely focuses on it by offering a potential solution.

This section introduces the fundamental technologies and understanding behind ultrasonic-based non-destructive evaluation. It includes the analysis of wave mechanics, the existing elastodynamic models and the typical hardware implementations of this technology.

## 2.2.1 Wave Pattern

### Phase Velocity

The phase velocity is based on the wave equation derived from the first principle in solid mechanics. The phase speed is measured as a function of density and elastic moduli (e.g., Young's and shear moduli). The first noticeable experiment that correlates the initial TOF and the elastic moduli is based on the work by Sandoz (Sandoz, 1989), the result shown in Fig. 2.13 suggests a good correlation with the correlation coefficient of 0.82. Due to the *dispersive property* of wood, Bucur (Bucur, 1983) examined the variation in the phase speed at frequencies of 80 kHz to 2 MHz. The findings concludes that velocity has a spectral dependency in the longitudinal mode. Through regression analysis, Bucur also found a high correlation among the elastic modulus, density, and phase velocity. Under the groundline cross-sectional configuration, the fiber direction with respect to the propagation direction strongly affects the phase velocity of the elastic wave. A study emphasizing the effect of the grain angle on the radiation source in the longitudinal-radial plane was conducted by Suzuki (Suzuki et al., 1990). It suggests that the ultrasonic phase velocity would decrease during the angle when the source and grain direction is between  $0^\circ$  and  $45^\circ$ , but when the grain angle increases further from  $45^\circ$  to  $90^\circ$  degrees, corresponding to the cross-section region, the change is less pronounced. This finding is a good indication that it is safe to neglect the effect of the fiber angles when using elastic waves to characterize the material property. In the cross-sectional plane, work performed by Mishiro (Mishiro, 1996a) and (Mishiro, 1996b) details the analysis of how elastic wave speed is affected by the an-

nual rings. More specifically, an empirical model was developed, suggesting the principle propagation speed in any direction is a nonlinear combination of the tangential and radial components. This is another evidence suggesting orthotropy of the wood medium.

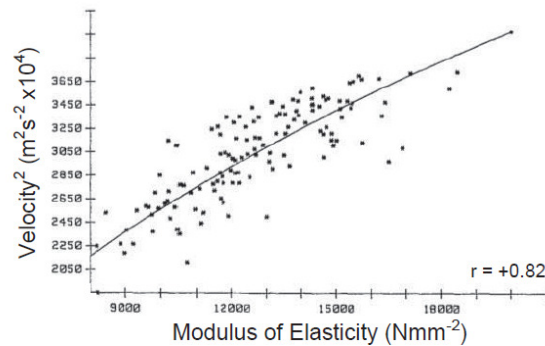


Figure 2.13: Experimental result of modulus of elasticity versus velocity squared. (Sandoz, 1989)

### Energy Absorption

Wood is considered as a sound-absorbing material due to its microscopic porous structure. Hence, the energy absorption of the elastic wave or often referred to as the attenuation has been studied. One of the pioneering work in this area was conducted by Bucur in 1992 (Bucur and Feeney, 1992). The experiment uses the acousto-ultrasonic (AU) pulse-echo technique illustrated in Fig. 2.14 to examine the attenuation of energy at different distances. Attenuation was measured using decibels per centimeter of various frequencies. This study concludes that the energy absorption of the elastic wave has both the spectral and directional dependencies. More specifically, high-frequency elastic waves tend to attenuate quicker in wood. In the cross-sectional region, the tangential direction has a higher attenuation compared to the radial direction.

When applying for log production inspection, a study conducted by Han (Han and Birkeland, 1992) examines the cross-sectional wave propagation by positioning the transducers at the opposite ends (0° and 180°). By detecting and analyzing the initial energy

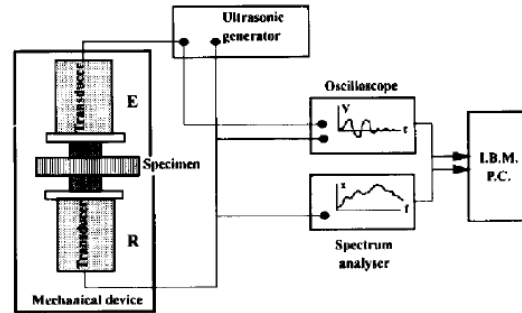


Figure 2.14: Experimental set up using pulse-echo technique (Bucur and Böhnke, 1994)

curve, two attributes are obtained: propagating time and the energy attenuation. Employing the *fuzzy set theory* developed by Zadeh (Zadeh, 1965), membership curves of velocity and energy attenuation are created. The membership curves are classified into low, normal, and high velocity groups and the normal and high attenuation groups. The detection result was compared with the computational x-ray tomography (CT) and a qualitative agreement was reached. Built upon the findings from his study, this work adds the following improvements:

- Elastic wave model is incorporated into model so that the different energy peaks within the wave pattern can be associated with the region within the wooden pole. This arrival mode analysis approach provides greater details about different regions within the cross-section.
- Peak detection algorithm from Han employs the root mean square (RMS) measurement, this can be improved with the TF domain analysis which will be later introduced.
- Han's approach of using standardized membership function via fuzzy set can be improved by integrating arrival plot and attenuation into one single representation for pattern classification.

In the following sections, the backgrounds regarding the prior work of the elastic wave propagation model and the signal analysis will be discussed.

### **2.2.2 Elastodynamics Model**

The wave propagation characteristics in wood is a classical elastodynamic problem. A systematic approach of high-fidelity numerical model that represents the wooden medium has yet to be fully developed. Early models use the isotropic assumption to analyze the elastic wave propagation within the cross-section domain. One of the first finite element models was developed by Wilson in 1965 (Wilson, 1965) to study the elastodynamics in solid under the cylindrical symmetry. It establishes the foundation for later development of the first finite element method (FEM) specifically for wood (Bulleit and Falk, 1985). By employing the isotropy, the wavefronts moving radially and tangentially were noted. An improved numerical model employing orthotropic property was developed analytically and numerically by (Senalik, 2013) and (Payton, 2003), the results are depicted in Fig. 2.15. They both produce a time progression of the dilatational (often referred to as the longitudinal mode) wave propagation at different times. The result shows an initial radiation pattern of a point source, forming a beam-like feature in the orthotropic medium. As the initial wavefront reaches the center, the orthotropy of the medium scatters the energy in all directions forming a radially expanding wave with axial symmetry. This study will recreate the numerical result and emphasize the shell region with enhanced features. In addition, this work highlights that the inclusion of orthotropy and the intrinsic annual rings is important. The embedded waveguide interaction with the orthotropic medium will be analyzed systematically to ensure its accuracy. To further increase the fidelity, this study will explore the viscous damping effect based on the *Biot-Allard's* poroelastic propagation model.

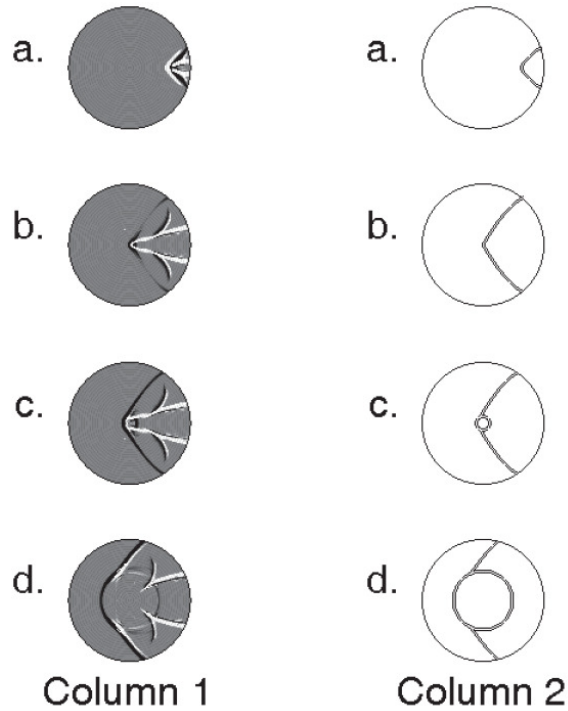


Figure 2.15: Dilatational wave motion produced by (Senalik, 2013) column 1 and (Payton, 2003) in column 2 at a)  $43 \mu s$ , b)  $116 \mu s$ , c)  $129 \mu s$  and d)  $172 \mu s$

### 2.2.3 Hardware Implementation

A portion of this work contributes to the development of a industrial graded ultrasonic instrumentation, a joint effort between the University of Denver and a private company, Utility Asset Management Inc (UAM). Before introducing the system in Chapter 6, this section will introduce the technical background associated with the development of the ultrasonic devices. In order to produce and receive an ultrasound, the instrument consists of two critical components. They are the ultrasonic transducer that employs the pizeoelectric effect, and the driving and receiving circuits. Ultrasonic transducers are categorized into two different types: the narrow-band and the broad-band transducers. Broad-band transducers are normally used in applications that require short pulses and broad spectral analyses. The short pulses enable the examination of the signal response over a continuous

range of frequencies. These characteristics allow such kind of transducers to be used in non-destructive testing and evaluation of materials. The current state of the broad-band transducers normally ranges from few hundred kHz to several MHz for achieving small wavelength/high spatial resolution. This study focuses on using the narrow-band ultrasonic signal to characterize the medium. Related literature can be found in (Goll, 1979), (Gallego-Juarez, 1989) and (Ultrasonics, 1975).

A narrow-band transducer is defined as the bandwidth to be a few percentages of the center frequency. This type of transducers tends to be in the low-frequency range and are used in high power applications. The Langevin transducer is one such example. However, most wood-related studies have discarded it due to the narrow-band spectral information this kind of transducers can provide. Narrow-band transducers offer analytical advantages and the capability to material characterization, which will be detailed in Chapter 3.4.

This section will introduce the piezoelectric transducers and the associated piezoelectric effect. Simple circuitry for the excitation signal, reception circuit and the data acquisition will be briefly discussed. Finally, some of the experimental and industrial grade instruments will be introduced.

## **Fundamental Principles**

The heart of an ultrasonic transducer is the *piezoelectric ceramic*. This material possesses a unique property, which can expand and contract in the same direction as the applied electric field. The phenomenon is governed by the piezoelectric effect discovered in 1880 by Pierre and Jacques Curie. Originally, piezoelectric ceramic are ferroelectric crystallites which are isotropic. When a low-level electric field is applied, the random orientation of the displacement fields within each crystal cancels out each other, exhibiting no overall displacement. This is called the unpolarized state of a piezoelectric ceramic. It is important to polarize all the different displacement vector by the so-called *poling* treatment. The poling

treatment applies a high energy electric field in a desired orientation, forcing the polar axes of the crystallites to point *close* at the direction of the applied electric field. The result is a permanent polarization. Figure 2.16 illustrates the unpolarized and polarized piezoelectric crystal.

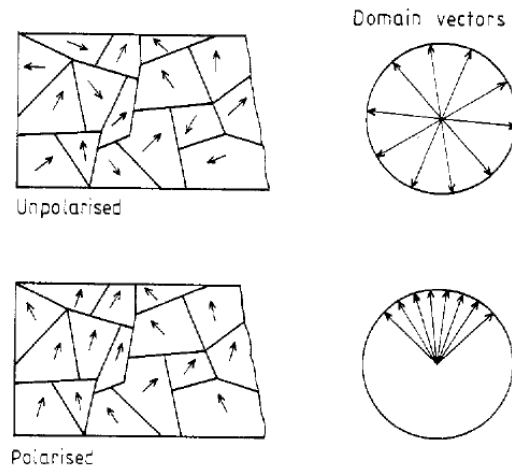


Figure 2.16: Alignment of the domain displacement before and after a poling treatment is applied. (Gallego-Juarez, 1989)

To understand basic construction of a piezoelectric transducer, the piezoelectric effect is introduced. The equation of motion of the piezoelectric behavior is described by the following set of equations.

$$\left\{ \begin{array}{l} x = dE, \\ E = gX, \\ k^2 = \frac{\text{stored electric energy}}{\text{input mechanical energy}}, \\ Q_m = \frac{\omega_0}{2\Delta\omega}. \end{array} \right. \quad (2.2)$$

The first equation of (2.2) relates the imposed electric field  $E$  and the induced strain  $x$ .  $d$  is the *piezoelectric strain constant*. The second equation of (2.2) describes the induced electric field  $E$  and the external stress  $X$  with the piezoelectric voltage constant  $g$ . The relation



between  $g$  and  $d$  can be related by the expression:  $g = d/\epsilon_0\epsilon$  where  $\epsilon_0$  is the permittivity of free space and  $\epsilon$  is the relative permittivity. The third equation is the electromechanical coupling factor, which describes the conversion rate between electrical energy and mechanical energy.  $k^2$  is an critical quantity that differentiates the qualities of different piezoelectric material designs. For simple geometries, the coupling factors are depicted in Fig. 2.17.  $Q_m$

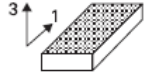
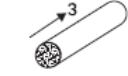

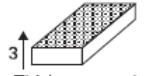
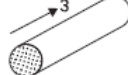
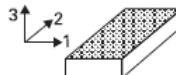
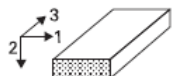
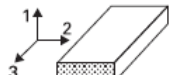
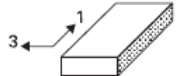
	Coupling factor	Elastic boundary conditions	Resonator shape	Definition
a	$k_{31}$	$X_1 \neq 0, X_2 = X_3 = 0$ $x_1 \neq 0, x_2 \neq 0, x_3 \neq 0$		$\frac{d_{31}}{\sqrt{s_{11}^E \epsilon_{33}^X}}$
b	$k_{33}$	$X_1 = X_2 = 0, X_3 \neq 0$ $x_1 = x_2 \neq 0, x_3 \neq 0$	 Fundamental mode	$\frac{d_{33}}{\sqrt{s_{33}^E \epsilon_{33}^X}}$
c	$k_p$	$X_1 = X_2 \neq 0, X_3 = 0$ $x_1 = x_2 \neq 0, x_3 \neq 0$	 Fundamental mode	$k_{31} \sqrt{\frac{2}{1-\sigma}}$
d	$k_t$	$X_1 = X_2 \neq 0, X_3 \neq 0$ $x_1 = x_2 = 0, x_3 \neq 0$	 Thickness mode	$k_{33} \sqrt{\frac{\epsilon_{33}^X}{c_{33}^D}}$
e	$k_p'$	$X_1 = X_2 \neq 0, X_3 \neq 0$ $x_1 = x_2 \neq 0, x_3 = 0$	 Radial mode	$\frac{k_p - Ak_{33}}{\sqrt{1-A^2} \sqrt{1-k_{33}^2}}$
f	$k_{31}'$	$X_1 \neq 0, X_2 \neq 0, X_3 = 0$ $x_1 \neq 0, x_2 = 0, x_3 \neq 0$	 Width mode	$\frac{k_{31}}{\sqrt{1-k_{31}^2}} \sqrt{\frac{1+\sigma}{1-\sigma}}$
g	$k_{31}''$	$X_1 \neq 0, X_2 = 0, X_3 \neq 0$ $x_1 \neq 0, x_2 \neq 0, x_3 \neq 0$	 Width mode	$\frac{k_{31} - Bk_{33}}{\sqrt{1-k_{33}^2}}$
h	$k_{33}'''$	$X_1 \neq 0, X_2 \neq 0, X_3 \neq 0$ $x_1 \neq 0, x_2 = 0, x_3 = 0$	 Thickness mode	$\frac{\sqrt{(k_p - Ak_{33})^2 - (k_{31} - Bk_{33})^2}}{1 - k_{33}^2 - (k_{31} - Bk_{33})^2}$
i	$k_{33}'$	$X_1 \neq 0, X_2 = 0, X_3 \neq 0$ $x_1 = 0, x_2 \neq 0, x_3 \neq 0$	 Width mode	$\frac{k_{33} - Bk_{31}}{\sqrt{(1-B^2)(1-k_{31}^2)}}$
j	$k_{24}=k_{15}$	$X_1 = X_2 = X_3 = 0, X_4 \neq 0$ $x_1 = x_2 = x_3 = 0, x_4 \neq 0$		$\frac{d_{15}}{\sqrt{\epsilon_{11}^X \epsilon_{44}^E}}$

Figure 2.17: Piezoelectric resonance modes and the corresponding coupling factors(Uchino, 2012), the shaded areas are the applied electric field.

in the final equation is called the mechanical quality factor,  $\omega_0$  is the resonance frequency, and  $\Delta\omega$  denotes the full width of the spectral response centered at the resonance. High  $Q_m$  indicates a sharp spectral response about its resonance, and low  $Q_m$  generates a flatter spectral response about its resonance (off-resonance frequency). In the next section, these quantities will be explored to understand the behaviors of the piezoelectric material and the design principles behind a piezoelectric transducer.

### **A Brief Overview of Piezoelectric Materials**

Wooden medium holds the physical characteristics of a porous medium. Its spectral response suggests a strong energy dissipation. In addition, wooden medium has a very different *acoustic impedance* compared to metal. In order to transmit elastic wave through high attenuating medium with pronounced impedance mismatch, high-power transducers are required (Gallego-Juárez et al., 1978). In order to produce a high-power transducer, a selection of piezoelectric material is critical. This section is to provide an overview of some widely used piezoelectric materials in high-power applications.

Piezoelectric materials are categorized into single-crystal and polycrystalline. Their piezoelectric properties are shown in Fig. 2.18. Quartz is the only single-crystal in the list, while it has a high voltage constant and mechanical quality factor, the coupling factors  $k_t$  and  $k_p$  values are low compared to the polycrystal. The polycrystalline materials are well-rounded in terms of exhibiting good piezoelectric properties. Hence, piezo-ceramic have been widely used in a large number of applications due to its desirable piezoelectric properties across the different piezoelectric parameters (e.g.,  $d$ ,  $g$  and  $k$ ). Within the piezo-ceramic category, lead zirconate titanate or the PZT family has proven to have the best  $d$  and  $k$  properties. The PZT family is divided into three subcategories: soft, semi-hard and hard PZTs. The soft PZTs exhibit high  $k$ ,  $d$  and  $\epsilon$  values, but with low  $Q_m$ , produces a rather broader spectral response. They are suitable for off-resonance applications. Hard PZTs,

exhibit a high  $Q_m$  value, which is suitable for resonance application. Fig. 2.19 shows the differences among the subcategories of PZTs. In a high-power application where a narrow-band spectral response is desirable (Gallego-Juarez, 1989), PZT-4 is an preferred choice.

Parameter	Quartz	BaTiO <sub>3</sub>	PZT-4	PZT-5H	(Pb,Sm)TiO <sub>3</sub>	PVDF-TrFE
$g_{33}$ ( $10^{-3}\text{V.m.N}^{-1}$ )	57.8	12.6	26.1	19.7	42	380
$k_t$	0.09	0.38	0.51	0.50	0.50	0.30
$k_p$		0.33	0.58	0.65	0.03	
$\epsilon_3^X/\epsilon_0$	5	1700	1300	340	175	6
$Q_M$	$> 10^5$		500	65	900	3–10
$T_c$ (°C)		120	328	193	355	

Figure 2.18: Piezoelectric properties of typical PZTs (Uchino, 2012)

	Soft PZT-5H	Semi-hard PZT-4	Hard PZT-8
EM coupling factor			
$k_p$	0.65	0.58	0.51
$k_{31}$	0.39	0.33	0.30
$k_{33}$	0.75	0.70	0.64
$k_{15}$	0.68	0.71	0.55
Piezoelectric coefficient			
$d_{31}$ ( $10^{-12}\text{m.V}^{-1}$ )	-274	-122	-97
$d_{33}$	593	285	225
$d_{15}$	741	495	330
$g_{31}$ ( $10^{-3}\text{Vm.N}^{-1}$ )	-9.1	-10.6	-11.0
$g_{33}$	19.7	24.9	25.4
$g_{15}$	26.8	38.0	28.9
Mechanical $Q_M$	65	500	1000

Figure 2.19: Piezoelectric properties of typical PZTs (Gallego-Juarez, 1989)

## Transducer Designs and Driving Circuit

In practice, a piezoelectric ceramic is pre-stressed. The stored mechanical energy amplifies the amplitude of the energy emission when an external electric field is applied (Uchino, 2012). During the manufacturing of a narrow-band transducer, a pre-compression

bolt with typical stress of  $300 \text{ kg/cm}^2$  is used to create the desired condition. A sectional view of a narrow-band Langevin transducer is depicted in Fig. 2.20. The transducer consists of the back section, the pre-compression bolt, piezoelectric ceramic and the output section. The back section is made of a denser and heavier material than the output section. This design allows the vibration energy from the piezoelectric material to be directed to the front output section. The live terminal and the ground are the electrodes for generating the electric potential across the piezoelectric ceramic.

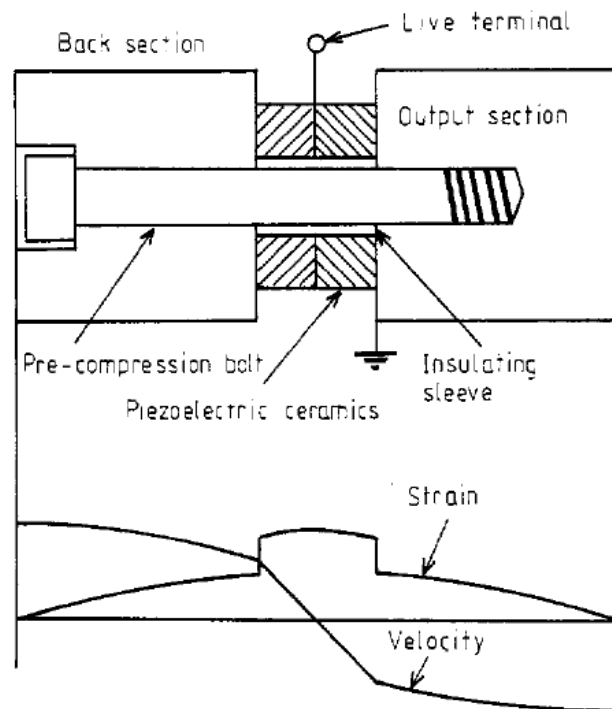


Figure 2.20: A sectional view of a Langevin transducer (Gallego-Juarez, 1989)

To excite the transducer, different electrical pulse shapes have been studied in literature (Okyere and Cousin, 1979), (Hayward, 1985) and (Ramos-Fernández et al., 1987). The most common pulse shape uses high-voltage square wave modulation. Circuitry capable of producing high voltage pulses is termed pulser circuit. It is normally constructed with a low voltage pulse generator, which can be both fixed or adjustable frequency to produce a

reference square wave. With a high-voltage DC power supply, the reference square wave and the high voltage power supply are combined in the *power stage* to create high-voltage square pulses. This high-voltage square pulse is the driving circuit for the piezoelectric transducer. Fig. 2.21 shows an example of a power stage circuit. The DS0026 is a MOSFET driver to send the modulated square wave to the MOSFET. It is connected to the high voltage DC supply through a pull-up resistor, which is used to apply the reference signal. Further downstream, the combination of a capacitor and the damping resistor  $R_d$  is used to damp out any high-frequency components in the leading and trailing edge of the pulses.

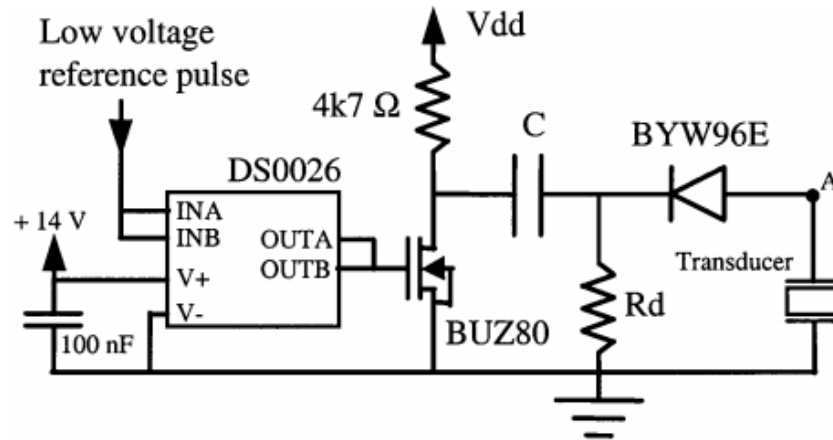


Figure 2.21: A simplified circuit diagram of the power stage circuit(Salazar et al., 2003)

## Interface Coupling

Due to the dissimilar material between the transducer and the wooden surface, energy loss due to *mode conversion* is inevitable. This is termed *acoustic impedance mismatch*. This phenomenon causes a portion of the wave energy to be reflected back to the transducers at the interface. For incident wave traveling perpendicular to surface, the acoustic impedance is defined as  $Z = \rho c_L$ . To minimize reflection, water or oil-based couplant is often used as a mediator to reduce the amount of reflection due to the mismatch. In addi-

tion, the porous nature of the wooden surface, where the material is in the two-phase state (air and solid are co-existed). A certain amount of coupling pressure must be applied to ensure most air-packets are displaced to reduce any interference during the energy transmission (Beall, 2002). Experiments have shown that there will be a loss of about 20-30 dB if couplant is not used. With all the proposed methods, a considerable amount of variations can still be introduced because of the surface variation. It presents a challenge in some research (Han and Birkeland, 1992).

The emerging air-coupled ultrasonic (ACU) technologies have started to be adapted in the industry when the use of couplant is unfeasible. With the absence of the couplant and physical contact, the testing can be performed with high efficiency and high reproducibility (Sanabria et al., 2011). However, the drastic difference in the acoustic impedance between wood and air only permits 0.1% of the emitting energy to be transmitted (Fleming et al., 2005). Even though this technology might be truly a non-destructive evaluation, its limited energy penetration depth confines its applications to specimens with small geometric dimensions, making this technology unsuitable for GL cross-sectional assessment.

To transmit a significant amount of energy into the medium without concerning any surface variability, the proposed technique in this work is to insert a small waveguide into a specimen directly. It creates a 4-mm diameter circular cross-section with an insertion depth of 1 cm. An ultrasonic transducer is then mounted to the back to generate the oscillating load. Many utility firms have accepted this approach due to the small insertion. This technique is termed the embedded waveguide excitation. It induces surface wave modes with high strong energy deposition critical for the shell-region assessment. We will revisit this method in chapter 3, 4 and 6.

## 2.2.4 Signal Processing

The TOF measurement is the most basic method to assess wood quality. It is a measure of the time difference at the moments of transmission and the first detectable wavefront. If a void or a significant decay exists internally along the path, the elastic wave will tend to propagate at a slower phase speed, resulting in a longer TOF (Wang et al., 2004), an indication of decay. However, wood is classified as an orthotropic material with a complex internal structure, wave propagating in a non-linear wooden medium creates complicated temporal and spectral responses in different wave modes. In addition, if the detection of the initial arrival is based on the signal amplitude being above the noise floor, detecting this arrival presents a challenge, in a highly attenuating medium. Using propagation velocity such as TOF as a sole metric in wood to help determine decay conditions appears to be unreliable for determining the conditions based on the data presented by (Winandy and Morrell, 1993). In his paper, a wood species is exposed to different fungus agents to induce both brown-rot and white-rot decays. The specimen is then tested by measuring the wave speed. The resulted TOFs are measured. The empirical data presented in (Winandy and Morrell, 1993) shows that TOF is almost insensitive to the severity of the decay. Consequently, a slight instrumentation error in measuring TOF can give erroneous readings resulting in misleading conditional assessment. Hence, other signal analysis techniques using a combination of attenuation, waveform shape, and frequency content are also employed (Beall, 2002).

Signal attenuation can be measured by calculating the RMS based on the *mean value theorem* (Prakash, 1980). This technique averages out all the signal variations destroying the wave pattern which holds important information about different wave trajectories. Another similar technique (Kim and Heo, 2012) is to determine the *moments of the signal*

which is expressed as,

$$M^n = \int_{t_1}^{t_2} y(t)t^n dt \quad (2.3)$$

where  $y$  is the deterministic time signal.  $n$  is the moment order and  $t$  is the time domain of the signal. By dividing the first moment ( $n = 1$ ) by the zeroth moment ( $n = 0$ ), it results in the so-called time centroid (TC). This metric is based on the shape of the waveform to determine the arrival time of the wave more accurately. In a medium where reflection and mode changes occur frequently, the waveform tends to skew resulting in a shift in the TC. The time centroid can be a measurement of the level of reflection.

Other additional techniques are used based on the broadband transmission of the ultrasound. Due to the dispersive property of the medium, the ultrasonic characteristics, including group propagating speed and amplitude response, are functions of the imposed frequency. Advanced signal analysis and empirical model based on the dispersion curves (Bucur, 1983) are developed. Since this work focuses on the narrow-band transmission, the representative work will not be further discussed. For readers who are interested, they can be found in (Tallavo et al., 2012), (Senalik, 2013) and (Dackermann et al., 2014).



# Chapter 3

## Estimation of Half-space and Subsurface Excitation

### 3.1 Electrodynamics in Isotropic Medium

To study the response analytically, steady-state approach is used to help simplify the formulation. A steady-state classical elastodynamic formulation governs the *equation of motion* (EOM) for elastic wave propagation in an isotropic solid is based on the *Navier equations* (Kolsky, 1963). The origin of the Navier's equation is detailed in Appendix A. With the absence of the forcing term, it is expressed as follow,

$$(\lambda + \nu)\nabla(\nabla\mathbf{u}) + \mu\nabla^2\mathbf{u} = \rho\frac{\partial^2\mathbf{u}}{\partial t^2}, \quad (3.1)$$

where  $\mathbf{u}$  denotes the displacement field in 3-dimensional space  $\mathbf{u} = [u_1, u_2, u_3]$ .  $\mu$  and  $\lambda$  are the Lamé constants describing the physical properties of the propagating medium,  $\rho$  is density,  $\nabla$  is gradient operator expressed as  $\nabla = [\partial_x, \partial_y, \partial_z]$  and  $\nabla^2$  is the Laplacian operator.

By employing the vector identity,  $\nabla^2 \mathbf{u} = \nabla \nabla \cdot \mathbf{u} - \nabla \times \nabla \times \mathbf{u}$ , (3.1) can be expressed as,

$$(\lambda + 2\nu) \nabla(\nabla \mathbf{u}) - \mu \nabla \times \nabla \times \mathbf{u} = \rho \frac{\partial^2 \mathbf{u}}{\partial t^2}. \quad (3.2)$$

The total displacement field can further be decomposed into a scalar field and a vector field using the Helmholtz decomposition. That is,

$$\mathbf{u} = \nabla \phi + \nabla \times \boldsymbol{\psi}. \quad (3.3)$$

It allows the Navier equation to be expressed in terms of the displacement potentials. That is,

$$\begin{aligned} & \left[ (\lambda + 2\mu) \nabla \nabla \cdot (\nabla \phi) - \rho \nabla \frac{\partial^2 \phi}{\partial t^2} \right] - \mu \nabla \times \nabla \times \nabla \phi \\ & + (\lambda + \mu) \nabla \nabla \cdot \nabla \times \boldsymbol{\psi} + \left[ \mu \nabla^2 \nabla \times \boldsymbol{\psi} - \nabla \times \frac{\partial^2 \boldsymbol{\psi}}{\partial t^2} \right] = 0. \end{aligned} \quad (3.4)$$

The diminishing nature of (3.4) demands the following relation for the potentials to hold true,

$$\left[ (\lambda + 2\mu) \nabla \nabla \cdot (\nabla \phi) - \rho \nabla \frac{\partial^2 \phi}{\partial t^2} \right] - \mu \nabla \times \nabla \times \nabla \phi = 0; \quad (3.5)$$

$$(\lambda + \mu) \nabla \nabla \cdot \nabla \times \boldsymbol{\psi} + \left[ \mu \nabla^2 \nabla \times \boldsymbol{\psi} - \nabla \times \frac{\partial^2 \boldsymbol{\psi}}{\partial t^2} \right] = 0. \quad (3.6)$$

(3.5) and (3.6) implies that in a unbonded medium without the forcing function, the potential fields can be decoupled, and each equation describes the EOM for each potential. By employing the following vector identities,

$$\nabla \times \nabla \times \nabla \phi = 0 \quad \text{and} \quad \nabla \cdot \nabla \times \boldsymbol{\psi} = 0,$$

a few mathematical manipulation yields a set of elliptical wave equations for each potential field.

$$\begin{aligned}\nabla^2\phi &= \frac{1}{c_L^2} \frac{\partial^2\phi}{\partial t^2}, \\ \nabla^2\boldsymbol{\psi} &= \frac{1}{c_T^2} \frac{\partial^2\boldsymbol{\psi}}{\partial t^2}.\end{aligned}\tag{3.7}$$

where  $c_L$  is the phase speed associated with the scalar potential  $\phi$  expressed as  $c_L^2 = \lambda + 2\mu/\rho$  and  $c_T^2$  is the phase speed associated with the vector potential  $\boldsymbol{\psi}$  expressed as  $c_T^2 = \mu/\rho$ . The scalar potential is often referred to as the longitudinal mode and the vector potential is often referred to as the transverse mode. The solution to the decoupled wave equation can be solved analytically using the method of "separations of variables". An assumed solution is a product of the spatial and temporal functions denoted as  $\mathbf{X}$  and  $\mathbf{T}$  respectively.

$$\begin{aligned}\phi(\mathbf{x}, t) &= \mathbf{X}_\phi(\mathbf{x})\mathbf{T}_\phi(t); \\ \boldsymbol{\psi}(\mathbf{x}, t) &= \mathbf{X}_\psi(\mathbf{x})\mathbf{T}_\psi(t).\end{aligned}\tag{3.8}$$

Based on a well-known priori that the wave equations will resolve in a time harmonic function. That is,  $\mathbf{T}(t) = e^{i\omega t}$ , where  $\omega$  is the fundamental frequency of the oscillation. The assumed form allows (3.7) to further reduce to the following expression:

$$\begin{aligned}\nabla^2\phi + k_l^2\phi &= 0; \\ \nabla^2\boldsymbol{\psi} + k_t^2\boldsymbol{\psi} &= 0,\end{aligned}\tag{3.9}$$

where  $k_t$  and  $k_l$  are the wavenumbers associated with the transverse and longitudinal modes respectively. Under the isotropic assumption, the wavenumber  $k_l$  and  $k_t$  are expressed in the following:  $k_l = \omega\sqrt{\rho/(\lambda + 2\mu)}$  and  $k_t = \omega\sqrt{\rho/\mu}$ .

The stress-strain relation for elasticity in the indicial notation is written as,

$$\sigma_{ij} = \lambda \sigma_{ij} \varepsilon_{kk} + 2\mu \varepsilon_{ij}, \quad (3.10)$$

where  $\varepsilon_{ij}$  is the strain equation which can be expressed in terms of the displacement field, that is,

$$\varepsilon_{ij} = \frac{1}{2} \left( \frac{\partial u_i}{\partial x_j} + \frac{\partial u_j}{\partial x_i} \right). \quad (3.11)$$

By substituting (3.11) and (3.10) and expressing the displacement fields in terms of the potentials, it produces the EOM for each stress component.

$$\begin{aligned} \sigma_{xx} &= \lambda \left( \frac{\partial^2 \phi}{\partial x^2} + \frac{\partial^2 \phi}{\partial z^2} \right) + 2\mu \left( \frac{\partial^2 \phi}{\partial x^2} - \frac{\partial^2 \psi}{\partial x \partial z} \right), \\ \sigma_{zz} &= \lambda \left( \frac{\partial^2 \phi}{\partial x^2} + \frac{\partial^2 \phi}{\partial z^2} \right) + 2\mu \left( \frac{\partial^2 \phi}{\partial x^2} + \frac{\partial^2 \psi}{\partial x \partial z} \right), \\ \sigma_{xz} &= \mu \left( 2 \frac{\partial^2 \phi}{\partial x \partial z} + \frac{\partial^2 \psi}{\partial x^2} - \frac{\partial^2 \psi}{\partial z^2} \right). \end{aligned} \quad (3.12)$$

where  $\sigma_{i,j}$  represents the principle stress oscillation in the  $j$ -direction with propagation in the  $i$ -direction.

## 3.2 Formulation of Diffusive Propagation

Fig 3.1 illustrates an embedded waveguide inserted in an arbitrary propagating medium at a depth  $L$ . An embedded waveguide consists of the side and front radiating apertures. These apertures are the physical boundaries separating the waveguide and the propagating medium. The load application interface is where the elastic wave can be introduced. The half-space boundary is the discontinuous interface separating the propagating medium from the gaseous surrounding.

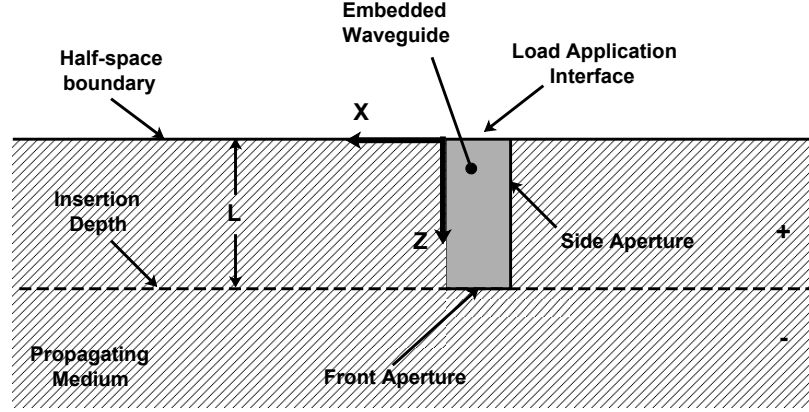


Figure 3.1: A simplified diagram of the problem.

Based on the relatively small mass of the waveguide, we assume the reversible elastic oscillations within the waveguide. Negligible energy attenuation as the elastic wave propagating can be safely assumed. For simplicity, the isotropic condition is applied to the entire domain of interest.

A conventional transducer, such as the Lavigne transducer, uses piezoelectric ceramic (e.g., the lead zirconate titanate (PZT)) to convert between the electrical energy and the mechanical energy. This conversion rate is referred to as the electromechanical coupling factor with the fundamental mode in the longitudinal direction (Uchino, 2012) and (Gallego-Juarez, 1989). It is reasonable to assume that the displacement potential  $\phi$  possesses the time-harmonic traveling wave of the form,

$$\phi_{wg} = \phi_0 e^{i(k_0 z - \omega_0 t)} \quad \text{for } x = 0 \quad \text{and } z \in [0, L]. \quad (3.13)$$

where the subscript  $wg$  denotes the waveguide medium.  $\phi_0$  can be any arbitrary amplitude modulating function.  $\phi_0$  can be a constant and an arbitrary amplitude modulating function. Under the steady-state condition, it renders the function  $\phi_0$  at the boundary to be a constant. In a real case, the time-transient response often occurs in an ultrasonic transducer which renders the function  $\phi_0$  to be a Gaussian function with a mean and a standard deviation.  $k_0$

denotes the wavenumber of the longitudinal mode propagating along the waveguide. For non-attenuating wave traveling along the waveguide,  $k_0$  is real (Achenbach and Epstein, 1967).  $L$  is the insertion depth.

The traction-free boundary condition can be imposed for the half-space between the propagating medium and the surrounding air. That demands the stresses for the longitudinal and transverse modes having the component in the  $z$ -direction to be zero (Viktorov, 1967). That is,

$$\sigma_{zz} = 0 \quad \text{and} \quad \sigma_{xz} = 0 \quad \text{for} \quad z = 0. \quad (3.14)$$

At the side aperture between the embedded waveguide and the propagating medium, the no-slip condition of assuming displacement continuity is imposed. It implies the following boundary condition for the displacement fields at  $x = 0$ :

$$\begin{aligned} W &= W_{wg} \quad \text{for} \quad x = 0, \\ U &= 0 \quad \text{for} \quad x = 0. \end{aligned} \quad (3.15)$$

where  $W_{wg}$  is the disturbance of displacement within the waveguide.

### 3.2.1 Half-space Response

The assumed solution to the wave equations (3.9) is the traveling harmonic waves (Rose, 2004) of the form,

$$\begin{aligned} \phi_0 &= f(k_1^+ x + k_2^+ z - \omega t) = A(t) e^{i(k_1 x + k_2 z - \omega t)}, \\ \psi_0 &= g(k_1^+ x + k_2^+ z - \omega t) = B(t) e^{i(k_3 x + k_4 z - \omega t)}, \end{aligned} \quad (3.16)$$

where  $k$  is the wave number defined as  $k = \omega/c$ , and  $c$  denotes the phase velocity and  $\omega$  denotes the fundamental angular frequency of the propagating wave.  $k_1$  and  $k_3$  are the

wavenumbers associated with the induced longitudinal and transverse components of the Rayleigh mode traveling in the x-direction respectively,  $k_2$  and  $k_4$  are the transverse and longitudinal components of the Rayleigh mode traveling in the z-direction.

Based on the Helmholtz decomposition (3.3), the displacement field in the z-direction at  $x = 0$  is written as

$$W = Ak_2ie^{i(k_2z-\omega t)} + Bk_3ie^{i(k_4z-\omega t)}. \quad (3.17)$$

Similarly, the displacement within the waveguide can be obtained. Enforcing the no-slip boundary condition mentioned previously yields the following relation.

$$Ak_2ie^{i(k_2z-\omega t)} + Bk_3ie^{i(k_4z-\omega t)} = \phi_0k_0ie^{i(k_0z-\omega_0t)}. \quad (3.18)$$

(3.18) constrains the wavenumber and produces the following relations,

$$\begin{aligned} k_2 &= k_4 = k_0; \\ \omega &= \omega_0. \end{aligned} \quad (3.19)$$

The governing equation also enforces the longitudinal and transverse wave numbers  $k_l$  and  $k_t$  to possess the following equality:

$$\begin{aligned} k_l^2 &= k_1^2 + k_2^2; \\ k_t^2 &= k_3^2 + k_4^2. \end{aligned} \quad (3.20)$$

By combining (3.19) and (3.20),  $k_1$  and  $k_3$  have the forms,

$$\begin{aligned} k_1 &= (k_l^2 - k_0^2)^{1/2}; \\ k_3 &= (k_t^2 - k_0^2)^{1/2}. \end{aligned} \quad (3.21)$$

Invoking the stress-strain relation (3.12) and imposing the traction-free boundary condition  $\sigma_{xx} = 0$  and  $\sigma_{xz} = 0$  yields the following algebraic relations,

$$\begin{aligned}\lambda A (k_1^2 + k_0^2) + 2\mu (Ak_0^2 + Bk_3k_0) &= 0; \\ -2Ak_1k_0 - Bk_3^2 + Bk_0^2 &= 0.\end{aligned}\tag{3.22}$$

$\epsilon$  and  $\beta$  are the wavenumber ratios. That is,  $\epsilon = k_3/k_0$  and  $\beta = k_1/k_0$ . By invoking a Lamé relations:  $\lambda/2\mu = \nu/(1 - 2\nu)$ , (3.22) relates the wavenumber ratio to the Poisson's ratio,

$$\epsilon = \frac{\beta - 2\beta\nu \pm \sqrt{(\beta - 2\nu\beta)^2 + (\nu\beta^2 - \nu + 1)^2}}{\nu\beta^2 - \nu + 1}.\tag{3.23}$$

Since all wavenumbers are positive, only the positive quantity of  $\epsilon$  is considered. The absence of frequency dependency in (3.23) suggests that the  $\epsilon$  and  $\beta$  do not exhibit any frequency dispersion. Their values depend only on the Poisson's ratio of the propagating medium. Similar dispersion effect can be observed in the classical Rayleigh characteristic equation (Rayleigh, 1885) in which the wavenumber ratio of the Rayleigh and the transverse mode is only a function of the Poisson's ratio  $\nu$ .

By introducing the wavenumber ratios  $\epsilon$  and  $\beta$ , (3.21) yields the following expression,

$$\epsilon = \left[ \sqrt{\frac{1 - 2\nu}{2 - 2\nu}} (\beta^2 + 1) - 1 \right]^{1/2}.\tag{3.24}$$

To eliminate one of the wavenumber ratios, (3.23) and (3.24) are combined to yield the following relation that satisfies both the no-slip condition and the governing wave equations.

$$\frac{\beta - 2\beta\nu + \sqrt{(\beta - 2\nu\beta)^2 + (\nu\beta^2 - \nu + 1)^2}}{\nu\beta^2 - \nu + 1} - \left[ \sqrt{\frac{1 - 2\nu}{2 - 2\nu}} (\beta^2 + 1) - 1 \right]^{1/2} = 0.\tag{3.25}$$



Given a specific Poisson's ratio of the medium, (3.25) gives a unique  $\beta$  value. Using (3.23) and (3.24), each  $\nu$  value produces a solution set of  $\beta$  and  $\epsilon$  which is plotted in Fig. 3.2.

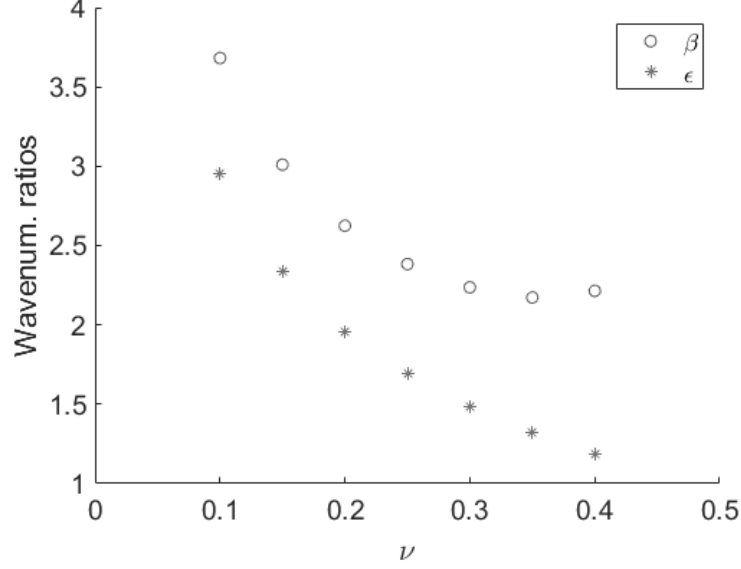


Figure 3.2: Diffusive relation between wavenumber of the fast and slow modes and the Poisson's ratio

By invoking the expressions for  $U_0$  and  $W_0$ , we obtain the displacement fields along the x and z directions as follow,

$$\begin{aligned}
 U_0 &= \left( A_0 k_1 e^{ik_1 x} - B_0 k_0 e^{ik_3 x} \right) i e^{-i\omega t}, \\
 W_0 &= \left( A_0 k_0 e^{ik_1 x} + B_0 k_3 e^{ik_3 x} \right) i e^{-i\omega t}.
 \end{aligned}
 \tag{3.26}$$

(3.26) consists of two traveling wave in the x-direction with two different wave numbers  $k_1$  and  $k_3$ . The solution pair for each  $\nu$  reveals that  $k_3 < k_1$  for normal matters with  $\nu$  between 0 and 0.5. In turn, the phase speeds  $c_3$  and  $c_1$  associated with the wavenumbers  $k_1$  and  $k_3$  with a constant fundamental frequency would suggest that  $c_3 > c_1$ . The two traveling wave inhibited in the displacement fields are termed the *fast* and *slow* modes. The spatial separation between the two traveling wave modes can increase as the displacement

fields propagates further and further away from the source, creating a diffusive interference pattern. The constructive interference only occurs when the relative phase shift between the two waves is small. The amplitude can be greatly reduced when the relative phase shift becomes significant.

The arbitrarily constants in (3.26) can be obtained by imposing the boundary condition at  $x = 0$ , which yields the following,

$$\begin{aligned} U_0 &= \frac{k_1 e^{ik_1 x} - k_1 e^{ik_3 x}}{1 + \beta \epsilon} \phi_0 i e^{-i\omega t}; \\ W_0 &= \frac{k_0 e^{ik_1 x} + \beta k_3 e^{ik_3 x}}{1 + \beta \epsilon} \phi_0 i e^{-i\omega t}, \end{aligned} \quad (3.27)$$

where the amplitudes of the displacement fields are functions of the wavenumbers associated with the fast and slow modes, the wavenumber ratios  $\beta$  and  $\epsilon$ . The dependency of  $\phi_0$  implies that both displacement fields will preserve the waveform of the imposed load at the application interface. In the case of ultrasonic piezoelectric material,  $\phi_0$  is often modeled with a Gaussian function.

### 3.2.2 Subsurface Response

Subsurface propagation below the half-space is governed by (3.9) and an assumed solution to the potentials is expressed as,

$$\begin{aligned} \phi_R &= A_R e^{i(k_{R,1}x + k_{R,2}z - \omega t)}; \\ \psi_R &= B_R e^{i(k_{R,3}x + k_{R,4}z - \omega t)}, \end{aligned} \quad (3.28)$$

where the subscript  $R$  denotes the wave mode existing in the subsurface region. Following the same analytical approach, the boundary conditions are expressed as follow,

$$W = \phi_0 k_0 i e^{i(k_0 z - \omega t)} \quad \text{for } x = 0; \quad (3.29)$$

$$U = 0 \quad \text{for } x = 0; \quad (3.30)$$

$$U_0 = \frac{k_1 e^{ik_1 x} - k_1 e^{ik_3 x}}{1 + \beta \epsilon} \phi_0 i e^{-i\omega t}; \quad (3.31)$$

$$W_0 = \frac{k_0 e^{ik_1 x} + \beta k_3 e^{ik_3 x}}{1 + \beta \epsilon} \phi_0 i e^{-i\omega t}. \quad (3.32)$$

By invoking the Helmholtz decomposition (3.3) at  $x = 0$ , (3.28) and (3.29) constraint the wavenumbers in the  $z$ -direction with the following relation:

$$k_{R,2} = k_{R,4} = k_0. \quad (3.33)$$

Similarly,

$$A_R k_0 + B_R k_{R,3} = \phi_0 k_0; \quad (3.34)$$

$$A_R k_{R,1} = B_R k_0.$$

Using the previously derived Rayleigh mode as the boundary condition at the half-space, the expressions for  $A_R$ ,  $B_R$ ,  $k_{R,1}$  and  $k_{R,3}$  can be obtained. That is,

$$A_R = A_0;$$

$$B_R = B_0;$$

$$k_{R,1} = k_1;$$

$$k_{R,3} = k_3. \quad (3.35)$$

The solution of the displacement fields below the subsurface can be expressed as follow,

$$\begin{aligned} U_R &= \frac{k_1 e^{ik_1 x} - k_1 e^{ik_3 x}}{1 + \beta \epsilon} \phi_0 i e^{i(k_0 z - \omega t)}; \\ W_R &= \frac{k_0 e^{ik_1 x} + \beta k_3 e^{ik_3 x}}{1 + \beta \epsilon} \phi_0 i e^{i(k_0 z - \omega t)}. \end{aligned} \quad (3.36)$$

(3.36) has important implications. The same wavenumber for both displacement potentials suggest both  $U$  and  $W$  are propagating at the same phase speed.

When transient load is introduced, the disturbance propagates within the waveguide with a finite speed. Below the half-space, it is translated into a phase shift  $\theta$  where  $\theta = k_0 z$  with  $z \in (0, L]$  added to (3.36) in  $x$  directional propagation. That is,

$$\begin{aligned} U_R &= \frac{k_1 e^{i(k_1 x + \theta)} - k_1 e^{i(k_3 x + \theta)}}{1 + \beta \epsilon} \phi_0 i e^{i(k_0 z - \omega t)}; \\ W_R &= \frac{k_0 e^{i(k_1 x + \theta)} + \beta k_3 e^{i(k_3 x + \theta)}}{1 + \beta \epsilon} \phi_0 i e^{i(k_0 z - \omega t)}. \end{aligned} \quad (3.37)$$

Compared to the half-space solution (3.27), the addition of phase shift of (3.37) infers a plane wave propagation geometry in the  $x$ -direction will incur a  $z$ -directional dependency. It renders the plane wave to have a curvature in the  $z$ -direction as it propagates along the half-space boundary. This result suggests the waveform integrity is maintained as it travels along the half-space with oscillations extending from the half-space boundary to the insertion depth  $L$ . This finding is unlike a typical Rayleigh excitation in which the Rayleigh mode only penetrates the medium by a few wavelengths.

### 3.3 Numerical Plane Geometry Model

The analytical finding in the previous section will be validated using a numerical technique employing the *differential algebraic equation*(DAE). This section details the load,

material assignment and boundary conditions of the steady state problem. The spatial diffusion and its dependency of the mechanical properties will be investigated. By imposing the same computational domain described in the previous section with the imposed steady state load. Elastic field measurement using the two-waveguide (transmission and reception) configuration will be compared against the ideal estimation.

### 3.3.1 Model Environment

Using the method of line (MOL), the differential operators  $\nabla$  in the Navier's equation (3.9) can be discretized linearly into a set of finite difference equations. By retaining the time-derivative expression, the resulted expression is referred to as the semi-explicit DAE (Brenan et al., 1996). This equation decouples the temporal and spatial parameters so each domain can be solved separately. To maintain both accuracy and numerical stability, the generalize- $\alpha$  technique is determined due to its accuracy and minimal damping in the high-frequency component (Jansen et al., 2000).

A 2D model is used to illustrate the propagation characteristics of the subsurface diffusive Rayleigh mode. The numerical model is built upon the latest model developed by (Lee et al., 2020), which utilizes the semi-explicit differential-algebraic equation technique. Fig. 3.3 depicts the modeling environment. The computational domain consists of a half-cycle isotropic medium to mimic the physical properties of wood, which has a density of  $480 \text{ kg m}^{-3}$ , Young's modulus of 1 GPa and a Poisson's ratio  $\nu$  of 0.4. A perfectly matched layer (PML) is constructed at the outer rim of the circle to create an unbounded medium in the radial direction by absorbing any reflections that could obscure the result.

The aluminum waveguide is inserted into the medium ( $\rho = 630 \text{ kg m}^{-3}$ , Young's modulus = 100 GPa,  $\nu = 0.33$ ), the side aperture of the waveguide and the medium is bonded to enforce the no-slip condition. The half-space is modeled as a free boundary to permit

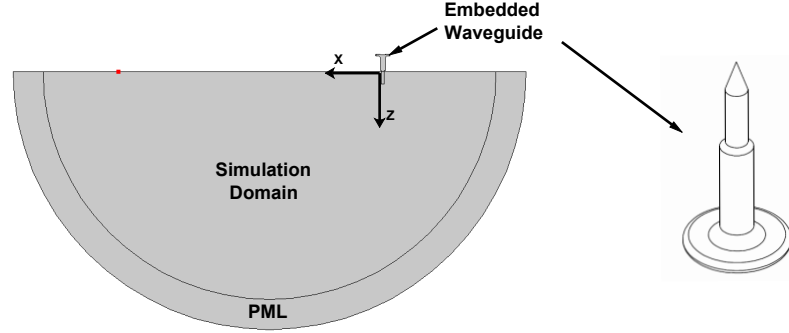


Figure 3.3: Simulation Geometry using COMSOL.

oscillation. To simulate a steady-state problem, a piece-wise function with a rising amplitude using a Gaussian curve combined with a constant amplitude to simulate steady-state wave propagation while maintaining smoothness at the transition. The quasi-stable load is imposed on the back flange of the waveguide to introduce the disturbance.

$$y = \begin{cases} e^{-\alpha(t-t_0)^2} \sin(\omega t) & t \in [0, t_0] \\ \sin(\omega t) & t \in (t_0, \infty) \end{cases} \quad (3.38)$$

where  $\alpha$  is the variance,  $\omega$  is the fundamental frequency of the transmitting signal, and  $t_0$  is a constant.  $t_0$  determines the temporal location of the maximal amplitude. A plot of this piece-wise function is illustrated in Fig. 3.4

### 3.3.2 Diffusive Propagation

At  $t = 0 \mu s$ , Fig. 3.5a and Fig. 3.5b depict clear displacement fields shortly after the disturbance is introduced. Due to the same phase speed at and below the half-space, both  $U_R$  and  $W_R$  fields travel away from the source while maintaining the plane wave geometry. In order to measure the diffusive effect, a displacement probe measuring the z-directional disturbance is placed at the half-space at 50, 200 and 400 mm away from the source, as shown in Fig. 3.6. The first measured disturbance is depicted in Fig. 3.7a, about 50 mm away

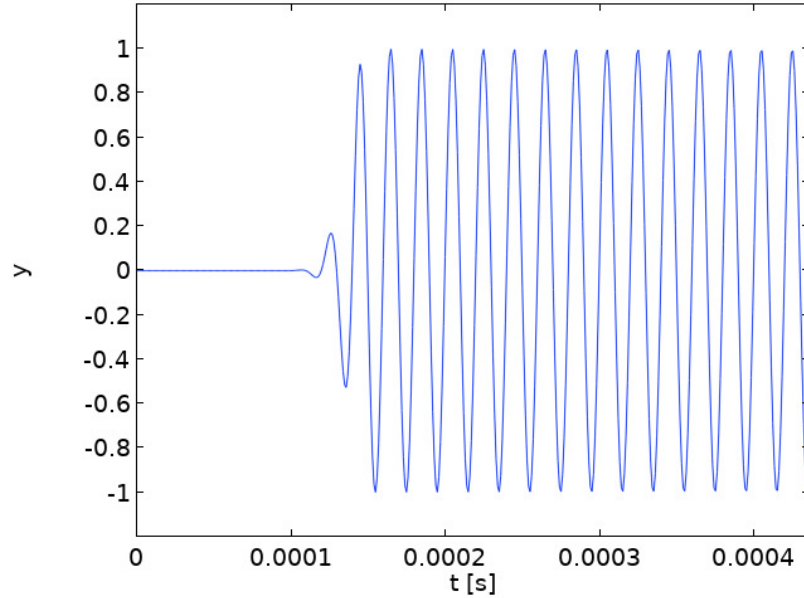


Figure 3.4: A piece-wise forcing function creating quasi-stable oscillation

from the source. The waveform contains the initial transient state about 0.2 ms, the following waveform exhibit steady-state oscillation similar to the imposed load. In Fig. 3.7b for measurement performed at 100 mm away from the source. The results illustrate the same transient and steady-state regions. There are some subtle differences in the transient region where small oscillations before 0.3 ms. In the steady-state region, the amplitude appears to be smaller and modulated with a sinusoidal function with the same fundamental frequency. A more pronounced diffusive effect is depicted in Fig. 3.7c. Oscillation is observed around 0.4 ms. After 0.6 ms, the steady-state is achieved. The amplitude in the steady-state is further decreased and amplitude modulation can be observed. The modulation might have been contributed by the initial transient amplitude that was not considered in the analytical formulation. Since this model does not model attenuation, the only contributing factor that causes the reduction in amplitude is the difference in phase speeds between the *fast* and *slow* modes. This result agrees with the previous analytical finding of the diffusive effect in Chapter 3.

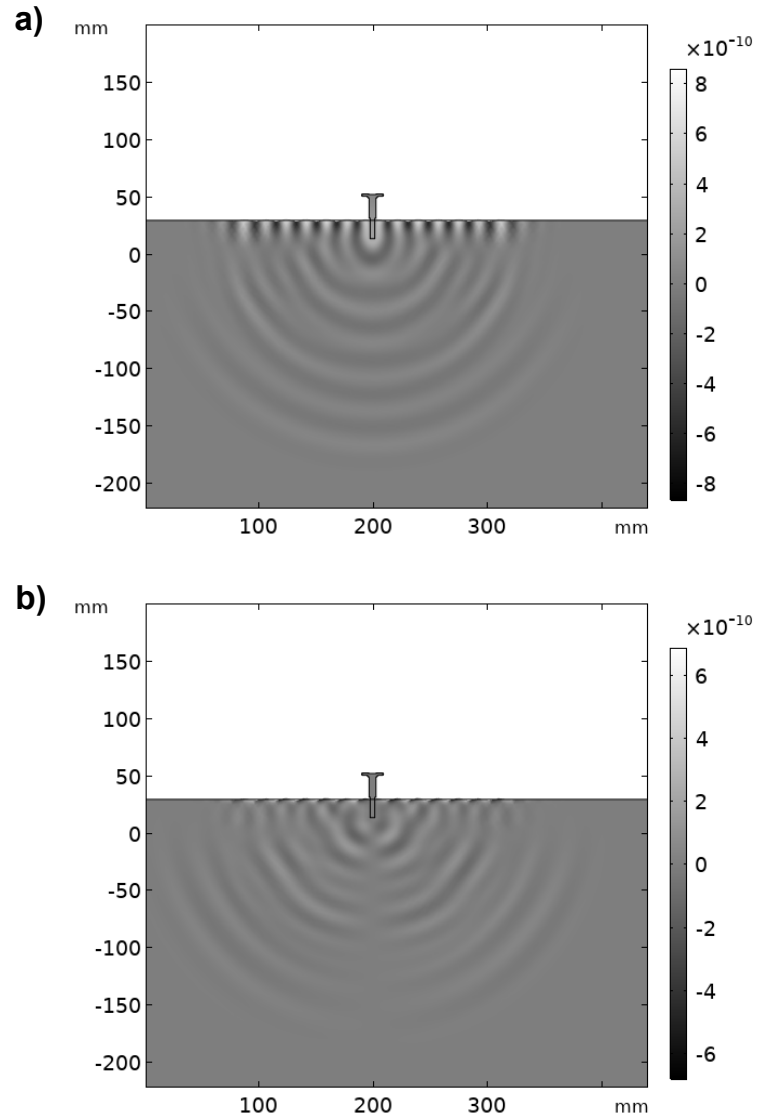


Figure 3.5: Simulated steady-state with  $W$  mode propagation in (a) and  $U$  mode propagation in (b).

In Fig. 3.8, the  $U$  displacement field exhibits similar diffusive behavior as the steady wave propagates away from the source. The amount of attenuation due to the interfering diffusion is different between the  $W$  and  $U$  fields. It is the coefficients of the fast and slow modes in the field formulation (3.27 and 3.36) that causes the different interference patterns resulting in greater attenuation.



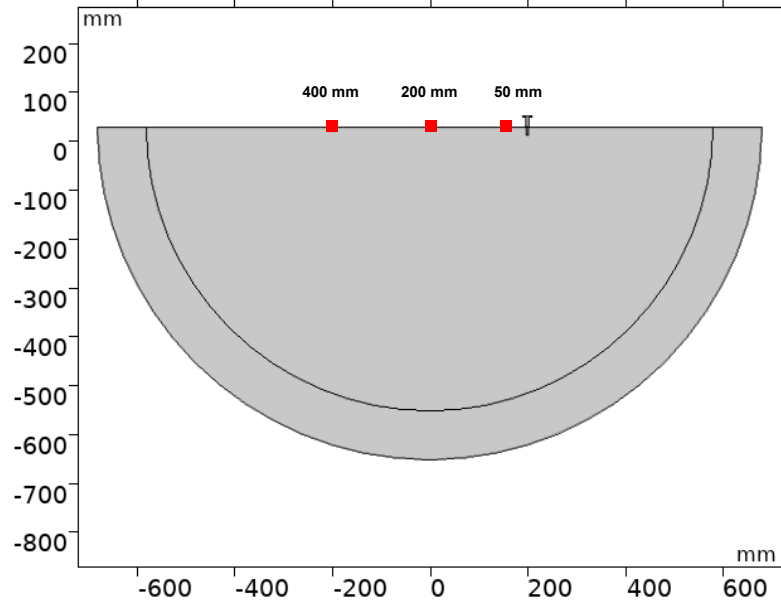


Figure 3.6: Placements of the displacement probes represented by the red dots.

### 3.3.3 Poisson's Ratio Dependency

This section validates the analytical finding from varying Poisson's ratios. Analytical results shown in Fig 3.2 infers that an increase of the Poisson's ratio from 0.2 to 0.4 amplifies the difference in wavenumbers between the two modes (fast and slow). In turn, the resulting waveform experiences a stronger diffusive effect. In this case, the displacement measuring probes are placed at a fixed distance of 200 mm away from the source the measure the waveform. Fig. 3.9 and Fig. 3.10 illustrate the measured  $U$  and  $W$  fields. The first detectable peak from both cases indicates that the Poisson ratio does not have any effect on the phase speed. The results also indicate the transition from the transient state to the steady-state occurs at around 0.6 ms. According to the analytical result, the reduction in amplitude is due to the difference in propagating speeds of the two different modes.

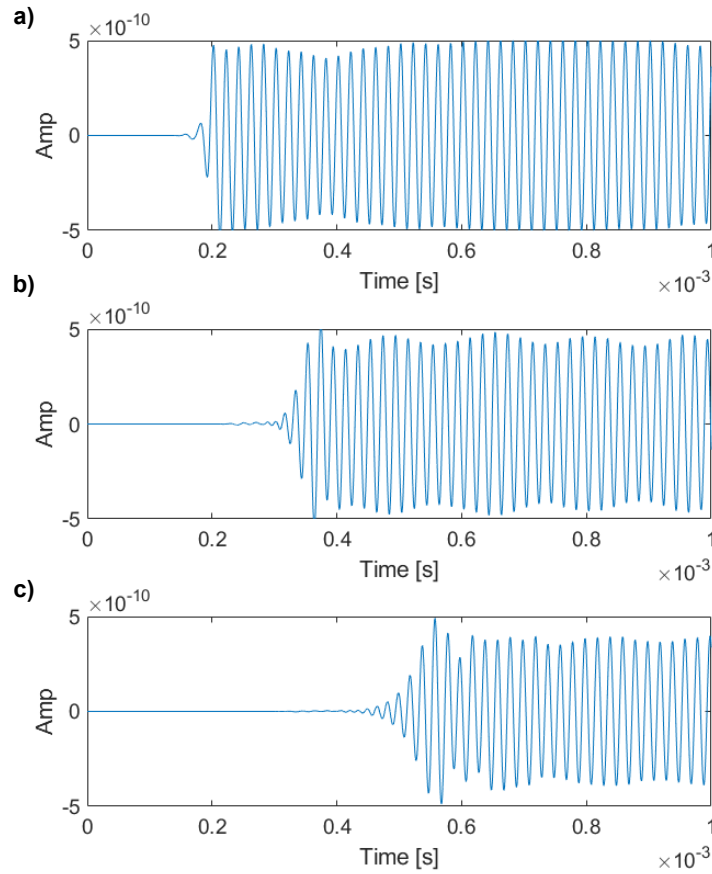


Figure 3.7:  $W$  displacement fields measured at a) 50 mm, b) 100 mm and c) 200 mm from the source.

### 3.3.4 Steady-State Waveguide Estimation.

In a realistic case, two identical waveguides are used to perform transmission and reception. This section focuses on the displacement estimation using the two-waveguide configuration to examine any variation between the theoretical and realistic estimation. That is performed by comparing the signals generated using the displacement probe and the insertable waveguide at the 50 mm from the source. The two results are depicted in Fig. 3.12. There is a pronounced attenuation of the displacement response. This can be explained from the governing wave equation. When an incident plane wave meets at the

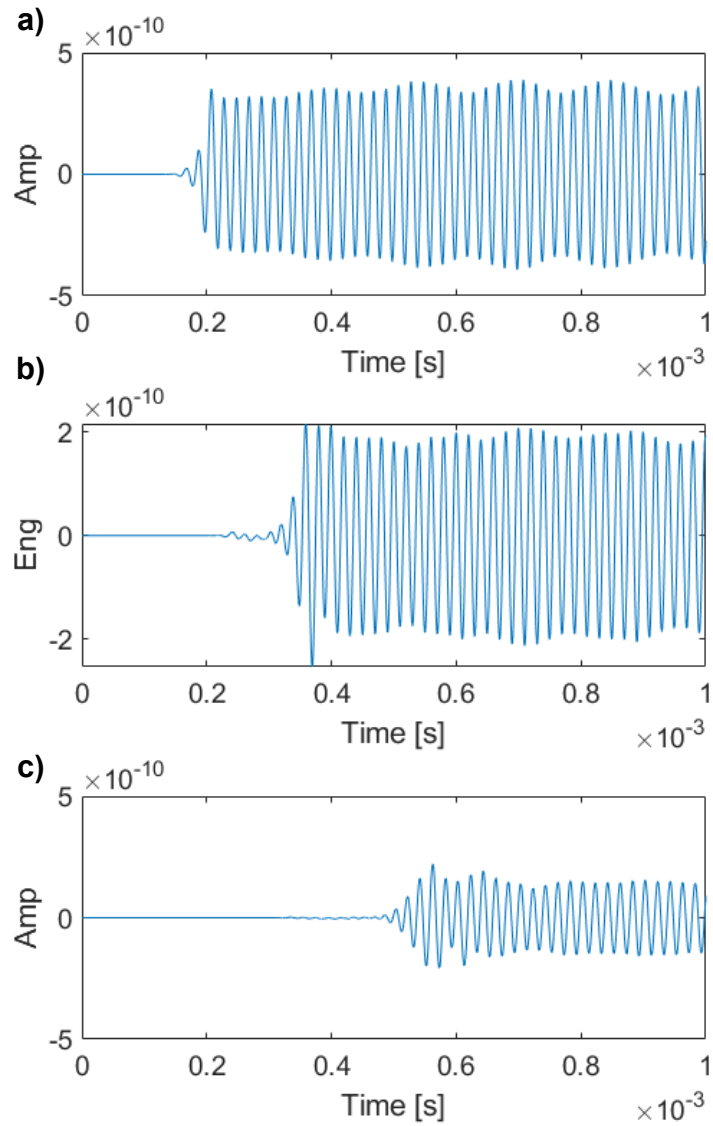


Figure 3.8:  $U$  displacement fields measured at a) 50 mm, b) 100 mm and c) 200 mm from the source

boundary of the two dissimilar materials, it partitions the incident wave into two wave modes: transmission and reflection. The reflection factor  $R$  and the transmission factor  $W$

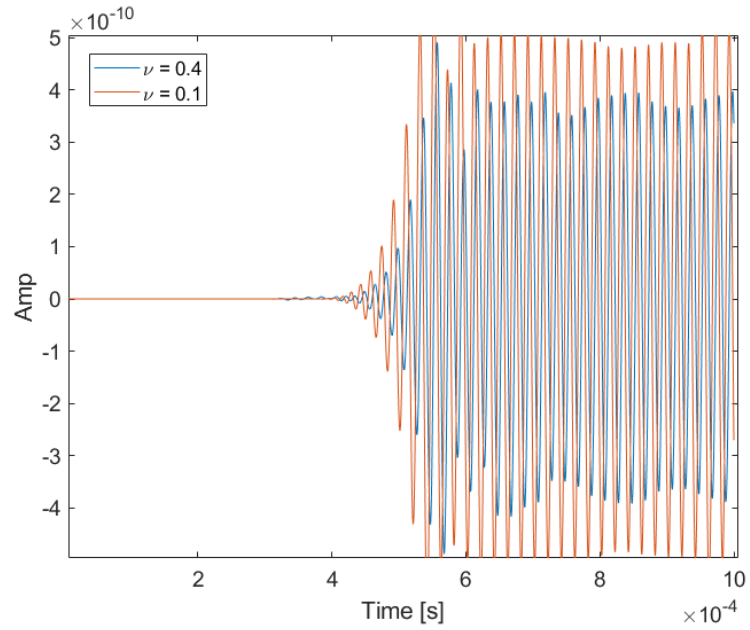


Figure 3.9:  $W$  displacement field at the half-space with different  $\nu$  values.

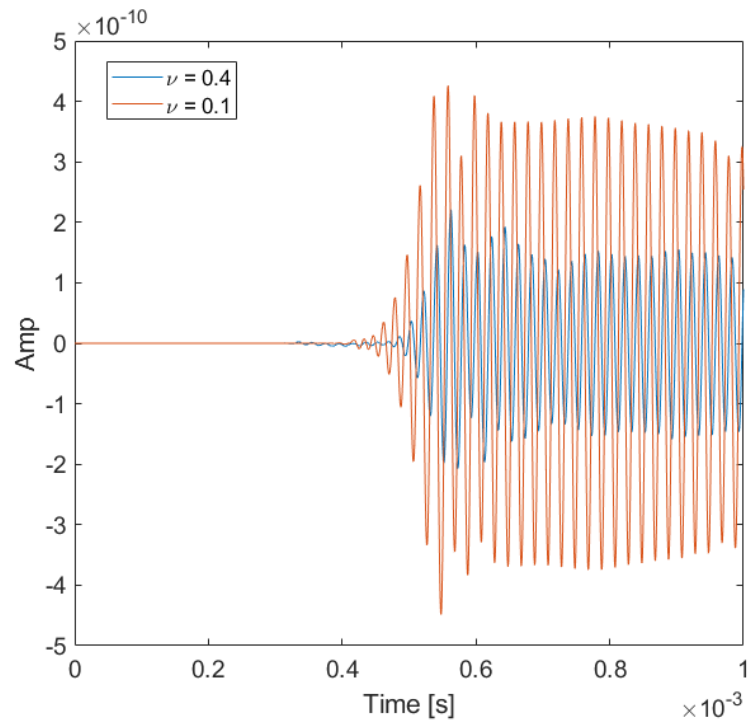


Figure 3.10:  $U$  displacement field at the half-space with different  $\nu$  values.

are expressed as,

$$R = \frac{W_2 - W_1}{W_1 + W_2};$$

$$W = \frac{2W_2}{W_1 + W_2'} \quad (3.39)$$

where  $W$  is referred to as the acoustic impedance expressed as  $W = \rho c_L$ . Since aluminum has higher acoustic impedance than the simulated wooden medium, attenuation is expected. Since acoustic impedance is only a function of the physical properties, its effect is invariant in time. A close examination reveals that the steady-state estimation maintains the frequency information compared to the ideal reference.

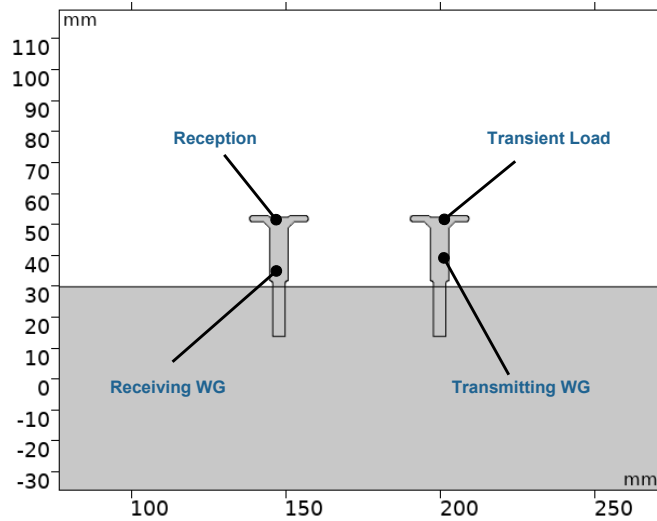


Figure 3.11: Two waveguide configuration.

### 3.4 Field Approximation under the Quasi-steady Limit

The introduction of elastic energy is often a transient process. In this section, a more realistic response of the Langevin transducer will be studied. After piezoelectric material is excited by an injection of modulated electrical energy, narrow-band transducers tend to

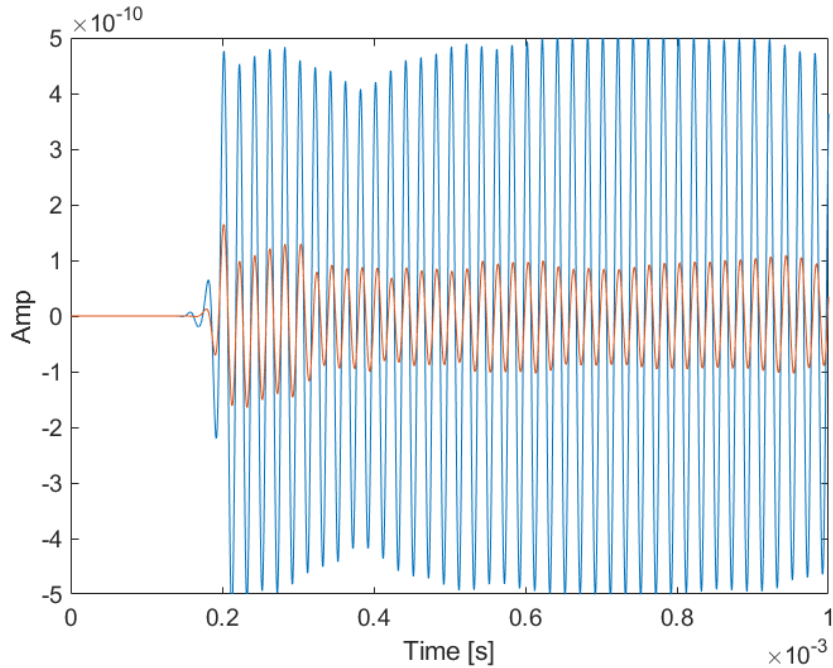


Figure 3.12: The waveguide response compared to the ideal response of the half-space displacement.

experience a long settling time (referred to as the "ringing"). It is interesting to apply the findings from the previous chapter to determine if a narrow band Langevin transducer is within the *quasi-steady* limit. In this section, the finite-element model developed from the previous chapter will be employed. The results will be compared to evaluate the quasi-steady state approximation.

### 3.4.1 Transient Response of Langevin Transducer

Narrowband transducers generate oscillations with longer rise and fall times, which in turn, exhibit the quasi-steady-state response. Broadband transducers produce low-intensity short pole signals when a high spectral resolution is desired. Due to the high attenuation acoustic properties of wood at higher frequency (Wassilieff, 1996) and strong impedance matching, high-intensity narrowband transducers with low resonant frequency are utilized.

A practical and elementary narrow-band transducer is the Langevin transducer. Its design components are illustrated in Fig.3.13a. A Langevin transducer consists of back section, piezoelectric ceramic layers, and the output section for delivering the elastic oscillations. The back section plays an important role of maximizing the energy throughput and damp out high frequency components in the output. Multiple layers of piezoelectric plates are sandwiched together, and metal film electrodes are inserted between each layer. The electrodes with opposing polarities produce voltage potential within each piezoelectric ceramic layer. A pre-tensioned bolt is threaded through each layer to increase the tensile strength to achieve a prestress in the order of  $300 \text{ kg cm}^{-2}$  (Gallego-Juarez, 1989). By pre-stressing the piezoelectric ceramic, mechanical energy is stored before the excitation which increases the amplitude of the output mechanical energy. Fig. 3.13b displays a constructed Langevin transducer as employed in this study.

The piezoelectric ceramic material can bi-directionally convert electrical energy into mechanical energy. Due to the complexity of the material response and its geometry relation, the nonlinear estimation of the time-dependent transient response can only be estimated using the classical wave equation. The geometric shape excites multiple vibration modes that often produce non-ideal mixed resonance (Uchino, 2012). The previous attempt at using FEM and 1D analytic result has produced useful results illustrated in Fig. 3.14. In this case, the piezoelectric plate experimented immediately after an excitation voltage is applied. The spectral graph Fig. 3.14b illustrates two fundamental modes occurring at about 5 MHz and 15 MHz, suggesting the excitation response of mixed resonance. The time-domain signal illustrates a clear oscillation with multiple frequencies with attenuating amplitude.

Based on the mixed resonance response of a typical piezoelectric plate, a waveguide is designed to filter other frequency components so that only the desired resonance is produced. The waveguide design is illustrated in Fig. 3.15. It primarily consists of the front

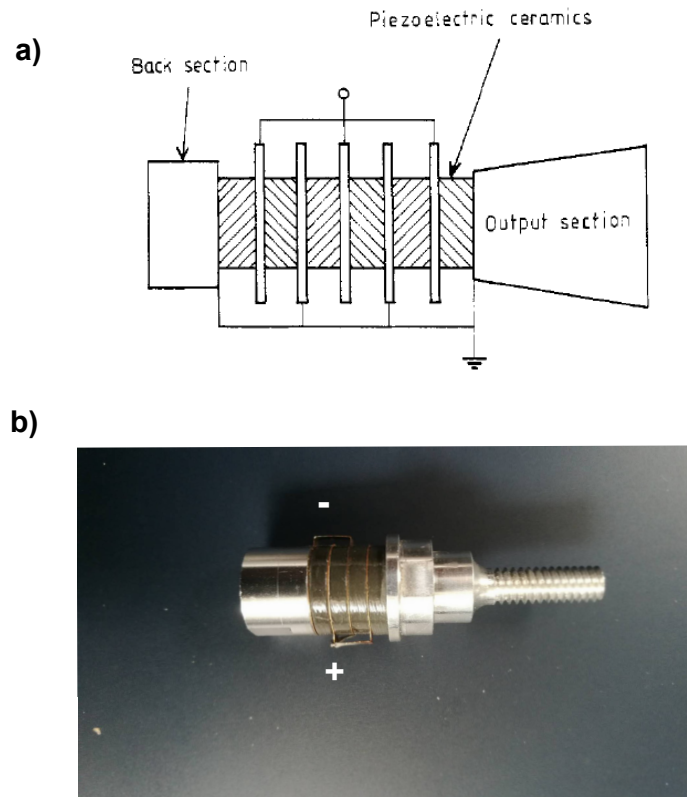


Figure 3.13: a) Design schematic of Langvin transducer. b) Exposed view of a manufactured Langvin transducer. (Cochran et al., 2012).

radiation aperture (17), back flange (18), the main shank (19), and the application interface. The radiation aperture is the portion of the waveguide that will be inserted into the wooden medium. The back flange provides the structural support allowing ultrasonic transducers to be mounted directly to the waveguide. The indented application interface is where Langevin transducer horn will be connected to the waveguide guiding the ultrasonic wave into the desired medium. The main shank (19) is wider than the radiation aperture to provide the necessary structural support when the waveguide is hammered into the medium.

Steady-state modal analysis is performed to ensure the maximal displacement is achieved at the pre-determined frequency. The displacement is measured at the front aperture. Through steady-state spectral and geometric optimizations, different physical dimensions were used to achieve an optimal eigenfrequency of 50 kHz while maintaining the physical



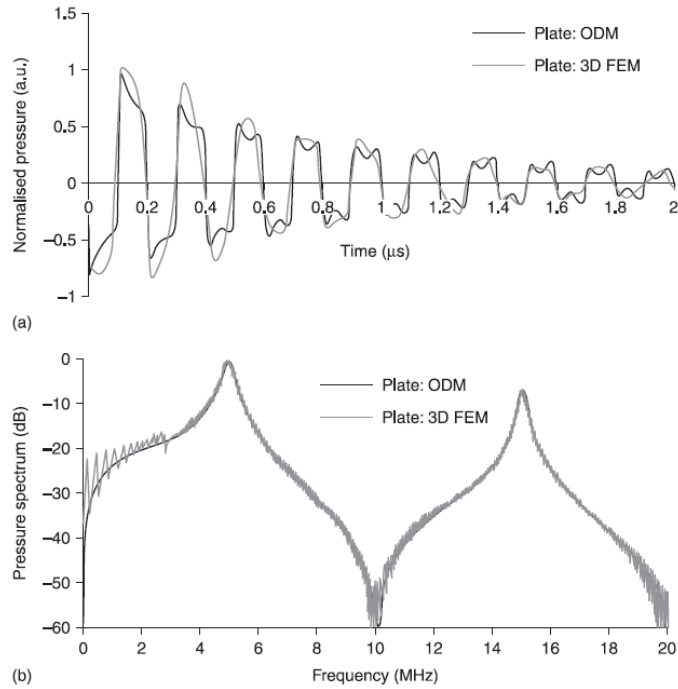


Figure 3.14: Time transient response of a piezoelectric plate (Cochran et al., 2012).

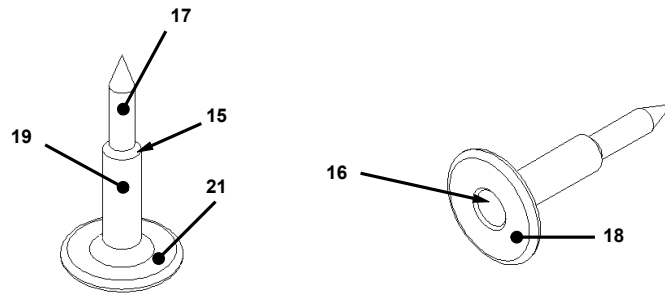


Figure 3.15: An illustration of the insertable waveguide.

requirement. Fig. 3.16 illustrates the spectral response of the waveguide. It shows that the resonance frequency is at 50 kHz, and the amplitude reduces rapidly for other frequencies. This spectral response is an ideal "bandpass filter" to reduce the effects of high frequency components.

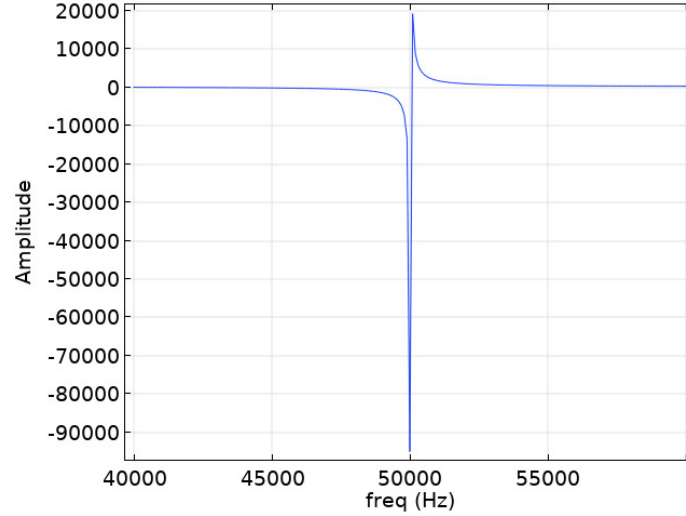


Figure 3.16: Spectral Response of the waveguide

### 3.4.2 The Spatial and Poisson's Ratio Dependencies

To illustrate the elastic wave propagation under the quasi-steady limit, the previously introduced finite-elements model in Chapter 3.3 is used with the same boundary condition. A square wave excitation response of a Langevin transducer can be simplified by a Gaussian modulated sinusoidal wave (San Emeterio et al., 2004) illustrated follow to model the transient load,

$$\sigma = \sigma_0 e^{-\alpha(t-t_c)^2} e^{-i\omega t} \quad (3.40)$$

where  $\sigma_0$  is the amplitude,  $\omega$  is the resonant frequency of the oscillating piezoelectric material,  $\alpha$  represents the bandwidth, and  $t_c$  is a constant denoting the time when the maximum amplitude occurs. The measured displacement waveform at 50 mm, 100 mm, and 200 mm away from the source is superimposed in Fig. 3.17. The three envelopes with different arrival times. The difference in arrival times indicates the same group speed suggesting the narrow-band propagation. As the transient waves propagate away from the source, the waveform displays a distinct amplitude reduction. Since artificial damping was not imposed in the model, the reduction in amplitude suggests the difference in phase speeds

between the fast and slow mode might have contributed. This finding is similar to the steady-state result. One more observation confirms the diffusive propagation by analyzing the wave envelopes. At 200 mm, the primary wave envelope is followed by a secondary wave envelope. This secondary wave envelope is less pronounced for 50 and 100 mm measurements, suggesting the two modes are more in phase resulting in stronger amplitude responses. In other words, the interference pattern produces a reduction of primary wave amplitude and a more distinct secondary wave envelope. Fig. 3.18 is the results of a study comparing the reduction of amplitudes between the steady-state and the quasi-steady state. As the wavefront propagates further away from the source, the diffusive behavior in the steady-state case is compared with the transient state. A similar level of amplitude attenuation and the close correlations in values strongly suggest the validity of employing the quasi-steady assumption. Henceforth, the fast and slow modes produced by the steady-state formulation can apply to the slow transient amplitude modulated ultrasonic signal using the quasi-steady limit.

The diffusive behavior as a function of the Poisson ratio is examined in Fig.3.2. Similar to the steady-state analysis, waveform measurements are conducted at 200 mm away from the source.  $\nu = 0.1$  and  $\nu = 0.4$  are examined. As recall, the phase speed difference between the fast and slow modes increases as the Poisson ratio increases. In Fig.3.2a, it is apparent that the reduction in amplitude in the primary envelope for  $\nu = 0.4$  followed by a more pronounced secondary envelope. Unlike the waveform with  $\nu = 0.1$ , the waveform is more in phase due to the small difference in phase speeds. Fig.3.19b shows the frequency response suggesting no shift in the fundamental frequency. The small spectral response suggests a greater destructive interference in the  $\nu = 0.4$  case.

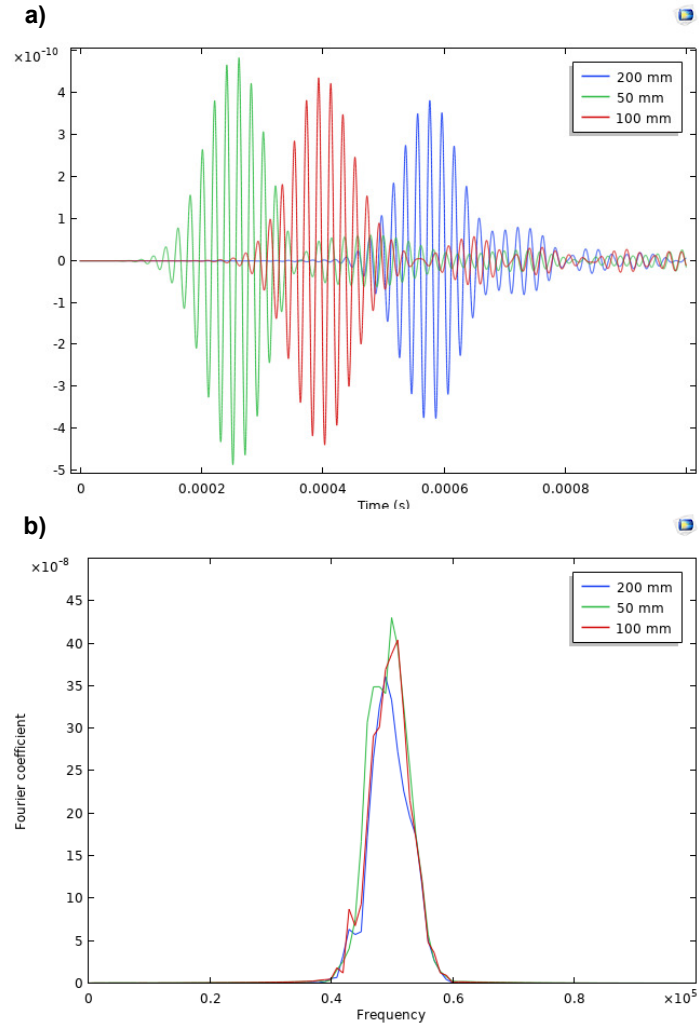


Figure 3.17: a) Temporal and b) spectral responses of the waveguide with  $\nu = 0.4$

### 3.4.3 Dual Waveguide Estimation of Transient Wave

It is critical to ensure that the dual waveguide sensing configuration does not introduce artificial disturbance that would destroy the actual waveform characteristics. In this case, the stress measuring probe is placed at the application interface of the receiving probe to mimic the elastic wave seen by the transducer. A comparative study between the displacement at the half-space and the stress measurement at the receiving probe is illustrated in Fig. 3.20. The time-domain responses are illustrated in Fig. 3.20a and Fig. 3.20b. Full width

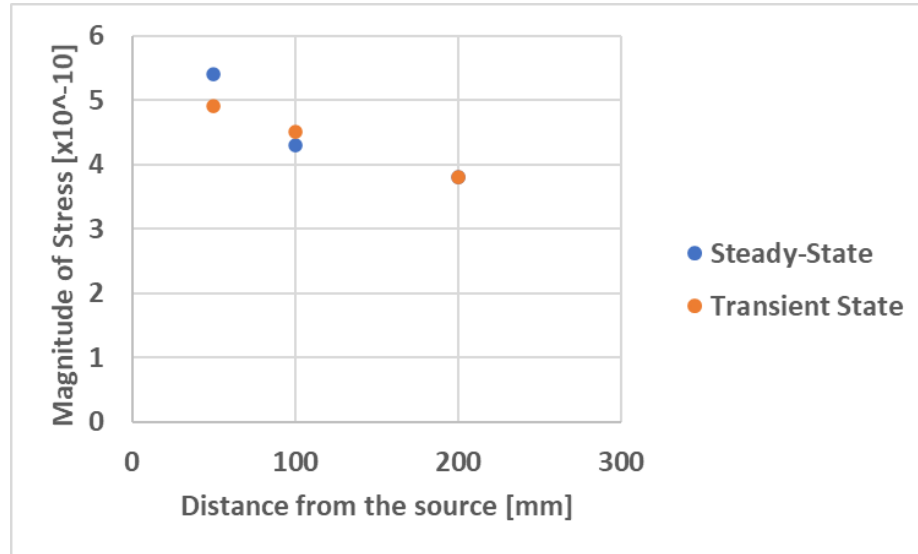


Figure 3.18: A comparison of the measured amplitudes between the steady-state and quasi-steady excitation mode with  $\nu = 0.4$

at half maximum (FWHM) is to measure the levels of diffusivity quantitatively. As the name implies, FWHM is defined as the width of the energy distribution at half-maximum. The ideal measurement produces an FWHM of  $120 \mu s$  while the waveguide approximation gives FWHM of  $110 \mu s$ , that gives an approximately 8% difference in the wave envelope in the time domain. It suggests that the embedded waveguide does not distort the waveform measurement. In the spectral response, which is depicted in Fig. 3.20c and d, Both response curves show the center frequency at 50 kHz with a bandwidth of approximately 10 kHz, an excellent indication in spectral estimation.

### 3.5 Summary and Discussion

This section has formulated the stress wave excitation using the designed embedded waveguide and the characteristics of its propagation. Under the flat geometry and the isotropic assumption, the resultant analytical solution gives rise to the diffusive property as a function of the Poisson's ratio. Below the half-space, the subsurface wave travels at

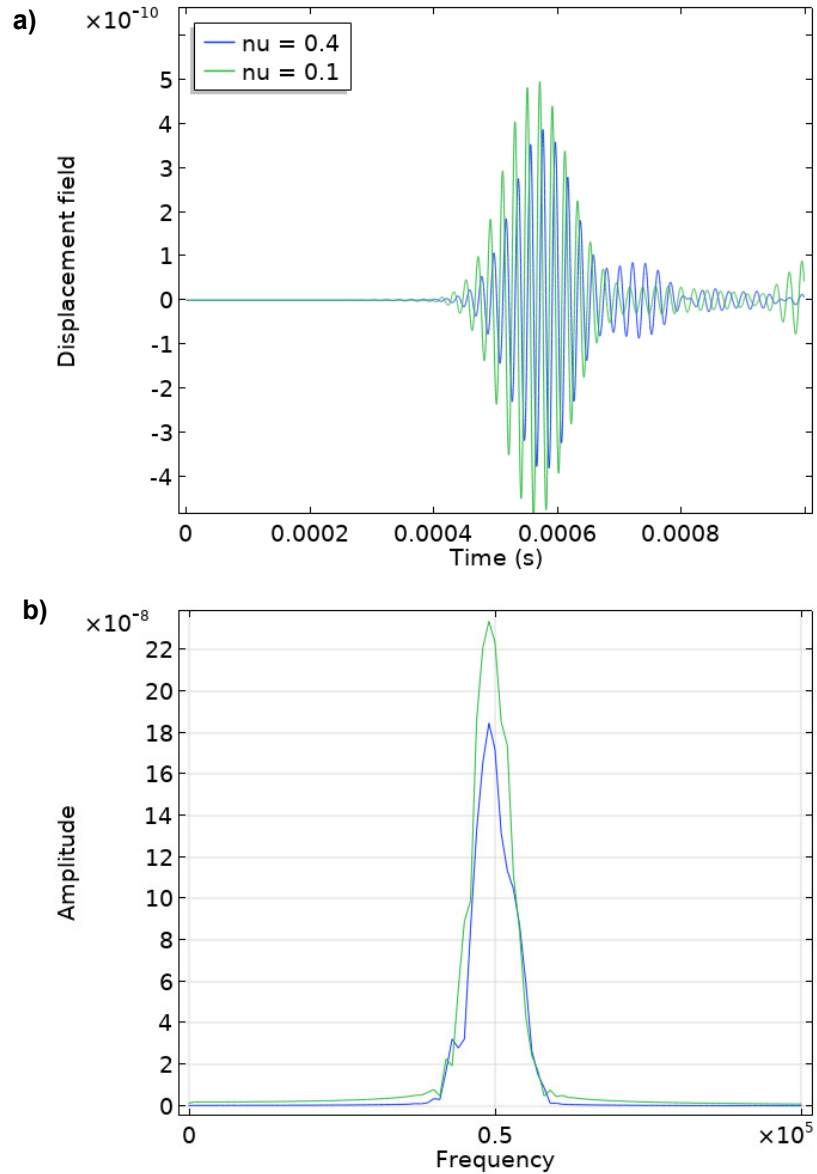


Figure 3.19: A comparison of the measured waveforms between the steady-state and quasi-steady excitation mode with  $\nu = 0.4$

the same phase speed as the surface wave allows the integrity of the wave envelopes to be maintained. This has an important implication of allowing the surface and the subsurface modes to characterize the shell region. The steady-state results can be used to approximate the response under the quasi-steady assumption, which is used to model the transient response of the Langevin transducer. Wooden materials possess Poisson's ratio between 0.3

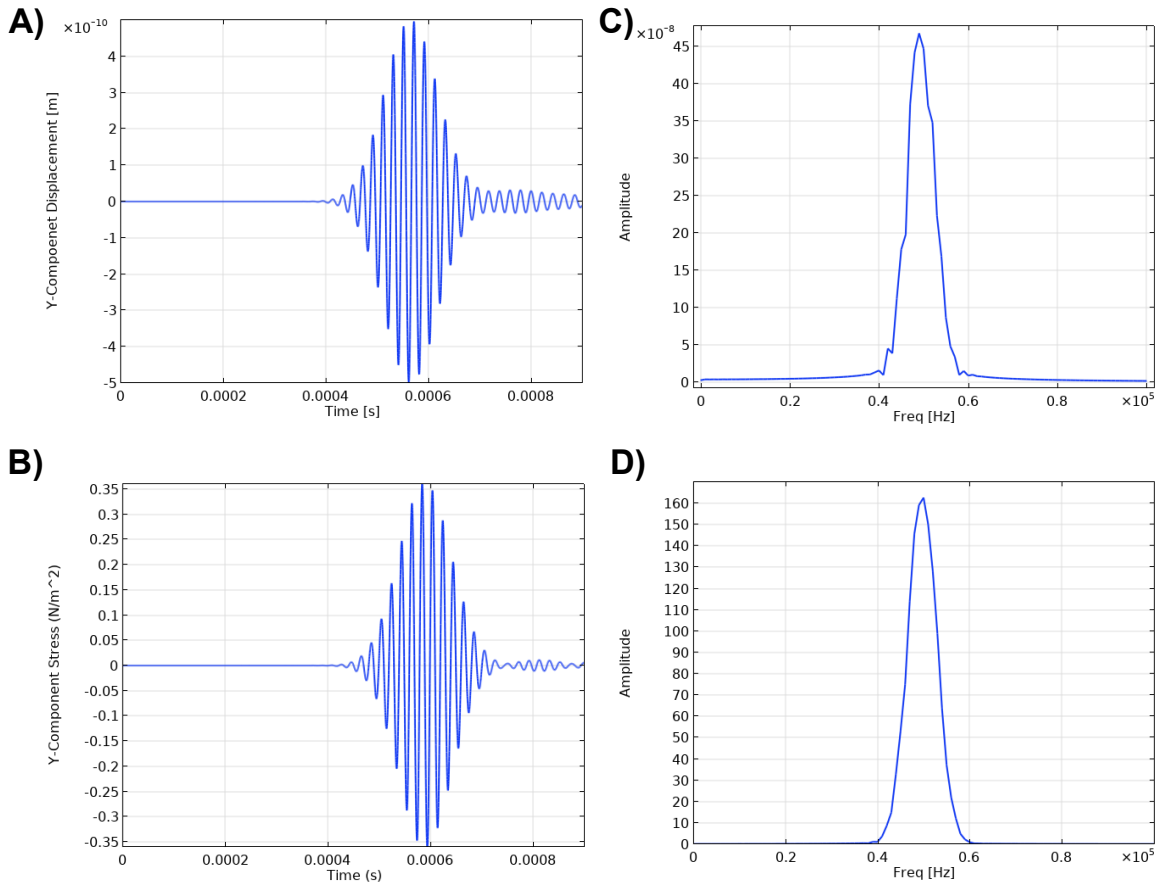


Figure 3.20: Transient response estimation of the waveguide. Subplot a and c show the ideal waveform in both temporal and spectral domains. Subplot b and d shows the waveform estimation using the proposed embedded waveguide design.

to 0.4 (Green et al., 1999). According to the finding highlighted in Fig 3.2, the diffusivity of the elastic propagation is insensitive to the change of the Poisson's ratio. Hence, this study does not focus on the diffusivity property of the elastic wave to characterize the material properties. In the next chapter, a numerical poroelastic model in the orthotropic medium will be developed and employed to analyze the effects of the excited Rayleigh mode under cylindrical symmetry.

## Chapter 4

# Numerical Model of the Orthotropic Porous Medium

Microscopically, wood generally consists of hollow fibers oriented in the longitudinal or axial direction transporting water and nutrients from the roots through the sapwood to the leaves. These fibers are called tracheids. Depending on the seasonal variation, the cycle creates springwood and summerwood with a varying density, as seen in Fig. 2.6. These fiber structures constitute about 90% of the wood. The remaining 10% is composed of short, hollow, brick-shaped ray cells oriented in the radial direction transporting food that is manufactured in the leaves down to the inner bark to support the growth of more wood fiber (Morrell, 2012). The microscopic view gives rise to orthotropic and poroelastic properties. It presents a great challenge of modelling the behaviors of any elastic wave propagation. This chapter is devoted to the numerical approximation of the medium. Using the proposed dual waveguide excitation and approximation technique, the resultant waveform in the orthotropic medium with cylindrical symmetry in the time domain is first studied. Using the Biot's model for porous media, the resultant spectral domain analysis will be added to the model to study its effects on Rayleigh wave propagation.



## 4.1 Numerical Model of Orthotropic Medium

### 4.1.1 Constitutive Equation of Motion

The orthotropic medium is defined as the mechanical properties with the axial dependency. By invoking the Navier equation in 3.1, the directional dependency of the physical properties can be represented by the Christoffel acoustic tensor  $C_{iklm}$ . Henceforth, the Navier equation in an unbounded orthotropic medium with a body force  $\sigma_{ij}$  can be transformed into

$$\rho \ddot{u}_i = C_{iklm} u_{k,lj} + \sigma_{ij} \quad (4.1)$$

where  $\ddot{u}_i$  denotes the second time derivative of the displacement field  $u$ , and it is often decomposed into the longitudinal and transverse potential fields through the Helmholtz decomposition. In the two-dimensional case, the stiffness matrix  $C_{iklm}$  describing an orthotropic medium in the cylindrical coordinate system is expressed as follows:

$$C = \begin{bmatrix} c_{11} & c_{12} & 0 \\ c_{21} & c_{22} & 0 \\ 0 & 0 & c_{33} \end{bmatrix} \quad (4.2)$$

with  $c_{11} = \frac{1}{E_R}$ ,  $c_{12} = c_{21} = -\frac{\nu_{TR}}{E_T}$ ,  $c_{22} = -\frac{1}{E_T}$  and  $c_{33} = \frac{1}{G_{TL}}$ , where  $E_R$ ,  $E_T$  and  $E_L$  are the Young moduli in the radial (R), tangential (T) and longitudinal (L) directions,  $\nu_{i,j}$  corresponds to the Poisson's ratios with the longitudinal deformation in the direction of stress  $i$  and shear deformation in the  $j$  direction, and  $G_{ij}$  are the shear moduli. Based on the empirical results generated by the U.S. Department of Agriculture (USDA), different elastic properties can be obtained from Taggart et al. (1999). Table 4.1 provides the numerical values for the typical wood species deployed in the utility pole industry.

	$c_{11}$	$c_{22}$	$c_{12}$	$c_{21}$	$c_{33}$
Douglas-fir	11.7	15.9	5.94	4.55	113
Red cedar	19.1	26	10.5	9.24	186
Red pine	13.1	17.9	5.5	5.36	128
White spruce	14.9	2.02	4.95	6.46	144

Table 4.1: Entries of the Christoffel acoustic tensor (Lee et al., 2020).

Under the cylindrical symmetry, the radial and tangential directions are shown in Figure 4.1. The estimated transient response of a Langvin transducer is applied on the excitation interface according to (3.40).

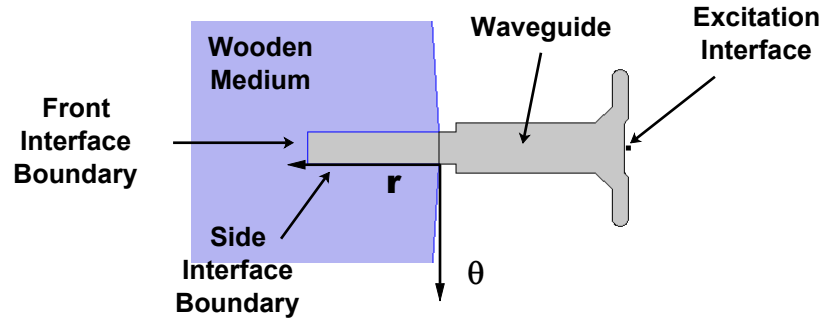


Figure 4.1: Geometry of the problem.

In order to discretize the constitutive equation (4.1) to be suitable for numerical implementation, MOL can be employed. This method allows the spatial derivatives to be transformed into a set of finite difference equations resulting in the so-called semi-explicit DAE. The backward differentiation formula (BDF) has known to be one of the most versatile and popular numerical techniques for solving a wide range of DAE problems. Hence, it is employed in this problem Bernan et al..

#### 4.1.2 Forcing Boundary

Based on the quasi-steady response of a typical narrow-band transducer, the boundary load of the elastic radiation can be modeled using the analytical form described in (3.40). Due to the geometry the GL region, the cylindrical symmetry formulation of the transducer

response is used. It can be described using the Gaussian model which yield the following transient expression:

$$\sigma_{rr}|_{r=b} = \sigma_0 e^{-\alpha(t-t_c)^2} e^{i(kL-\omega t)} \quad \text{for } |\phi| \leq a, \quad (4.3)$$

where  $k$  is the wave number. At the half-space of a utility pole at the ground line (GL), the boundary condition along the circumference of the cross-section can be reasonably assumed to have zero longitudinal and shear stresses. That is,

$$\sigma_{rr} = 0, \quad \sigma_{\theta r} = 0 \quad (4.4)$$

### 4.1.3 Effective Properties and Computation Upscaling

As previously mentioned, the irregular cellulose structure produces both microscopic and macroscopic properties depending on the spatial scale. Its mechanical properties depend on the morphology of the cellulose and the physical properties of the cell walls. Due to the microscopic anisotropy, if the elements are to consider the microscopic structure, it will present an abnormous computational challenge. Therefore, a technique called computational upscaling is utilized by replicating a single cell to a multi-cell structure. The dimensional dependency can reduce and give rise to the so-called effective properties. Fig. 4.2 shows that as the cell structure continues to replicate, the physical properties converge to values at which we termed the effective properties. It is apparent that the notion of effective properties helps produce realistic results without incurring excessive computational complexity. It helps establish the smallest element size. In order to resolve the waveform, the Nyquist-Shannon theory constrains the smallest element size. Based on the constraints of the effective properties and the constraints of the sampling theory, a study conducted by (Lee et al., 2020) has summarized the wood species that are commonly used for poles.

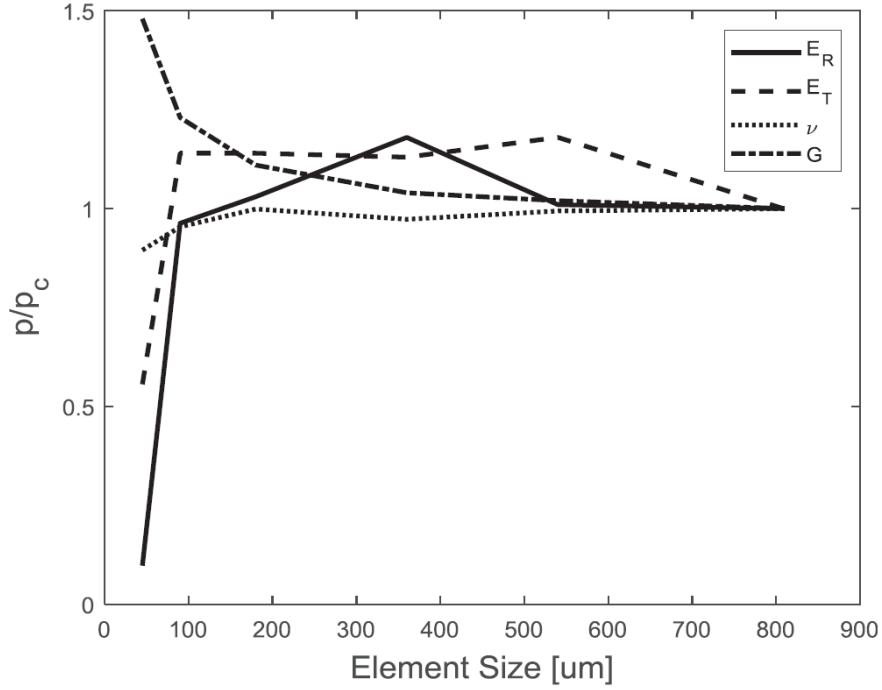


Figure 4.2: Homogeneity and convergence of physical properties from Douglas-fir (Lee et al., 2020).

#### 4.1.4 Time stepping and Numerical Stability

There are two main requirements in selecting the appropriate time step. The first requirement is to avoid aliasing in the signal. This can be determined using the Nyquist-Shannon sampling theorem which states that the sampling frequency needs to be at least twice of the center frequency (Shannon, 1949). Be conservative, the time step is set to be at least ten times greater than the fundamental frequency to avoid aliasing.

	Min. Element Size [ $\mu m$ ]
<b>Douglas-fir</b>	613
<b>Red Cedar</b>	361
<b>Red Pine</b>	702
<b>White Spruce</b>	663

Table 4.2: Maximum element size for each species in order to employ the computational upscaling technique (Lee et al., 2020).

Since the orthotropic wave equation contains non-linear terms, the issue of the stiffness of the PDE requires the numerical technique to be more resilient to any numerical instability (Kassam and Trefethen, 2005). It demands the numerical method to be capable of controlling the truncation and interpolation errors during the solution process. In this study, different sizes of time-stepping are used to observe the local relative errors by comparing the predicted values and approximated value at every time step. By definition, the relative local error is defined as follows (Brenan et al., 1996),

$$\text{ERR} = M \left\| u_{n+1} - u_{n+1}^0 \right\| \leq 1.0, \quad (4.5)$$

where  $u_{n+1}^0$  contains all the predicted values based on the predictor formula Krogh (1974), and  $u_{n+1}$  contains the approximated values.  $\|\cdot\|$  denotes the  $L_2$  norm.  $M$  is a coefficient related to a chosen step size. Figure 4.3 illustrates the relative error using different step sizes. Although small step sizes provide a better temporal resolution, it increases computational time. As illustrated in Figure 4.3, the diminishing in return helps justify an efficient time step while maintaining small relative error.

#### 4.1.5 Case Study: Time Domain Analysis

Under the orthotropic medium, this section briefly describes the numerical results by analyzing the wave emission and propagation pattern. The cylindrical symmetry of orthotropic medium according to data compiled by the US Forest Services (Green et al., 1999) provide the detail information about the physical properties of the medium. Due to the wide adaptation of Douglas-firs in the utility industry, its physical properties from the database were used for demonstrating the result. The justified transient load based on the nonlinear response of the Langevin transducer is used, and an approximate elastic response is depicted in Fig. 4.4.

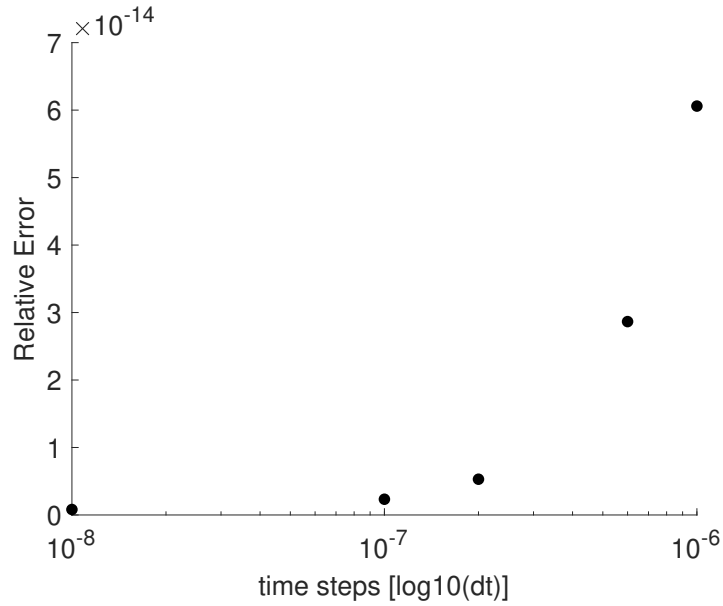


Figure 4.3: Relative error of different step sizes (Lee et al., 2020).

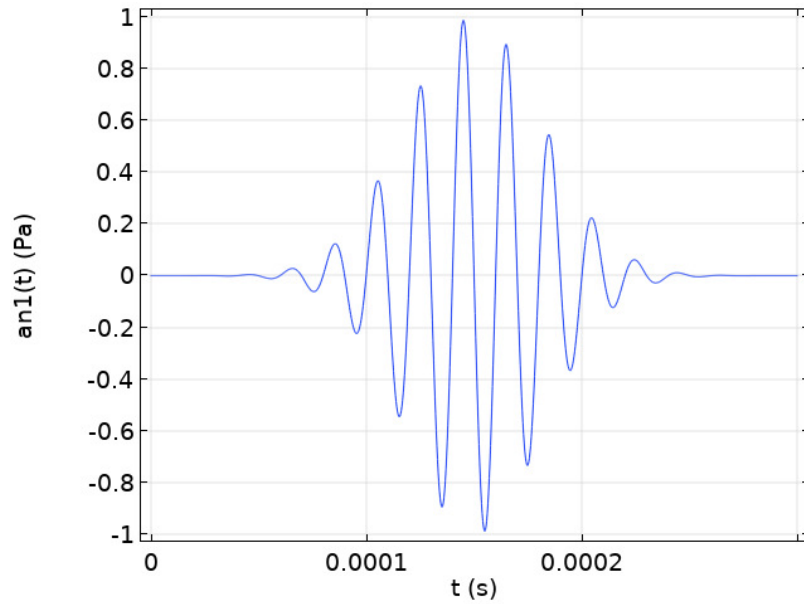


Figure 4.4: Imposed transient response to simulate a typical narrow-band ultrasonic transducer

The elastic disturbance imposed at the application interface is guided through the shank of the waveguide and into the interior of the medium. The immediate unbounded medium allows the wavefront to expand outward. Due to orthotropic variations in physical proper-

ties within the medium, the propagating speed differs both tangentially and radially. Hence, it results in a beam pattern shown in Fig. 4.5a. This similar pattern has been previously predicted by (Rose, 2004). For the purpose of comparison, a snapshot of the emission pattern created in an isotropic medium is shown in Fig. 4.5b. It depicts a uniform and spherical expansion of the elastic wave due to the directional dependency of the physical properties. (Lee et al., 2020) further analyzed the longitudinal and transverse wave modes and compared with other similar model (Senalik et al., 2010) in order to validate this model.

Based on the imposed traction-free condition and the assumed longitudinal mode, the side interface excites longitudinal stress wave oscillating in the radial direction. The propagation of Rayleigh mode in the curved half-space boundary is often termed *surface mode*. This mode consists of both the longitudinal  $\phi$  and the transverse displacement components  $\psi$  which can be expressed analytically as (Viktorov, 1967),

$$\begin{aligned}\phi &= Ae^{ip\theta} I_p(k_l r); \\ \psi &= Be^{ip\theta} I_p(k_t r),\end{aligned}\tag{4.6}$$

where A and B are the amplitudes,  $I_p$  is the Bessel function of an order p, where p is the angular wave number expressed as  $2\pi R\lambda$ ,  $\theta$  is the tangential direction,  $k_l$  and  $k_t$  are the wave numbers for the longitudinal and tangential wave numbers expressed as  $k = 2\pi/\lambda$ . This mechanism is illustrated in Fig. 4.6 by observing the enhancement of the stress level around the circumferential region at different times.

By employing the dual waveguide configuration which measures the stress received, the wave mode excited by the front interface and the Rayleigh surface mode excited by the side interface are captured in Fig. 4.6. Three different time frames are recorded corresponding to different wave modes generated by the embedded waveguide. The first arrival labeled AW1 is generated by the direct radial trajectory at  $t = 360 \mu\text{s}$  (Fig. 4.6a). This is a small

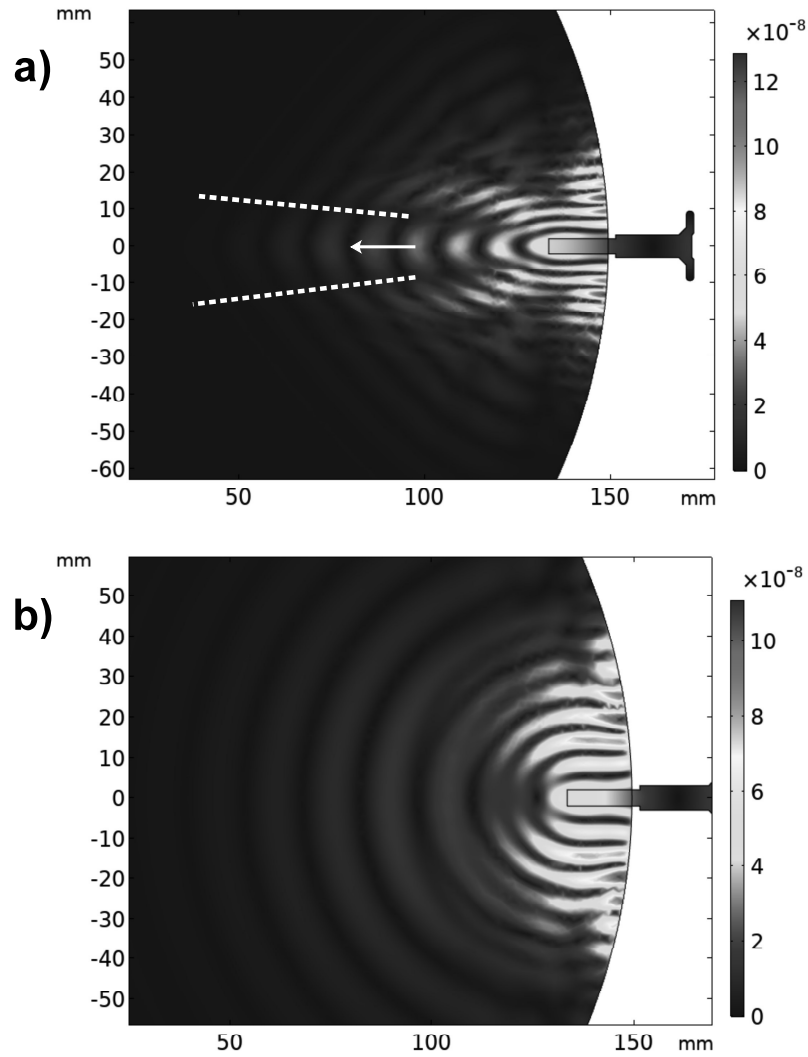


Figure 4.5: Magnitude of the displacement fields at a) orthotropic medium where the dotted white lines denote the beam width boundary and the white arrow denotes the energy vector. b) Isotropic medium using average properties.

amplitude due to the outward expansion of the energy through a small frontal area. The second arrival labeled AW2 arriving at  $t = 560 \mu\text{s}$  is produced by the similar mechanism. The outer boundary however reflects most of the elastic energy back toward the receiving waveguide creating a slightly larger wave amplitude (Fig. 4.6b). This mechanism is often referred to as the *Snell's law*. In the process, the so-called mode conversion converts a portion of the stress energy from the longitudinal to transverse mode. This trajectory follows



the half-space boundary in the tangential direction. As a very rough estimate, the group TOFs of the two different arrivals have the ratio of approximately 1.55, which agrees with the ratios of the distances of the two arrival waves. This finding suggests that the dispersive relation between the AW1 and AW2 are the same, producing the same group velocity.

The focus is the arrival mode labeled AW3. At  $t = 890 \mu s$ , the signal response is the strongest due to the larger contact interface between the medium and the waveguide (Fig. 4.6c). However, this is not always the case. When decay and high moisture content exist in the shell region, high attenuation in the signal can result in a lower amplitude response. This concept will be revisited in the later chapters. The AW3 is the result of symmetric wave propagation in both *clockwise* and *counter-clockwise direction*. The arrival time is much longer than the AW2. This is due to the significant difference of group velocities between AW1 and AW3. Since this study focuses on narrow-band transducer, the dispersive relations of AW1, AW2 and AW3 are not further investigated here. However, the phase speed of AW3 can be found in Fig. 3.2.

Table 4.3 shows the estimated arrival measured based on the highest peak amplitude value. This technique is more accurate in determining TOF when a single-frequency elastic wave is introduced into the medium because any attenuation in energy will not alter the time of the peak energy. The normalized ratio (NR) is calculated based on the following expression  $NR = TOF_i/TOF_1$ , where  $i$  denotes the arrival wave number. This expression compares the TOFs of different arrivals to the initial arrival mode. As an interesting observation, the NR of AW2 is 1.56. This is the same as the ratio of the distances of the two arrivals. This is realized by examining the simulation result. AW1 corresponds to the radial propagation, while AW2 is a result of mode conversion when the wavefront interacts with the half-space boundary. This observation helps validate the model and confirm the trajectory of AW2. The AW3 has a much greater NR value because of the curvature of the boundary that changes the group speed of AW3 predicted by (Viktorov, 1967).

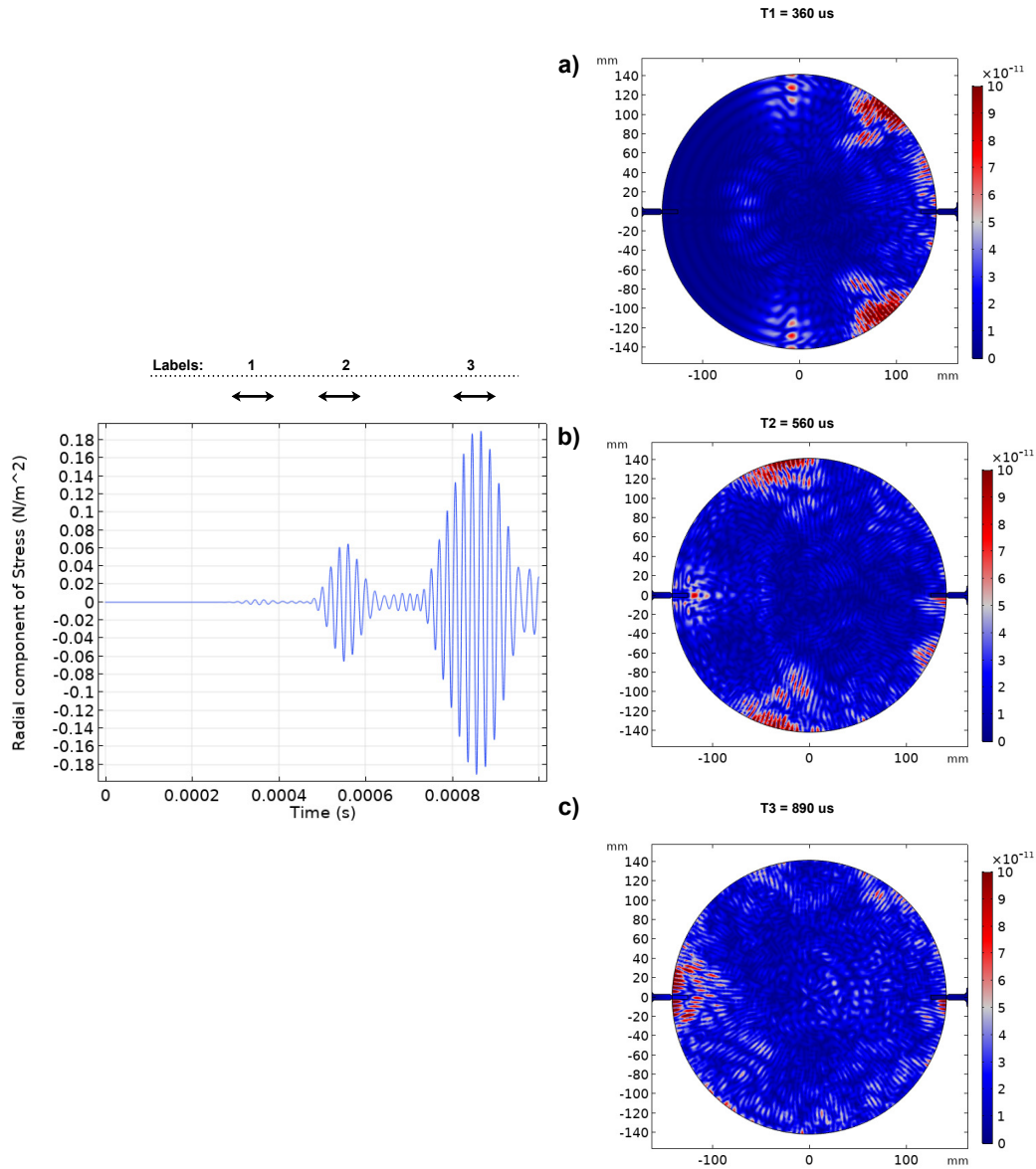


Figure 4.6: Received time-domain signal with the corresponding states of wave propagation at a)  $t = 360 \text{ us}$ , b)  $t = 560 \text{ us}$  and c)  $t = 890 \text{ us}$ . (Lee et al., 2020)

The diffusive effect of the Rayleigh propagation can be observed by measuring the FWHM of the waveform. To demonstrate this scenario, receiving waveguides are placed at the  $180^\circ$  and  $20^\circ$  relative to the transmitting waveguide. The resultant waveforms are illustrated in Fig. 4.7. Subplot a) shows the waveguide positioning at  $180^\circ$ , the FWHM is measured to be approximately equal to  $150 \mu\text{s}$ . Subplot b) shows the waveguide posi-

Arrival Wave	TOF	Normalization Ratio
AW1	360	1
AW2	560	1.56
AW3	890	2.47

Table 4.3: The arrival time of the different wave modes

tioning at  $20^\circ$ , and the measured FWHM is estimated to be  $80 \mu\text{s}$ . This difference in the width of the wave envelop help further validate the finding of the diffusive effect and more importantly, it suggests the finding from the plane geometry propagation also applies in the convex curvature.

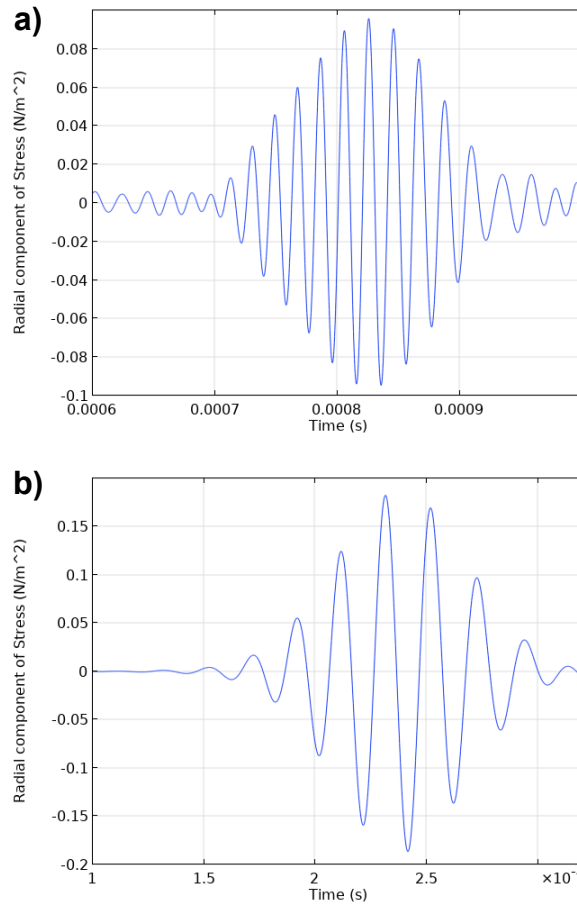


Figure 4.7: Received time-domain signal with the corresponding states of wave propagation at a)  $t = 360 \mu\text{s}$ , b)  $t = 560 \mu\text{s}$  and c)  $t = 890 \mu\text{s}$ . (Lee et al., 2020)

#### 4.1.6 Case Study: Variations in Mechanical Properties

When a wood pole experiences the first stage of decay (often referred to as the incipient decay), fungal agents produce digestive enzymes (Schmidt, 2006) by destroying normal tissues on the wood cell walls. This process alters the original cell structures and degrades its physical properties. A direct contribution to the reduction of its overall strength. In the early stage, the mechanical properties decrease by 10% before any sign of mass loss can be detected (Highley, 1999). Fig. 4.8 illustrates empirical result conducted by S.F. Curling (Curling et al., 2002). It illustrates the extent of the decay over time and compares the difference between mass loss and MOR, MOE and work to maximum load (WOM). Recent studies are focusing on the specific decay mechanisms and the targeted mechanical property degradation (Schubert et al., 2006) and (Winandy and Morrell, 1993). Employing the findings from the prior research, the data are incorporated into the model to investigate the impact on the waveform in the temporal domain.

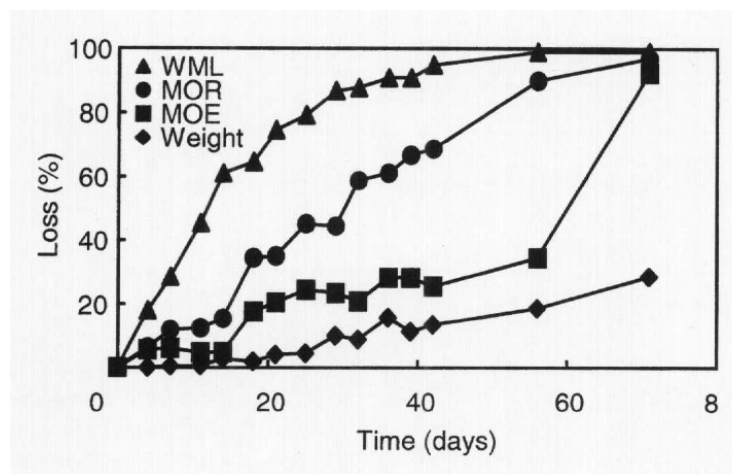


Figure 4.8: An excerpt illustrating the correlations between decay on various mechanical properties (Curling et al., 2002).

To simulate wooden pole with incipient decay, according to Fig. 4.8, both Young's modulus and the Shear modulus incur 20% reduction. The density remains constant in

both cases. The time domain signal is portrayed in Fig. 4.9. The AW1 are relatively the same in both cases. The AW2 and AW3 on the other hand, have a distinct difference in group velocities. That is evidenced in the reduction of the elastic moduli. The shift in group velocity signifies a slower propagation velocity. This finding can be realized by the constitutive equations governing the Rayleigh mode. The longitudinal and transverse wave numbers are inversely proportional to the elastic moduli. This shift can be detected by measuring the temporal location of the peak energy. The specific analysis technique will be further discussed in Chapter 5.

A distinct reduction in peak energy is depicted in Fig. 4.9. By measuring the FWHM, the pole without the property degradation is  $150 \mu\text{s}$ , and the pole with degradation is  $160 \mu\text{s}$ . It suggests no further diffusive effect due to deterioration of its properties. This can be explained by invoking one of the *Lamé* relations of homogeneous isotropic material which states that,

$$\nu = \frac{E}{2G} - 1 \quad (4.7)$$

where  $E$  is the Young's modulus and  $G$  is the Shear modulus. Since both elastic moduli were reduced by 20%, the Poisson's relation  $\nu$  remains relatively constant.

## 4.2 The Poroelastic Formulation

In poroelastic material, the solid and fluid media interaction forms aggregated motions. Unlike elastic properties of the solid medium, the compression of fluid is an *irreversible* process. It generates heat that will quickly dissipate into the environment. Under the poroelastic region limit in which the ultrasonic wave operates, the solid and fluid media interact to form aggregated motions. Unlike the elastic properties of a solid medium, the compression of fluid within the voids is an irreversible thermodynamic process. It results

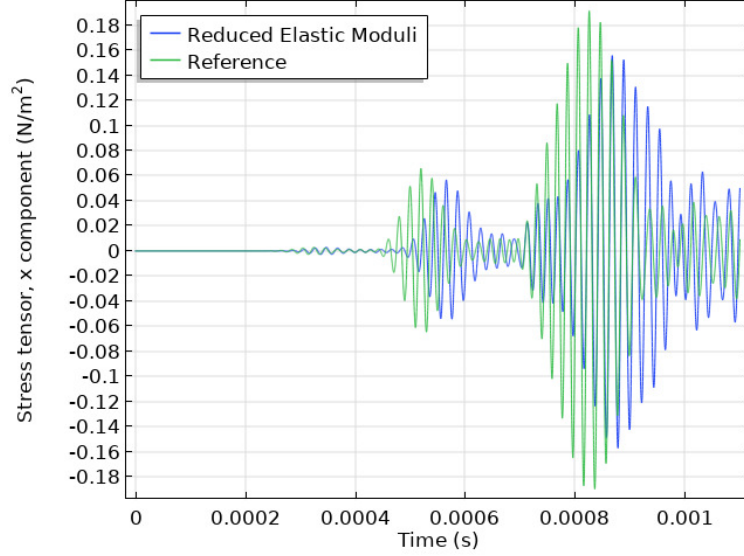


Figure 4.9: A comparative result of waveforms between healthy pole and pole with simulated incipient decay.

in added damping in the wave propagation which is referred to as the *viscous damping*. The early work produced by M.A. Biot (Biot, 1956) laid out the foundation which becomes the model of poroelastic medium. According to (Biot, 1956), using Langrangian formulation, the energy propagation in the poroelastic medium adds energy dissipation in terms of the viscous damping. That is,

$$\begin{aligned}
 \rho_{11} \frac{\partial^2 \mathbf{u}}{\partial t^2} + \rho_{12} \frac{\partial^2 \mathbf{U}}{\partial t^2} &= P \nabla \cdot (\nabla \mathbf{u}) + Q \nabla (\nabla \cdot \mathbf{U} - N \nabla \times (\nabla \times \mathbf{u})) \\
 \rho_{12} \frac{\partial^2 \mathbf{u}}{\partial t^2} + \rho_{22} \frac{\partial^2 \mathbf{U}}{\partial t^2} &= Q \nabla (\nabla \cdot \mathbf{u}) + R \nabla (\nabla \cdot \mathbf{U})
 \end{aligned} \tag{4.8}$$

where  $\mathbf{u}$  denotes the solid displacement field,  $\mathbf{U}$  denotes the fluid displacement field,  $\rho_{mn}$  is referred to as the "mass coefficients" relating the densities of solid and fluid phases.  $P$ ,  $Q$  and  $R$  are the generalized elastic constants.  $N$  is the shear modulus of the composite. The elastic energy is often damped out due to the viscous exchange between the fluid and structure. The consideration of the coupling is critical in determining the viscous losses. The mass coupling parameter  $\rho_{12}$  describes the interactions between the solid and fluid

media which is defined as,

$$\rho_{12} = -\phi\rho_f(\alpha_\infty - 1), \quad (4.9)$$

where  $\phi$  is the *porosity*,  $\rho_f$  is the *fluid density*, and  $\alpha_\infty$  is the *tortuosity* of the pores. Prior work developed by Johnson et al. (Johnson et al., 1987) details the effect of viscous loss by introducing the *dynamic tortuosity*. It describes the extent of the fluid and solid interaction which is termed the *viscous skin depth thickness*. It can be expressed mathematically as follows,

$$\delta = (2\eta/\omega\rho_0)^{1/2}. \quad (4.10)$$

Since the level of interaction is frequency dependent, the formulations for the high and low scenarios are created. At high frequency, the viscous skin thickness appears to be thin so the interaction between the two media concentrates near the interface. Conversely for low frequency range, the energy exchange tends to penetrate further into the interface ( $\delta/r \gg 1$ ), resulting in more significant viscous damping. Using 50 kHz narrow band transmission, this study concludes that a low-frequency range is suitable for the poroelastic analysis. Henceforth, the corresponding approximated dynamic tortuosity under the low-frequency limit according to (Biot, 1956) and (Fellah et al., 2018) is defined as,

$$\alpha(\omega) \approx \alpha_0 \left( 1 + \frac{\eta\phi}{j\omega\alpha_0\rho_fk_0} \right) \quad (4.11)$$

where  $\alpha_0$  is the approximated tortuosity under the low-frequency approximation introduced by (Lafarge et al., 1997). In the next section, numerical simulation of the Biot's model with dynamic tortuosity will be analyzed in the frequency domain.

	Values
Porosity	0.4
Drained Density	685.71 kg/m <sup>3</sup>
Permeability	0.1 m <sup>2</sup>
Tortuosity Factor	1.7

Table 4.4: Parameters describing the poroelastic medium

### 4.2.1 Case Study: Unsaturated vs. Saturated Porous Matrices

The microscopic hollow fibers called *tracheids* oriented lengthwise are responsible for transporting water and nutrients in order to sustain the growth. This function remains intact even when a tree is commissioned for service as a utility pole. Once a brand-new pole is planted to the ground, the ground with high moisture content allows the tracheids to continue transporting water up to a few feet above the groundline. Contrarily, the tracheids can be unsaturated when the ground moisture level is relatively low. Since the coupled constitutive equations (4.8) rely on the fluid properties, the medium in the tracheids can significantly alter the propagational characteristics. The understanding of the moisture effect on elastic wave propagation in wooden utility poles has yet to be fully understood. Using the prior studies characterizing the porous medium by (Cown, 1975), (Comstock, 1965) and (Matyka et al., 2008) which are detailed in Table 4.4, this section analyzes the frequency domain response of the moisture effect in a porous medium.

The result is illustrated in Fig. 4.10. The frequency axis is normalized with the resonant at  $f = 0$ . The spectral response with respect to the saturated and the unsaturated scenarios are plotted. In the unsaturated case, the force interaction between the media is virtually zero, greatly depleting the damping effect. In the saturated case, the damping force becomes more pronounced causing greater attenuation in the signal away from the resonant frequency. Using power regression  $A = A_0 f^n$ , the coefficients are depicted in Table 4.5. It shows the exponent  $n$  of -1.069. Compared to the dynamic tortuosity, the exponent of



	Unsaturated (Air)	Saturated (Water)
$A_0$	4803.6	600.59
$n$	-1.069	-1.061

Table 4.5: Estimated parameters of an attenuation regression model between the unsaturated and moisture saturated medium

the frequency is -1. This result helps validate the numerical model. For the saturated and unsaturated media, there is a significant difference in amplitude. The regression model

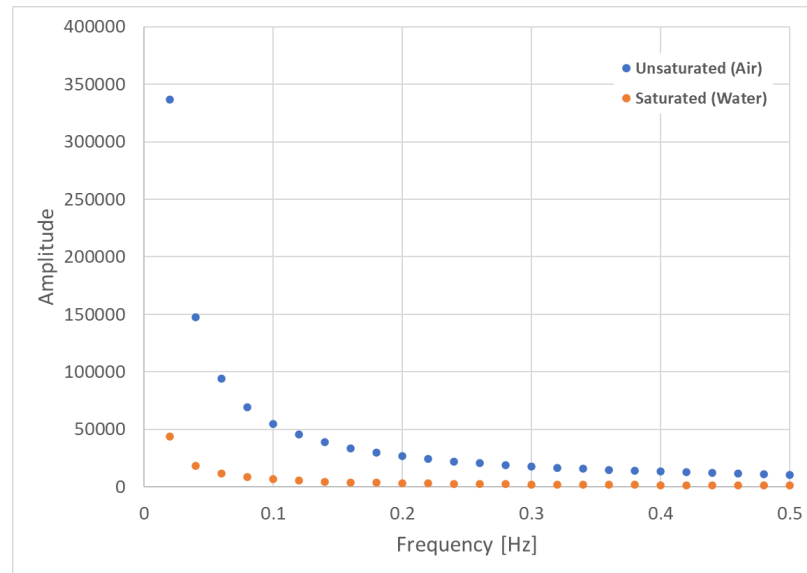


Figure 4.10: A comparison of the energy attenuation rates between the unsaturated and moisture saturated medium

suggests that the amplitude decreases as  $f^{-1}$  in both cases. By examining the constant  $A_0$ , the saturated model clearly presents a greater frequency-dependent attenuation caused by the fluid medium.

#### 4.2.2 Case Study: Variations in Porosity

As discussed in Chapter 2.1.2, the *Coriolus versicolor* decay fungus can attack both lignin and cellulose due to their high concentrations of carbohydrates in the more advanced stages. A scanning electron microscope produced by (Blanchette et al., 2004) in Fig. 4.11

illustrates the result of a more extensive white-rot decay. The resulting destruction of the cellulose causes an increase in porosity. A semi-empirical attempt was made by (Shang-guan et al., 2014) using nitrogen adsorption to quantify the increase of porosity as a result of prolonged exposure to the decay agents. This direct degradation of biomaterial within the wood cells destroy the transport functions of cellulose, significantly altering the desired physical and mechanical properties of the wood.

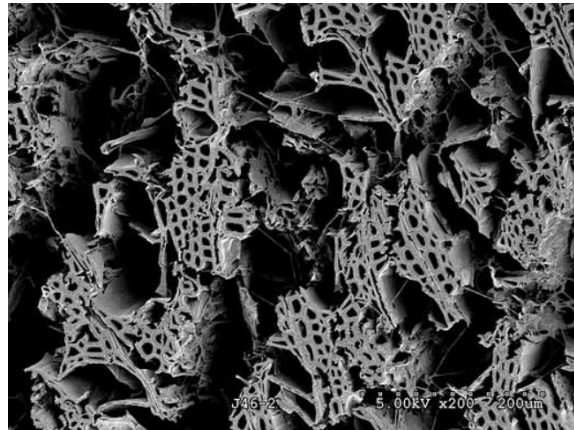


Figure 4.11: A scanning electron micrograph of wood that has been decayed by white rot (Blanchette et al., 2004).

This section analyzes the sensitivity of poroelastic wave to the variation in porosity. Employing the poroelastic model described in this section, five different porosities are investigated:  $\phi = 0.4$  to  $0.8$ . The result of the wave amplitude is plotted in the spectral domain shown in Fig. 4.12. Using the power regression model, the exponent and the coefficient constants are listed in Table 4.6. The result suggests a directly proportional correlation between the increase in porosity values and the spectral amplitude. While the exponent of the frequency remains at  $n = -1$  in all the cases, the decrease in  $\alpha_0$  suggests greater viscous damping or attenuation in the elastic energy propagation.

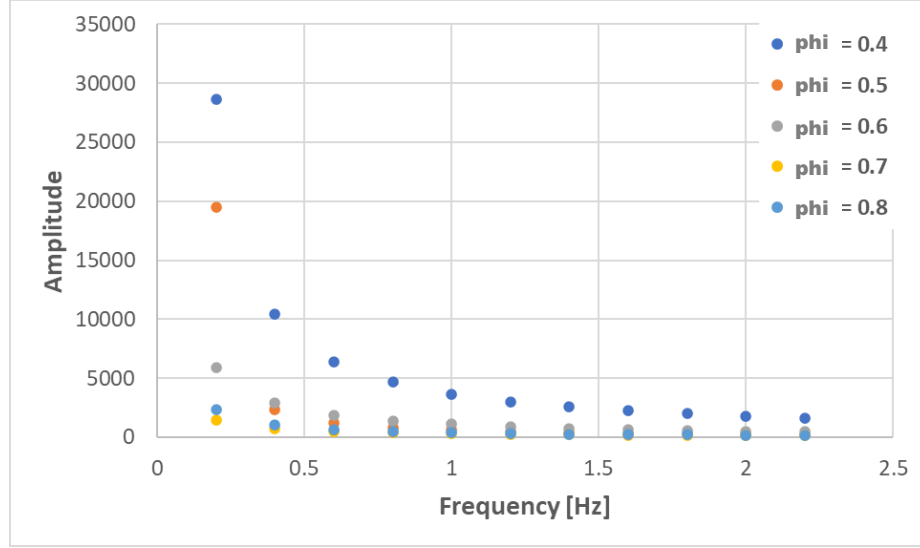


Figure 4.12: Spectral response of the received signal under different porosity

$\phi$	0.4	0.5	0.6	0.7	0.8
$\alpha_0$	3978.7	795.6	1083.2	297.1	407.5
n	-1.0	-1.0	-1.1	-1.1	-1.0
$R^2$	1.0	1.0	1.0	1.0	1.0

Table 4.6: Parameter estimation of power regression of different porosity values

### 4.3 Summary and Discussion

Based on a classical description of the orthotropic medium, a numerical model about the EOM elastic wave with cylindrical symmetry is introduced. The numerical results suggest the possibility of detecting Rayleigh mode in the temporal domain. The uncovered characteristics in relation to the Poisson's ratio discussed in Chapter 3 help explain the orthotropic wave propagation. Based on the decay mechanisms, the effects of different mechanical properties in the time domain were analyzed and derived important wave characteristics. An investigation into the poroelastic characteristics was conducted. Employing the Biot's poroelastic formulation, the dynamic tortuosity term relates the viscous damping to several vital characteristics describing the medium. The case studies corresponding to realistic scenarios are examined. The microscopic incipient decay corresponds to an increase

in porosity and saturation due to the surrounding environmental conditions or preservative treatment. The numerical model in both cases suggests greater viscous damping in the frequency domain representation. This chapter developed a comprehensive two-dimensional propagational model. For GLGL region assessment, the argument of developing a three-dimensional model could offer a numerical insight with two practical implications. Firstly, the possibility of out-of-plane relative placement of the probes could impact the obtained ultrasonic waveforms. However, the isotropic emission of the waveguide and the field attempt to align both probes in the same GLGL plane minimize the impact of off-plane elastic emission and reception. Secondly, the elastic wave can propagate or guided along the pole due to the half-space boundaries at the tip and the butt of the structure. This is the so-called guided wave phenomenon. This process requires exponentially stronger energy excitation and high sensitivity reception due to the strong energy attenuation of elastic wave propagation and the leakage of elastic energy between the pole and the nearby soil. Hence, its effect on the in-plane elastic propagation is minimal. The next chapter focuses on the dedicated signal processing technique allowing both time and frequency domains to be analyzed simultaneously to help infer the physical condition of the shell region at the groundline.

# Chapter 5

## Holistic Signal Synthesis

Based on the analytical and numerical models, the simulated elastic waveform at the receiving waveguide contains both temporal and frequency information essential to infer critical physical conditions within the shell region. As a logical extension, time-frequency domain analysis is deployed to expose the information hidden in the waveforms. Similar to other research in quantitative NDE, time-frequency representation has proven to be a successful tool to uncover critical content about the material condition (Chen and Guey, 1992) and (Flandrin, 1988). This chapter develops an signal synthesis technique by exploiting the TF-domain representation in order to establish an algorithmic foundation for empirical examination in Chapter 6.

### 5.1 TF Domain Representation

The TF representation in acoustic problems has been used to analyze acoustic waveform containing scattering and wave mode interference (Choi and Williams, 1989). A comparative study conducted by (Dragonette et al., 1996) shows the temporal and spectral resolution and localization of the *short-time Fourier transform* (STFT) and wavelet trans-

formations in solving backscattering acoustic problems. Similar to the previous studies, this section briefly introduces the STFT and the continuous wavelet transformation. Using the same signal generated from the model as the case studies, the performance of these two techniques will be analyzed and compared.

### 5.1.1 Short-time Fourier Transform

The STFT was first proposed as a generalization of the Gabor wavelet transform (Gabor, 1946). Further developments have continued, refining the implementation. Consequently, it has been used in many different applications (Boashash, 2015). The basic mechanism is to begin with the construction of the time-domain window of a length  $m$ . Within each window, the Fourier transform is performed. The window “hops over” the signal with a size  $h$ . This process continues until all the data points have been captured in the process. A windowing technique performed on deterministic time-invariant signal is expressed below,

$$x_l[m] = x[m + lH]w[m] \quad (5.1)$$

where  $m$  is the local time index and  $m \in 1, 2, \dots, M$  where  $M$  is the total number of signal fragments.  $l$  is the frame index,  $H$  is the hop size, which is a time advancement in sample as the window generates various windows.  $w$  is the window function. Typical window functions include Hamming, Blackman and Hann. Fig. 5.1 illustrate the a series of overlapping windows operating on the time-series signal. After the signal is broken down into various segments, discrete Fourier transform (DFT) is operated in every frame. That is,

$$X[k, l] = \frac{1}{M} \sum_{m=1}^K x_l[m] e^{-j2\pi mk/K} \quad (5.2)$$

where  $k \in 1, 2, \dots, K$  where  $K$  denotes the total number of frequency bins. A good illustration of the algorithm is provided in Fig. 5.2. The signal is dissected into small window ( $win$ ), and the window hops according to the hop size. The process continues to yield different window segments.

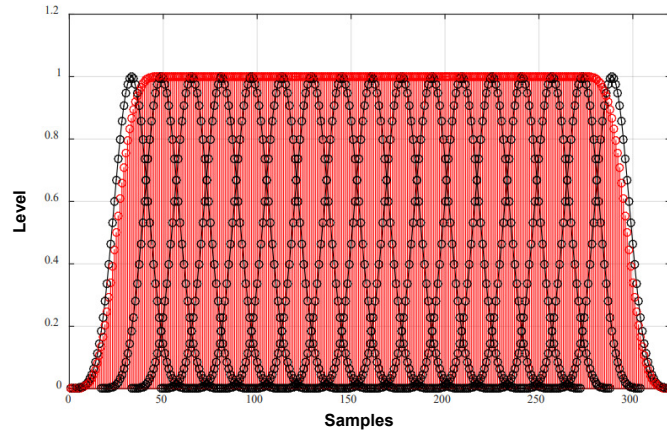


Figure 5.1: An overlapped Blackman window.(Zhivomirov et al., 2019)

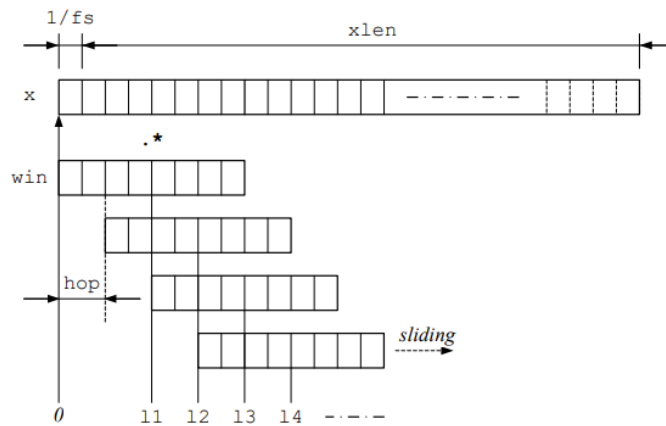


Figure 5.2: Illustration of process work flow of the STFT. (Zhivomirov et al., 2019)

The STFT uses constant temporal and spectral resolution for the entire analysis domain. Fig. 5.3 portrays a simple time-frequency resolution scheme. The constant division between the horizontal and vertical axes signifies the constant temporal and spectral resolution. This scheme presents an undesirable result in many applications. In addition, it

suffers the uncertainty according to (Auger et al., 2013). As illustrated in Fig. 5.2, the segmented window size can be varied, yet large window size loses the temporal resolution, but increase the spectral resolution. In contrast, the small window size improves the temporal resolution while decreasing the spectral resolution. In the ultrasonic application presented in this study, narrow-band of 50 kHz with a sampling rate of around 3.3 MHz is used. Since the 50 kHz response resides in the low end of the spectral range, and the high spectral information is not required, the STFT can produce low resolution in the low-frequency range. Hence, a multi-resolution scheme using continuous wavelet analysis will be investigated.

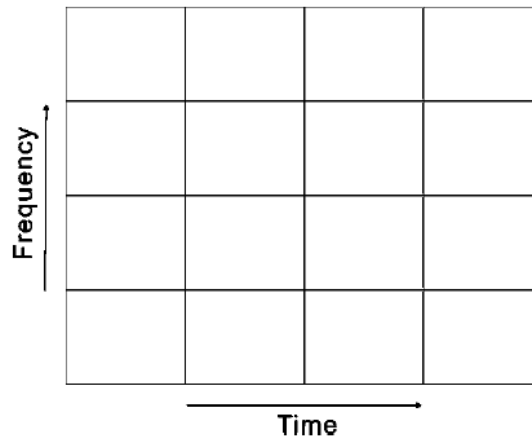


Figure 5.3: An example of the STFT resolution scheme.

### 5.1.2 Continuous Gabor Wavelet Transformation

Unlike the STFT which has a constant temporal and spectral resolution, wavelet transformation is a *multiresolution* transformation in the frequency domain, the increment of frequency in the time-frequency plane depends on the chosen filter bank. By definition,



Wavelet transformaiton is an inner product defined as (Mallat, 1999),

$$W_{\psi}^y(a, b) = \frac{1}{\sqrt{c_{\psi}|a|}} \int_{-\infty}^{\infty} y(t) \psi \left( \frac{t-b}{a} \right) dt, \quad (5.3)$$

where  $a$  is the dilation parameter and  $b$  is the translation parameter.  $y(t)$  is the stationary time signal.  $\psi$  is an operator function defined as the *mother wavelet*. The mother wavelet takes on different forms depending upon the selection. To select a proper mother wavelet, prior work by (Newland, 1999) indicates that signal containing dynamic frequency and time components should use *analytic wavelet function* (AWT) to analyze the signal. By definition, an analytic wavelet function must satisfy the following condition:

$$\left\{ \begin{array}{l} \int_{-\infty}^{\infty} \psi(x) dx = 0, \\ \|\psi(x)\|_2 = 1, \\ \psi(x) \text{ is symmetric about } x = 0. \end{array} \right. \quad (5.4)$$

Non-analytic mother wavelet often leads to interference and artifacts that can erroneously represent the amplitude and phase. Analytic mother wavelets such as the Gabor, analytic form of the Mexican hat, and Cauchy are considered. The most proper wavelet tends to have a matched shape as the signal in question (Ngu et al., 2013). Among the examined wavelets, the Gabor wavelet exhibits a temporal response similar to the transient waveform estimation by the dual waveguide configuration. Henceforth, the Gabor wavelet will be employed for the remainder of the analysis. Gabor wavelet is given by,

$$\psi(t) = e^{\beta(t^2/2)} e^{j\omega_0 t}, \quad (5.5)$$

where  $\omega_0$  is defined in a particular application to ensure the admissibility condition holds (Louis et al., 1994). The time-frequency plan is shown in Fig.5.4. In the low-frequency region, the plan portrays an acceptable frequency resolution for better spectral analyses and detection of the spectral response. Based on the findings from analytical and numerical models, the Gabor CWT produces a desirable temporal and spectral representation of the signal to detect the mechanical and the poroelastic variations in the propagating medium. This transformation does suffer temporal resolution in that range, but it is a common drawback in any TF domain analysis according to the uncertainty principle (Kim and Kim, 2001).

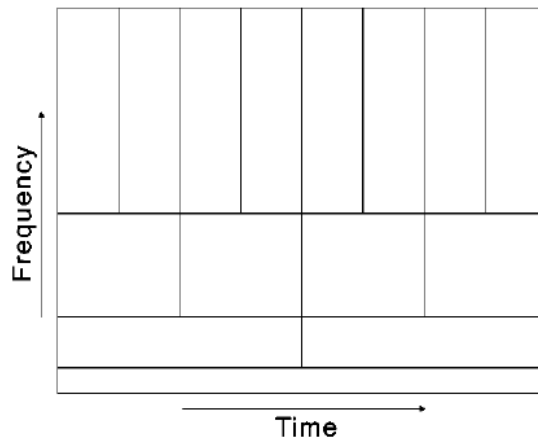


Figure 5.4: An example of the Wavelet resolution scheme.

## 5.2 Model-based Signal Analysis

The studies concluded in Chapter 3 and Chapter 4 suggest that the TF domain representation of the signal is essential to explore the physical conditions of the medium. The diffusive property that induced by the difference in phase speed between the fast and slow modes inhibits in the temporal domain. The TOF of the peak energy evidences severity of the incipient decay. The moisture content and variations in porosity associated with

the porous medium exhibit unique damping characteristics, which can be exploited in the frequency domain. Hence, this section attempts to deploy the appropriate time-frequency domain analysis to assess the GL condition.

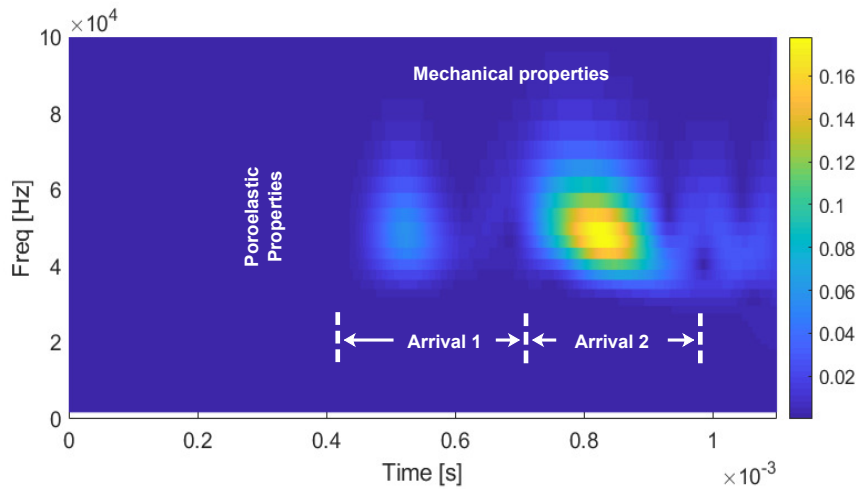


Figure 5.5: Relating physical properties to the TF domain analysis.

Using a simulated signal discussed in Chapter 4, the corresponding TF domain representation is displayed in Fig.5.5. Two pronounced clusters of energy are detected. These two clusters correspond to the AW2 and AW3 illustrated in Fig. 4.6 in Chapter 4. In AW3, the peak response at 50 kHz shows the fundamental frequency of the simulated signal. Due to the nature of the waveform responses in different domains, the frequency domain analysis helps infer the conditions about poroelastic medium and the time domain helps analyze the diffusivity and phase velocities of the medium based on the changes in the mechanical properties.

### 5.3 Case Study: Cylindrical Medium Without Attenuation

The STFT and Gabor wavelet transforms are used to analyze the temporal and spectral resolutions of the received waveforms. By neglecting the poroelastic effect, two received stress waveforms are generated by setting the Poisson's ratio to  $\nu = 0.2$  and  $\nu = 0.4$  (shown in Fig. 5.6). The corresponding STFT and the Gabor Wavelet transforms are illustrated in Fig. 5.7. The STFT displays two enhancement of energy located between 400 and 600  $\mu\text{s}$  and 700 to 1000  $\mu\text{s}$ . These two clusters are AW2 and AW3 based on the previous time-domain analysis. For the circumferential Rayleigh mode (arrival number 3) in the STFT domain, there is a subtle enhancement of energy (circled in white). The range of the spectral domain remains relatively the same. in both cases. The pixelated spectral response indicates a poor spectral. In the Gabor wavelet domain (subplot c and d), high spectral resolution produces a slight enhancement in the AW1 region (see subplot d). It enhances the AW2 and AW3 energy response by giving a more detailed feature in both the spectral region and the temporal region. It produces much higher sensitive frequency response up to 100 kHz than the STFT. For the diffusivity of AW3, the temporal domain produces greater diffusion in the  $\nu = 0.4$  case by enhancing the circled region with  $t \approx 900 \mu\text{s}$ .

At  $f = 50 \text{ kHz}$ , the enhanced temporal energy response at 50 kHz is shown in Fig. 5.8. Both domains detect the difference in energy corresponding to the diffusive interference occurring at  $t \approx 0.9 \text{ ms}$ . The temporal domain appears to be correct. The amplitude of the energy response is different. The Gabor generates a greater difference of 0.03 in the peak energy compared to the STFT which shows a difference of 0.02. The difference of the diffusive effect after the peak energy is enhanced in the Gabor wavelet domain compared to the STFT domain. This result indicates a 30% enhancement in the signal response. The variation of Poisson's ratio in the Gabor wavelet transform appears to be more pronounced

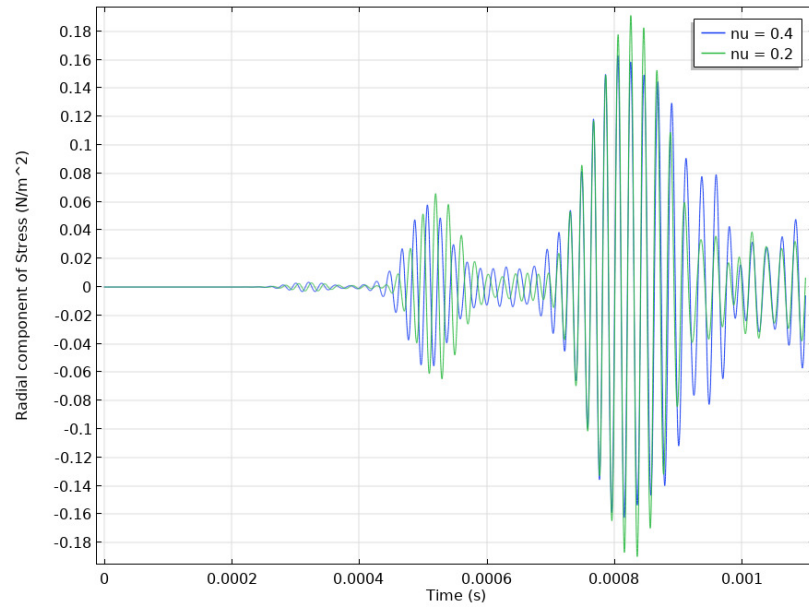


Figure 5.6: Temporal response.

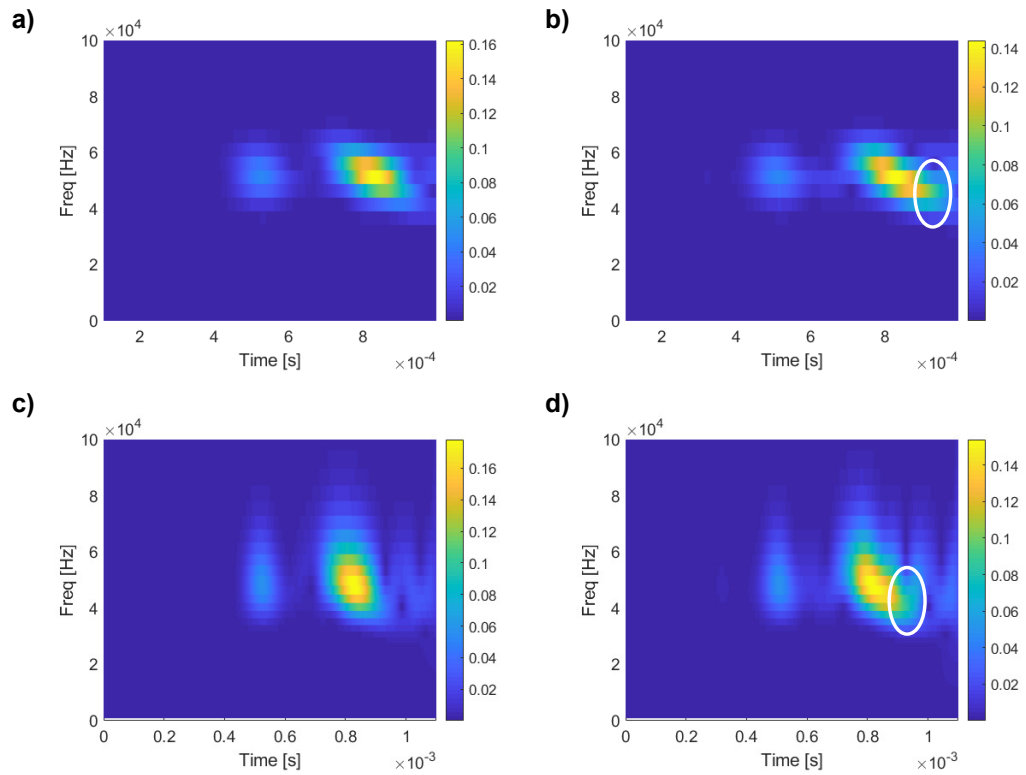


Figure 5.7: STFT vs. Gabor Wavelet, a) STFT with  $\nu = 0.2$ , b) STFT with  $\nu = 0.4$ , c) Gabor wavelet with  $\nu = 0.2$  and d) Gabor wavelet with  $\nu = 0.4$

than the STFT. This suggests a better sensitivity and resolution.

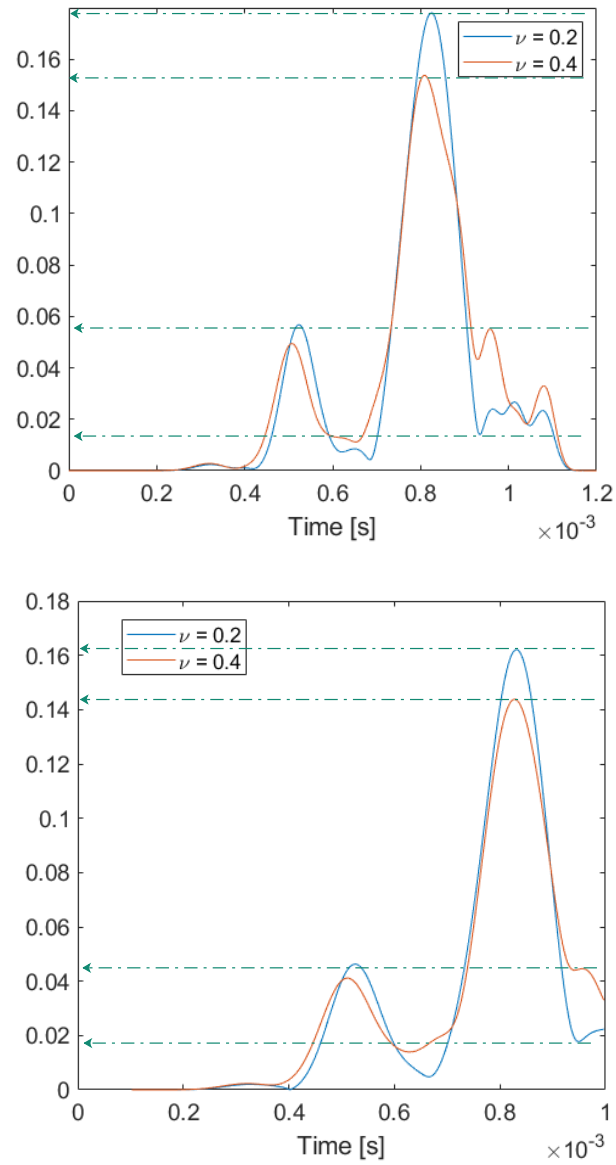


Figure 5.8: Time domain responses at the resonance at 50 kHz using the a) Gabor CWT and b) STFT

## 5.4 Case Study: Cylindrical Medium with Viscous Damping

The dynamic tortuosity of the Biot's formulation incurs energy attenuation by imposing a non-zero value in the 1st order differential term. This section aims to investigate the detectability and sensitivity of the attenuated energy in both the STFT and the Gabor wavelet domains. A simplified mathematical expression is shown below,

$$\rho \frac{\partial^2 \mathbf{u}}{\partial t^2} + \alpha_{dw} \rho \frac{\partial \mathbf{u}}{\partial t} - \nabla \cdot \sigma = Fv, \quad (5.6)$$

where  $\mathbf{u}$  is the displacement field,  $\rho$  is the effective density, and  $Fv$  is the forcing term that represents the introduced elastic disturbance.  $\alpha_{dw}$  is defined as the viscous damping. When  $\alpha_{dw} = 0$ , it is an undamped case, and  $\alpha_{dw} > 0$  represents the damped case. In this study, the orthotropic medium is used with the 0-180 testing configuration. The results of the damped and undamped cases are shown in Fig. 5.9. Distinct attenuation in the signal is observed in

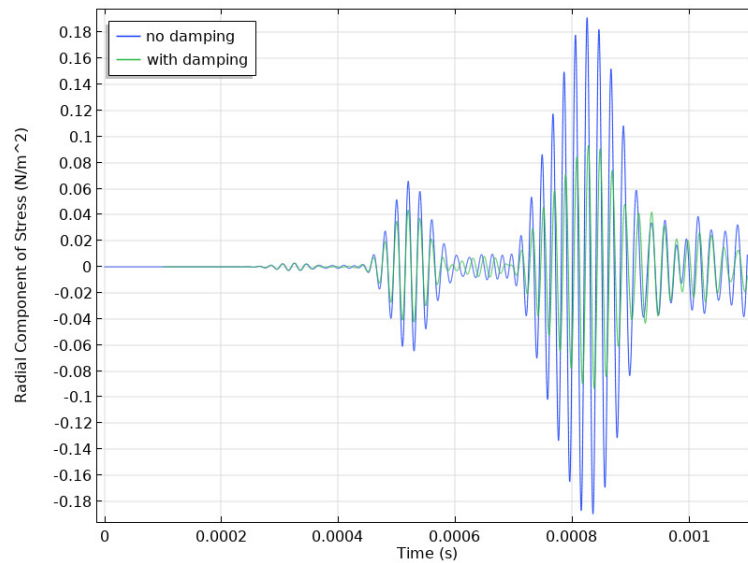


Figure 5.9: Waveform with an imposed viscous damping

the damped case, while the temporal locations of the envelopes are comparatively the same. They do appear to have some distinct differences in terms of the attenuation levels. At  $t \approx 500 \mu\text{s}$  which corresponds to the AW2, the amplitude level is reduced by 33%. Compared to AW3 at  $t \approx 800 \mu\text{s}$ , the amplitude is roughly reduced by almost 50%. Since the viscous damping is frequency dependent, the difference in levels of attenuation suggests that the AW2 and AW3 might have different frequency components. The scalogram of the TF-domain representation is shown in Fig. 5.10. It is apparent that Gabor CWT produces more refined features due to its higher temporal and spectral resolution. By exacting the

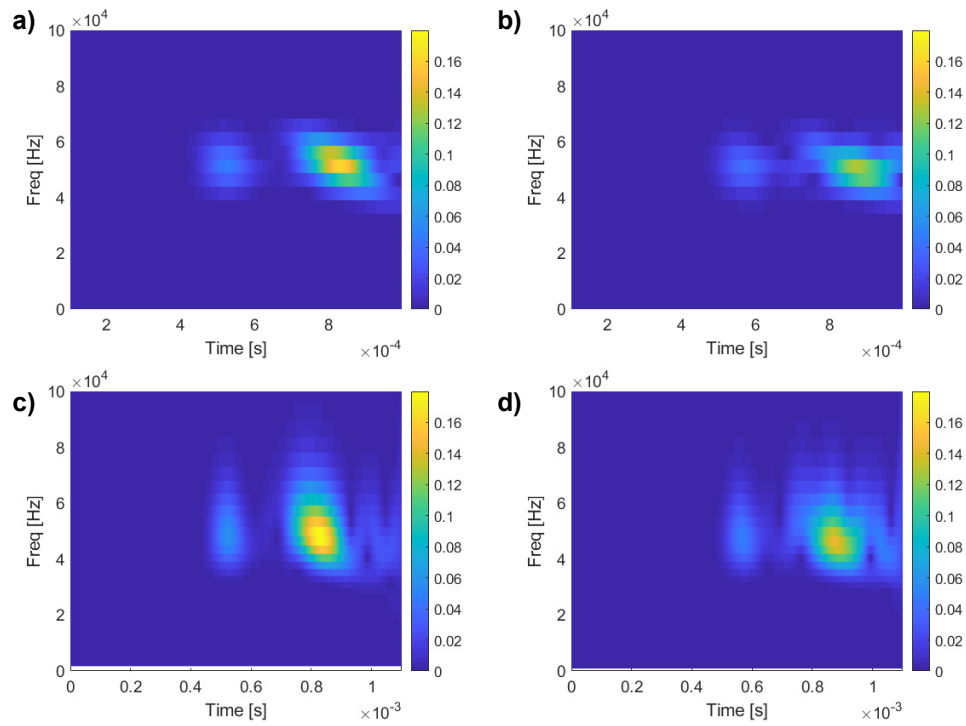


Figure 5.10: Waveform with an imposed viscous damping

temporal energy response at the resonance, the result is depicted in Fig. 5.11. The energy peaks shown in Gabor CWT suggests a reduction of 51%, compared to the STFT of 46%. It indicates that the Gabor CWT has a slightly more sensitive energy response. The times of the occurrence of peak energy are relatively the same in both cases. By examining the width



of the peaks in all arrivals, Gabor CWT has a slightly localized response compared to the STFT, which is an important feature to prevent interference between the energy peaks that inadvertently gives erroneous measurements of the wave characteristics. The comparative result suggests the Gabor CWT has a slightly better performance over the STFT. The next section employs the Gabor CWT and the analysis process presented to produce a waveform analysis algorithm to help characterize the GL region.

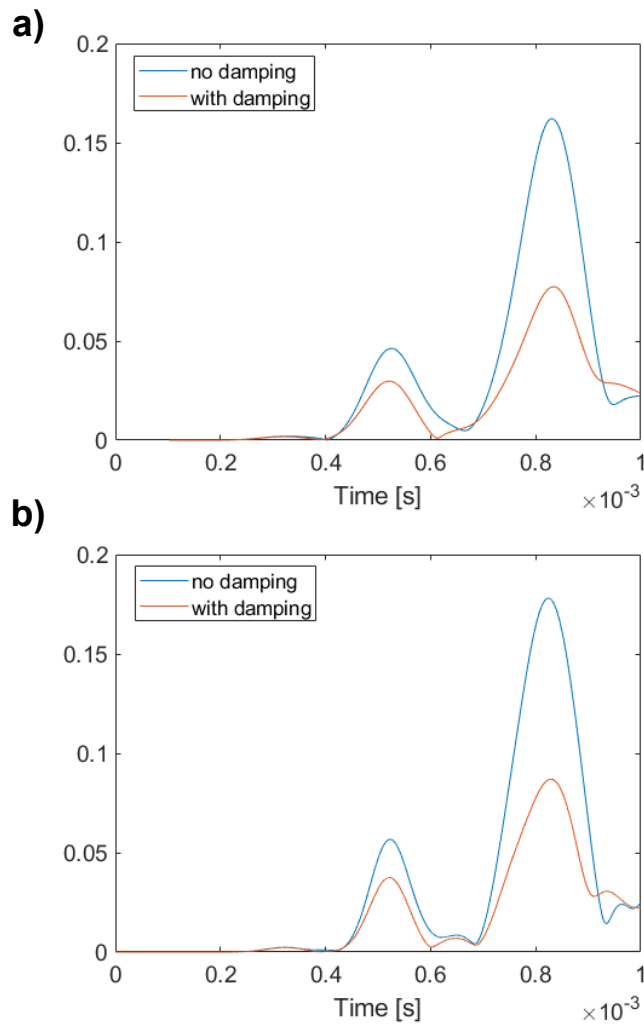


Figure 5.11: Time domain energy response at 50 kHz, with imposed viscous damping to simulate energy attenuation using a) STFT transformation and b) Gabor CWT transformation

## 5.5 Proposed Algorithm

The proposed algorithm follows the flow in Fig. 5.12. The raw data obtained at the GL region from the UB1000 is inserted into the algorithm. The signal-to-noise ratio (SNR) is calculated to evaluate the signal integrity. This calculation is critical to ensure the received signal contains a strong energy response. If the SNR is not high enough, the algorithm exits due to possible weak reception of the ultrasonic signal. Otherwise, the CWT using the Gabor mother wavelet is employed to transform the raw data into TF-domain representation. Under this representation, the resonant frequency is determined based on the strongest energy response in the frequency domain. At the resonant frequency, a one-dimensional temporal response can be extracted. The detection of the AW3 relies on the determination of the expected arrival region (EAR). This region can be based on the past datasets of the pole with similar dimensions and geographical locations. This range takes the dimensional, signal, the species of the wooden medium, and mechanical degradation into account to ensure AW3 can be detected in most cases. Within each region, the peak energy search subroutine is employed to determine the relevant peak based on a set of characteristics. Once the peak is identified, the algorithm calculates the peak energy value, the full width half maximum (FWHM) and time.

## 5.6 Summary and Discussion

Based on the implications of temporal and spectral domains in medium characterization discussed in Chapter 3 and 4, this section details a proposed signal analysis technique capable of dissecting the signal into the time and spectral domain holistically. Previously developed transformation such as the STFT and the wavelet transformation via Gabor mother wavelet are compared using a numerical model with and without the influence of viscous

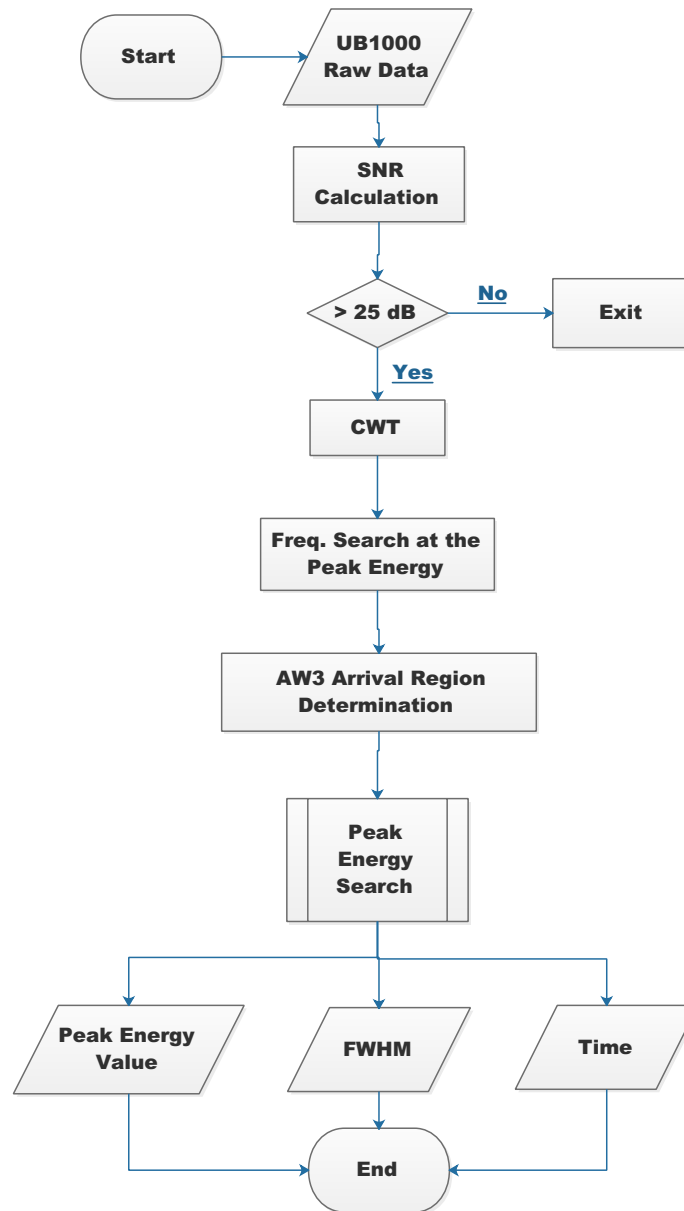


Figure 5.12: Flow chart of the algorithm

damping. The mother wavelet demonstrates more promising results in terms of sharper temporal localization of the peak energy, better spectral resolution, and contrast of the energy response when damping is imposed. Henceforth, the comparative study results in the selection of using Gabor continuous wavelet transformation as the signal analysis technique. Thus, an algorithm is developed with a flow chart detailing the implementation pro-

cess. The proposed algorithm will be tested in the next chapter using realistic samples and the results will be compared against the industry standard to evaluate the effectiveness.

## Chapter 6

# Empirical Study of Proposed Techniques

At this point, the fundamental understanding of principles governing the embedded waveguide excitation has been established. The numerical and theoretical findings have explained the essential relations between waveform parameters and the physical condition of the medium. It enables the condition assessment by dissecting different waveform characteristics. Through the time-frequency (TF) domain analysis, those parameters can be extracted to evaluate the cross-sectional condition of the wooden utility pole. Among different TF domain analysis techniques, the continuous wavelet transform using the Gabor mother wavelet appears to fulfill the analysis requirement with more superior performance. This chapter presents the empirical results. The ultrasonic instrument was developed through academic and industrial partnerships. This chapter utilizes empirical results to further validate the analytical and numerical findings. This chapter begins by briefly introducing the UB1000 design, including both the electrical and mechanical components. The empirical ultrasonic signal obtained from a sound wood pole will be examined in both the temporal and spectral domains. Based on the derived analysis technique, the effects of saturated and unsaturated media will be examined and compared in detail. The impact of mechanical degradation on the signal will then be analyzed. From a population of fifteen poles

with known conditions, the selected physical features will be plotted on a feature plot to highlight the possible future work in ultrasonic assessment.

## 6.1 A Brief Description of the UB1000 System

Fig. 6.1 illustrates an exploded view of the UB1000 (Hall et al., 2020) which consists of three primary subassemblies: The casing assembly (5), the electronic assembly (9) and the transducer assembly (7). The casing assembly protects the internal devices from the elements. The electronic assembly manages the transmitting (Tx) and receiving (Rx) of ultrasound through the transducer assembly. Fig. 6.2 shows a functional flow of the UB1000 circuitry. A Bluetooth module is used to establish a connection between the UB1000 probe and a tablet running the Android operating system. When an Rx commanding signal is issued by a user through the tablet, the received ultrasonic is filtered and amplified before sending it to an onboard analog-to-digital converter (ADC). The digitized raw data is forwarded to an onboard Bluetooth module to transmit the raw data to an Android OS tablet to perform post-processing analyses. Once the Android tablet initiates transmission command, the energy initially stored in the capacitor is discharged to provide a high-voltage DC source. Based on the concept introduced in Chapter 2.2, the energy is routed to a full-bridge converting a DC power into an 80-volt peak-to-peak modulated square wave to drive the ultrasonic transducer.

The physical layout of the system is illustrated in Fig. 6.3. Fig. 6.3a is a screen shot of the UB1000 application installed on a tablet to communicate with the UB1000 units shown in Fig. 6.3b. Fig. 6.3c shows a complete configuration of how the UB1000 is mounted to a wooden pole using the embedded waveguide for transverse ultrasound Tx and Rx. Fig. 6.3d shows the embedded waveguide. Its detailed specification and the design process are briefly described in section 6.1.1.

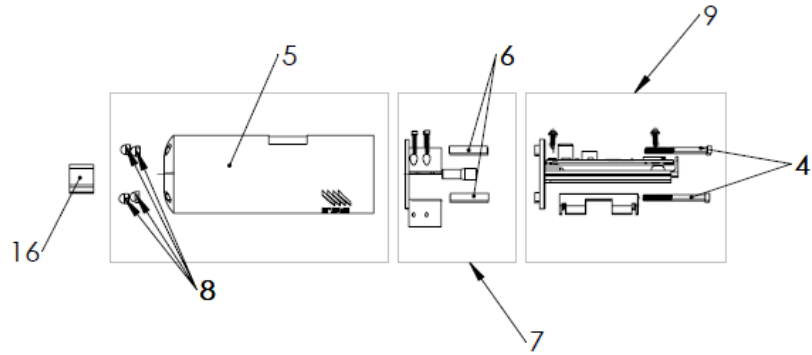


Figure 6.1: Overall internal view of the UB1000 (Hall et al., 2020)

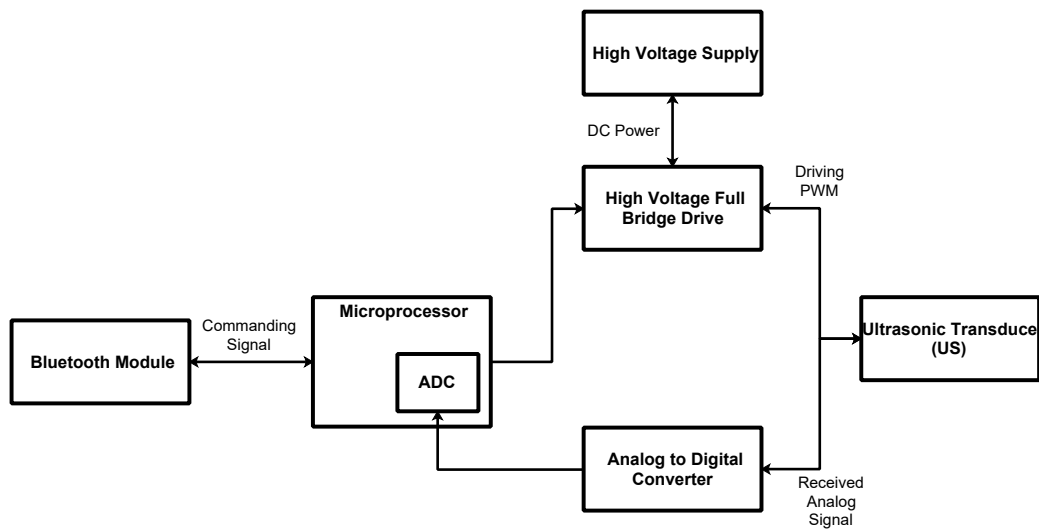


Figure 6.2: Flow diagram of the main circuit.

### 6.1.1 Embedded Waveguide

The waveguide consists of the coupling flange (21), lower body (19), radiating aperture (17), and the depth indicator (15). The depth indicator serves as a visual queue to ensure the waveguide is inserted to a proper depth. The aperture (17) composes of the front and the side aperture. The circular cross-section gradually tapers down to form a cone-shaped tip. The sharp end allows the waveguide to be driven into a specimen using a conventional hammer or a mallet. Once inserted, any stress wave introduced from the flange will be guided

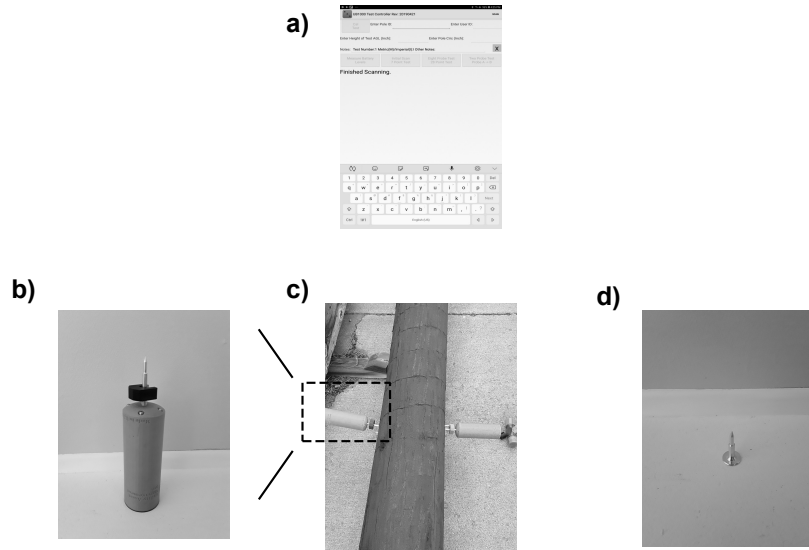


Figure 6.3: The physical layout of the entire UB1000 system

along the shank through the specimen surface. The waveguide radiates ultrasound through the radiating aperture in the interior of the specimen. A Langevin transducer introduced in Chapter 3.4 is used by mating with a designated surface behind the flange to introduce the disturbance. The back flange is also a resonator, by adjusting its diameter, it generates *standing wave* of different frequencies that amplify the energy traveling through the shank. Using FEM optimization process, the waveguide resonates at 50 kHz, the same resonant frequency of the transducer. Fig. 6.5 shows the stress distribution of the waveguide when the external load of 50100 Hz is introduced.

## 6.2 Signal From a Healthy Wooden Utility Pole

A 40-inch in circumference illustrated in Fig. 6.6a is used to demonstrate the received pulse-echo signal. The dimension of the cross-section increases the temporal separation among the arrival wave packets to reduce the unwanted interferences. From the Fig. 6.6a, two UB1000 probes are attached 180° apart at the GL region. The filtered ADC values are



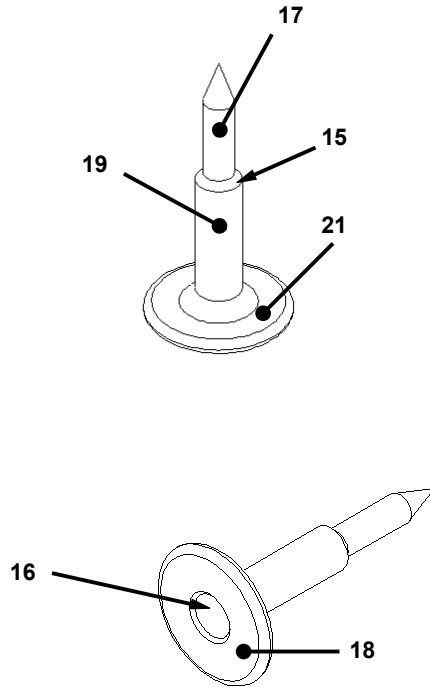


Figure 6.4: Waveguide (Lee and Hall, 2020).

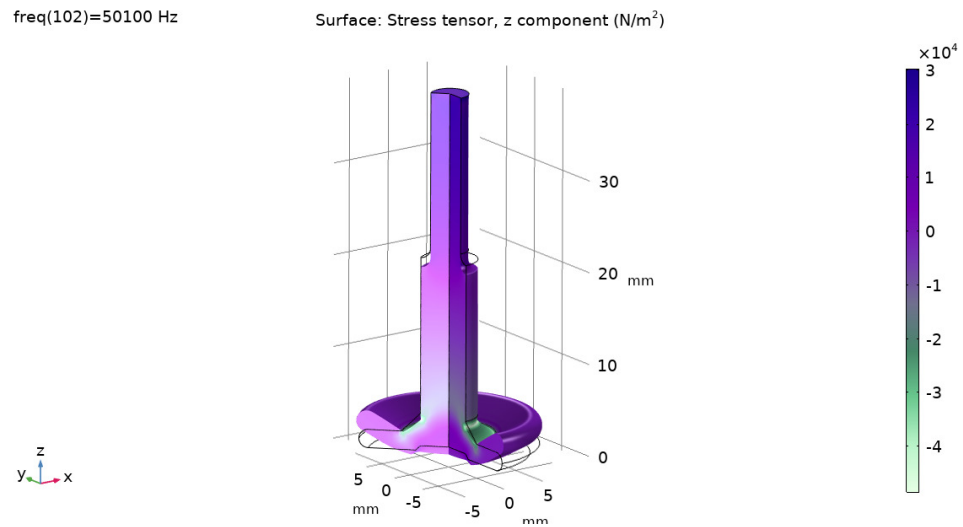
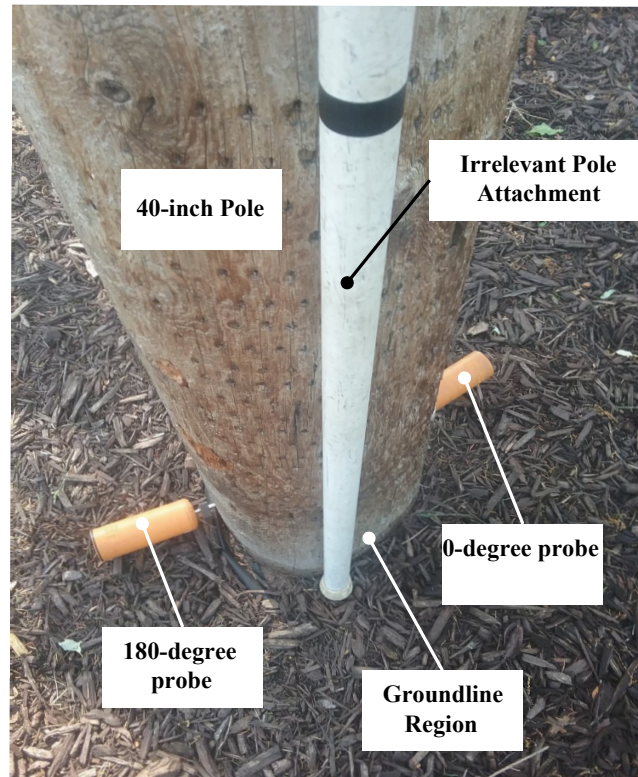


Figure 6.5: Waveguide Spectral Response.

captured in Fig. 6.6b. Preliminary analysis indicates three wavepackets, which can be seen at approximately 300, 500, and 700  $\mu\text{s}$ . Before 300  $\mu\text{s}$ , a low amplitude ambient signal confirms the quiescent environment. A strong SNR between the ambient noise floor and

the received signal indicates the hardware has been implemented successfully despite the high attenuating medium, and the post-processing step can be performed.

a)



b)

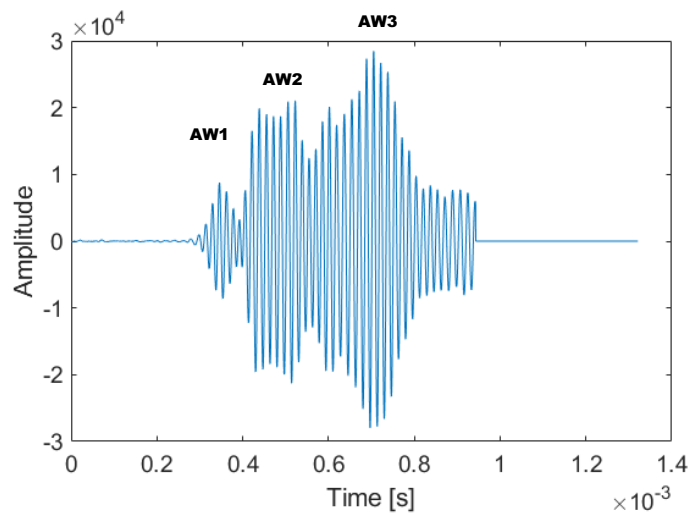


Figure 6.6: An image of the 40-inch circumference pole and the raw signal obtained by the UB1000 system, courtesy of UAM.

The TF Domain analysis is performed based on the Gabor wavelet analysis discussed in Chapter 5. The Gabor domain transformation of both the numerical and empirical results are illustrated in Fig. 6.7. In the T-F domain plot, the two energy clusters are clearly shown corresponding to the AW2 and AW3. Detailed justification can be found in the previous discussion. The empirical result is obtained using the UB1000 system, and we see multiple energy enhancement at  $t = 300, 500, \text{ and } 800 \mu\text{s}$ , which correspond to the arrival waves. To understand the origins of those energy regions, a temporal domain at the resonant frequency of those results are shown in Fig. 6.7 c and d. As discussed previously in Chapter 4, the numerical model gives three different arrival wave packets with increasing peak energy. This is normal when the ultrasonic wave is introduced into a medium of healthy wood cells. A similar pattern of the energy peak appears in the empirical result. However, the relative magnitude of this increase in peak energy is different. This is mainly due to the intrinsic viscous damping caused by irreversible energy dissipation. Based on the previous discussion, this damping factor is a function of distance. Since the AW1 travels radially, it is the shortest distance compared to AW2 and AW3 assuming no internal scattering. Therefore, the attenuation effect is the smallest resulting in a relatively stronger response of AW1 as shown in (d).

Temporal analysis can be used to validate the model by examining AW1 and AW2 TOF ratio. Based on the relative trajectory, the AW1 and AW2 should have a TOF ratio of close to  $\pi/2$ . More precise measurement can be found in Table 6.1. The result of the examination of the peak energy TOF ratio of AW1 and AW2 is shown in Table 4.3. The relative difference between the two is about 6.4%. This difference is due to a synchronization time delay between the initialization of the signal recording and actual transmission of the ultrasound. In addition, the data obtained from the forestry service publication (Green et al., 1999) is an estimate with 10% to 15% variation. This can translate to the difference in the propagating speed. The factor of moisture content, which can affect the mechanical

properties of the cell wall, has not been considered in this study. It is likely to contribute to a difference in the temporal location of the energy clusters. Nevertheless, this finding gives a qualitative comparison of the simulated and the numerical models, and the trajectories of the arrival wave modes.

In the spectral domain, we see a frequency shift of the energy peak. The simulated result illustrates the peak energy, which occurs at approximately 50 kHz, the same frequency response as the imposed resonance load. The empirical result shows a much higher fundamental frequency. Two main factors could contribute to such a frequency shift. Firstly, each transducer is manufactured with some tolerances. The geometric and material variations can slightly alter their vibrational mode producing different resonances. Secondly, the current model has not considered some of the hardware details, including interface coupler and the threaded features at the transducer horn. The fine feature within the transducer may have been intentionally modified the resonant response.

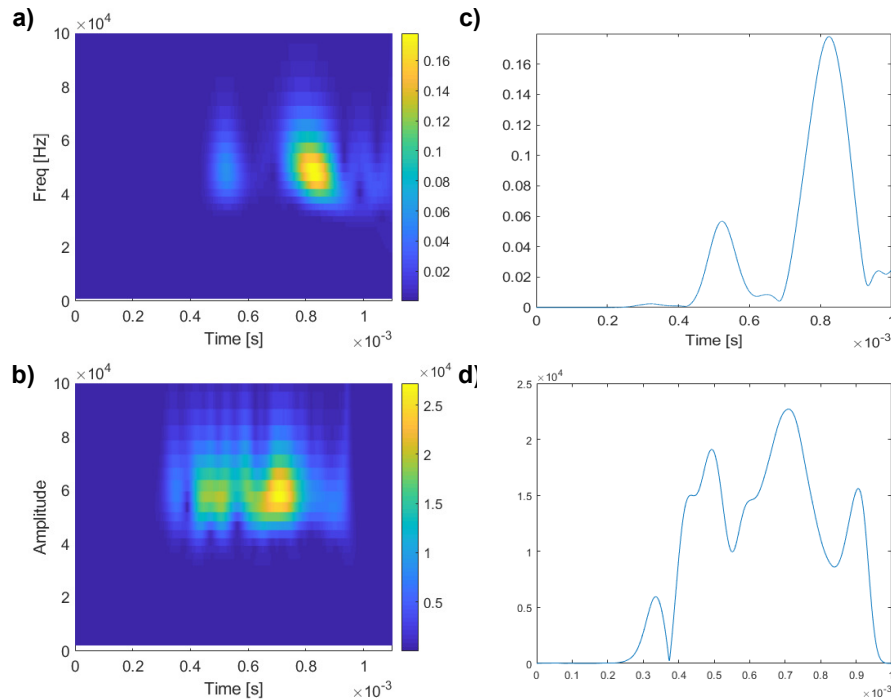


Figure 6.7: The Gabor domain representation of the a) simulated signal and b) GL signal.

	TOF	Energy Peak Value	TOF Ratio (with respect to AW1)
AW1	337	5.95e3	1
AW2	493	1.91e4	1.46
AW3	709	2.27e4	n/a

Table 6.1: Time of flight (TOF) and peak energy information from the empirical signal.

## 6.3 Effects of Saturated and Unsaturated Media

This section focuses on the empirical results in investigating the effects of moisture within the wood fibers on the characteristics of ultrasonic propagation. As previously discussed in Chapter 4.2, high moisture content within the porous matrix without mechanical degradation tends to greatly dissipate stress energy. In this section, we will first introduce the procedures for preparing the specimen, and the obtained signals will be imported into the proposed techniques to extract the critical spectral information. The findings from a comparative study between the high and low moisture content levels will be discussed.

### 6.3.1 Preparation and Procedures

In order to ensure moisture content is the only variable in the experiment, we purchased two nearly identical brand-new and untreated utility poles. The low moisture level within the wood fiber allows the absorption of moisture from the ground to take place naturally. This technique can empirically simulate the transport process to evaluate the effect of moisture saturated wood. An illustration of the experimental setup is displayed in Fig. 6.8. Pole A is exposed to the external humid environment of Georgia for a few months, while the controlled specimen (Pole C) is covered using a tent with only a few feet apart from the other specimen in order to eliminate any solid variation. The tops of both poles are covered so that the absorption of water only occurs at the groundline. In order to eliminate hardware variations, the same set of UB1000 probes are used throughout the entire experiment. Fig.

6.9 depicts the actual setup of the experiment with the two poles (labeled A and B) with two UB1000 units mounted at the GL level. The two datasets from pole A and pole C are collected and analyzed in the next section.

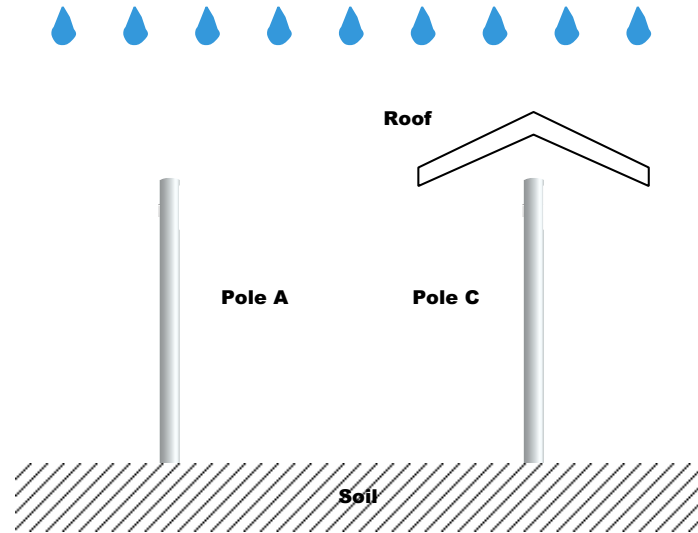


Figure 6.8: Illustration of the experimental setup to examine the moisture effects on the acoustic signal response.

### 6.3.2 T-F Domain Analysis

The received raw ADC values are portrayed in Fig. 6.10. Both plots show an acceptable level SNR suitable for analysis. As noted in Chapter 5, the Gabor wavelet is chosen for the T-F domain analysis. The results are illustrated in Fig. 6.11a and b. Due to the small dimension of both poles, the AW1 and AW2 are merged, creating *composite waveform* that is indistinguishable. Both cases depict a strong energy response at around  $500 \mu\text{s}$ . With the strong energy response at  $f \approx 60 \text{ kHz}$ , we proceed with the temporal analysis at this frequency.

The temporal analysis at the resonant frequency of 60 kHz is illustrated in Fig. 6.12 with both cases imposed on top of each other. Unlike the 40-inch circumference pole, the spatial dimension alters the peak energy TOF of the arrivals. Pronounced attenuation can

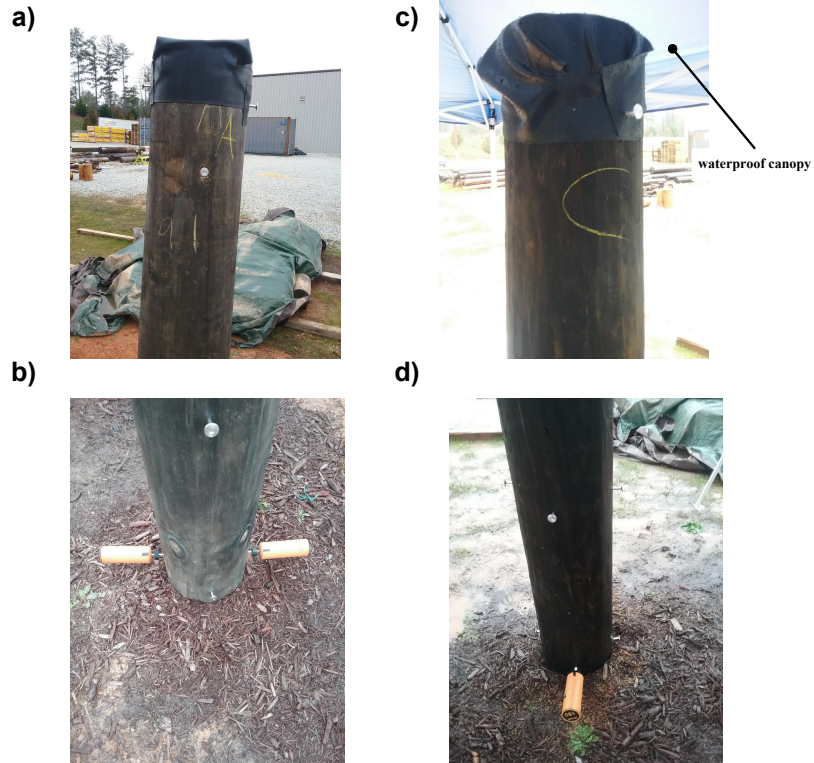


Figure 6.9: Images of the experimental setup a) front view of pole A, b) a view of the GL level of pole A with two UB1000 probes mounted, c) front view of pole C and d) a view of the GL level of pole C with two UB1000 probes mounted.

be observed by comparing results from the two specimens. The dryer specimen (Pole C) shown in red exhibits a strong energy response at around 400 and 500  $\mu\text{s}$ . The response is then quickly depleted after 700  $\mu\text{s}$ . The specimen with higher moisture content (Pole A) shown in blue also exhibits two peaks. Based on the locations, the first peak (AW2) has a drastic attenuation of 20 dB compared to the dryer specimen. We also observe a reduction of 35% for the second peak (AW3). More importantly, the combined peak energy TOF and energy response shown in Table 6.2 has an interesting implication. In the second peak, the energy in Pole A is reduced by 35% while the TOF is relatively unchanged. This can be explained by the finding concluded in Chapter 4. The mechanical property is determined by the temporal domain analysis. Since both poles have the same TOF in AW3, it suggests that the mechanical properties are similar. The attenuation implies a moisture content within

the porous medium. The signal analysis concurs with the experimental setup, validating the findings observed in the numerical and analytical models.

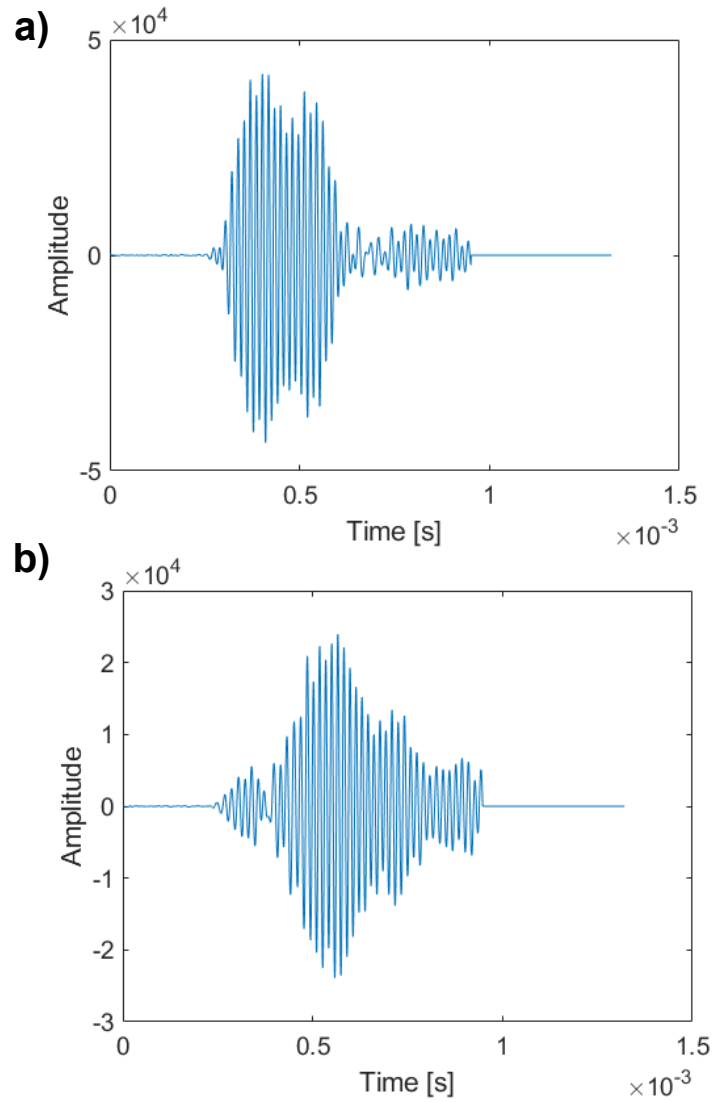


Figure 6.10: ADC filtered values.

## 6.4 Effects of Mechanical Degradation

The mechanical degradation resulted from an incipient decay discussed in Chapter 4 decreases the group speed of the AW3. This section employs the proposed T-F domain



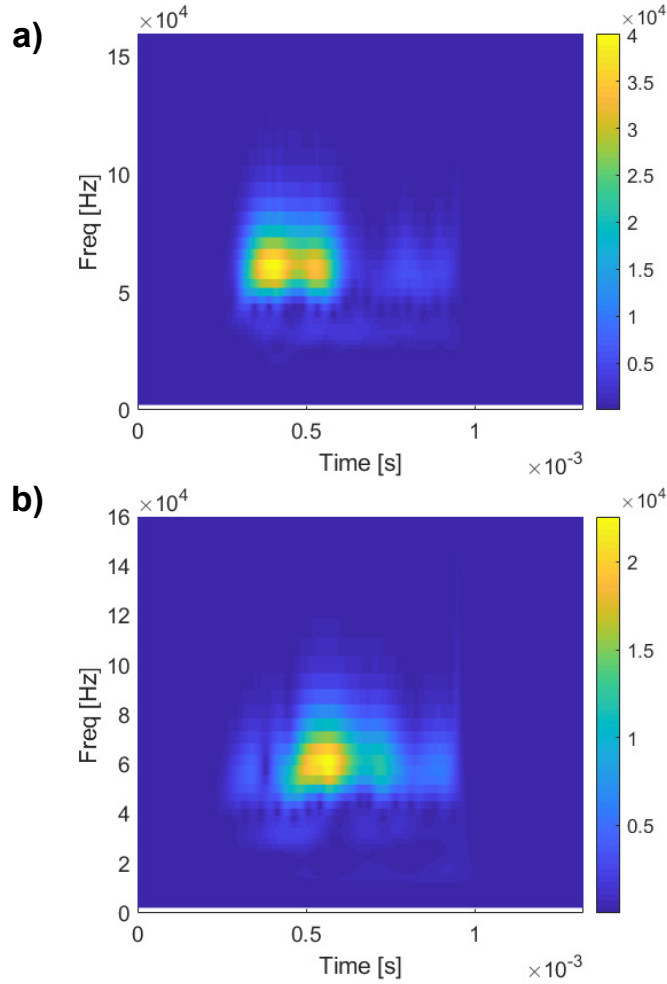


Figure 6.11: Wavelet domain.

	Low M.C.		High M.C.		Comparative Result	
	TOF	Energy Peak	TOF	Energy Peak	Attenuation	TOF Delay
AW2	387	3.9e4	342	4.4e3	89%	12%
AW3	520	3.4e4	530	2.2e4	35 %	2%

Table 6.2: The energy attenuation and the time-of-flight (TOF) between Pole A (low moisture) and Pole C (high moisture).

analysis, the signal collected using the UB1000 system from a deemed healthy and shell rot pole determined by the industrial standard process for wooden pole examination are analyzed and compared.

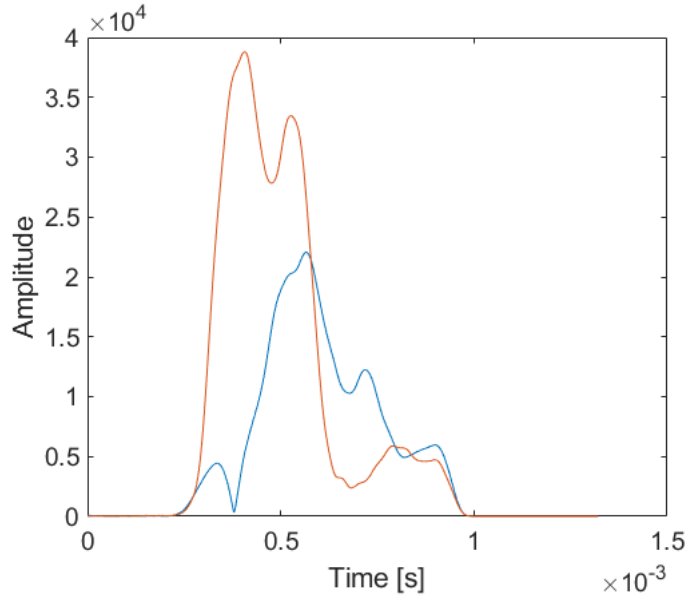


Figure 6.12: Temporal response at 60 kHz

#### 6.4.1 NESC Standard for Shell Rot

Based on the national electric safety code (NESC), the shell rot of utility poles can be examined using a shell rot gauge. Similar to the *hardness test* in metallurgy (DeGarmo et al., 1997), a shell rot gauge targets the differences in mechanical properties between the healthy and decaying poles. It can be measured by imposing a load through a sharp apparatus to create a permanent deformation in the form of an indentation or penetration. The level of indentation is an indicator of its hardness. Normally, a healthy wood pole exhibits a higher hardness value compared to a decay pole. The gauge allows an inspector to use a simple hammer as a load with a shell-rot gauge to evaluate its hardness. Fig. 6.13c shows a field inspector hammering the gauge against the pole surface to determine the level of penetration. An image of a shell rot gauge is illustrated in Fig. 6.13a from (Freeman, 2007). The level of penetration is converted into the *reduced circumference* expressed simply as,

$$C_{\text{red}} = C_0 - 2\pi r_{\text{red}}, \quad (6.1)$$

where  $C_0$  is the original circumference, and  $r_{\text{red}}$  is the depth of indentation obtained from the shell-rot gauge. In practice, the inspector will perform this shell rot test at three different points around the circumference at  $120^\circ$  apart to obtain an average reduced circumference (see Fig. 6.13b). Based on the US 1730-121 directives (Morrell et al., 1996), the pass/fail is detailed in Fig. 6.14. Based on the climatic condition which creates different loading requirements for the wooden utility poles, the reduced circumference outlined in Fig.6.14a is based on the different loading requirements in the U.S. map shown in Fig. 6.14.

## 6.4.2 Preparation and Procedures

Based on the NESC standard, a sound and a shell-decay pole are selected for this experiment to validate the finding. The pole selected will have the same GL dimension of 40-inch circumference. A larger circumference pole provides a greater temporal separation between the wavepackets, reducing the wave interference. Fig. 6.15 shows the 0-180 configuration for the UB1000 probes mounted at the GL region. Shell-rot measurements were performed at three evenly-spaced locations at the GL to calculate the reduced circumference. Pole ID 16529 is a healthy pole without any indication of shell rot. Pole ID 16530 has an initial indication of shell rot. The result shows approximately 1/4 inch penetration which equates to a reduced circumference of 38.7 inches. According to the NESC table in Fig. 6.14a and the pole location shown in Fig. 6.15c, the minimum reduced circumference is 36.3 inches. Consequently, this pole passes the test, but it requires close monitoring in the next few years.

## 6.4.3 TF Domain Analysis

The raw signals obtained from the UB1000 using the 0-180 configuration are depicted in Fig. 6.16a and b. The same probe set is used in both specimens to variation from the

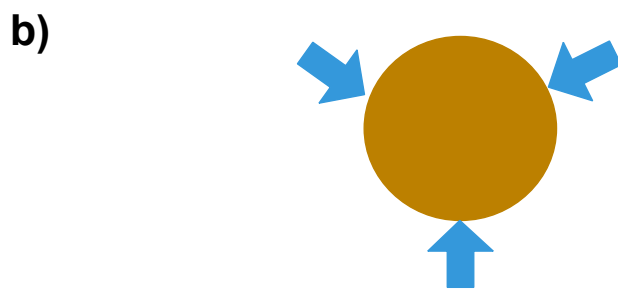
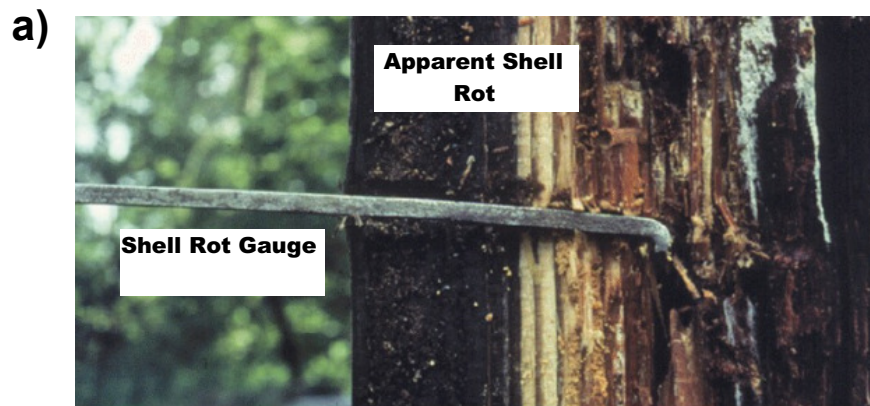


Figure 6.13: Shell Rot Demonstration.

a)

Reduced circumferences for NESC Rules 250B, 250C, and 250D

	Rule 250B – Combined ice and wind district loading	Rule 250C - Extreme wind and Rule 250D - Extreme ice and concurrent wind
Original Circumference (in)	Minimum Reduced Circumference (in) (Based on 2/3 initial strength)	Minimum Reduced Circumference (in) (Based on 3/4 of initial strength)
30	26.2	27.3
31	27.1	28.2
32	28.0	29.1
33	28.8	30.0
34	29.7	30.9
35	30.6	31.8
36	31.5	32.7
37	32.3	33.6
38	33.2	34.5
39	34.1	35.4
40	35.0	36.3
41	35.8	37.3

b)

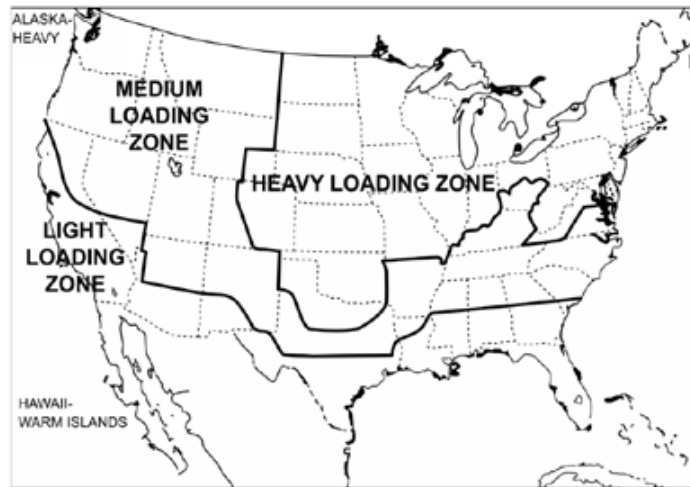


Figure 6.14: NESC standard for shell rot.

hardware. Based on the SNR of signals from both specimens, they are strong enough for the subsequent T-F analyses.

The TF domain representation of Pole ID 16529 is illustrated in Fig. 6.17a. Four main clusters of enhanced energy clusters are located at around 400, 500, 650, and 750  $\mu$ s. It appears to have four different wave modes reaching the receiving end. However, on

a)

POLE ID: 16529



b)

POLE ID: 16530



c)

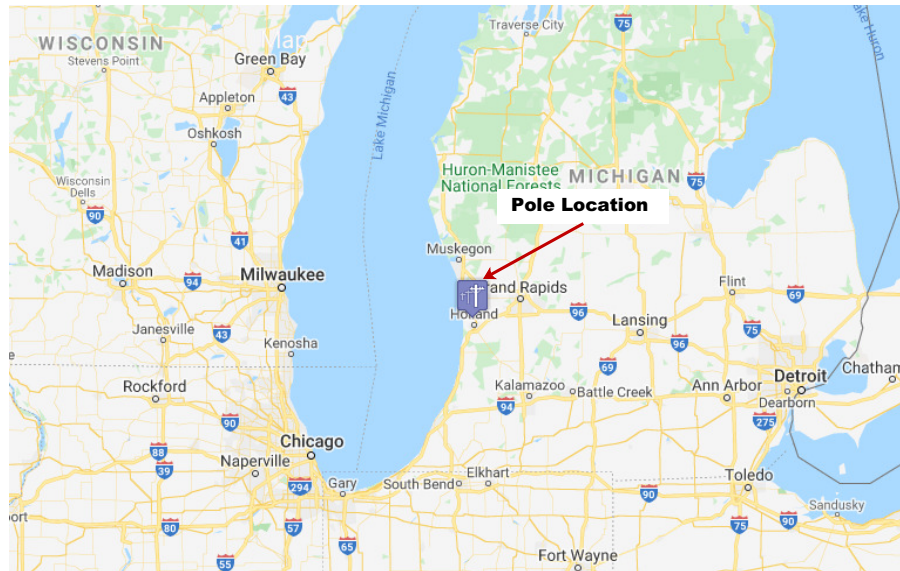


Figure 6.15: Two UB1000 at the GL region of the two selected poles and their geographical locations provided by (Hall, 2016).

a closer look at the spectral domain, the first two clusters appear to have similar spectral characteristics. This can be analyzed by examining the spectral response at fixed times. There is a pronounced energy depletion separating the first two clusters and the last two clusters at around  $t = 600 \mu s$ . A closer look reveals a very faint energy cluster at  $300 \mu s$ . This result can be better illustrated by the temporal response at the resonant frequency

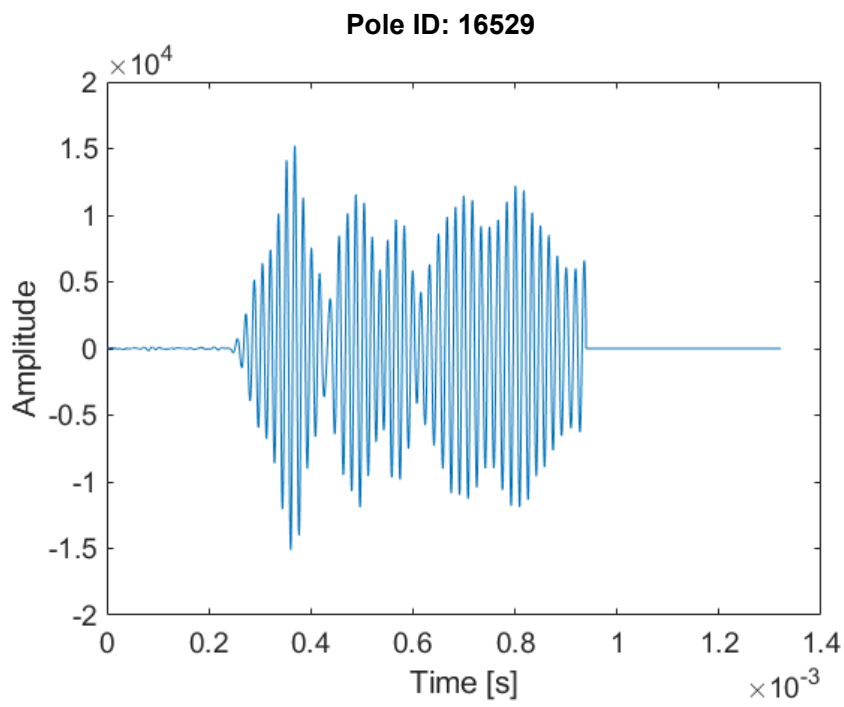
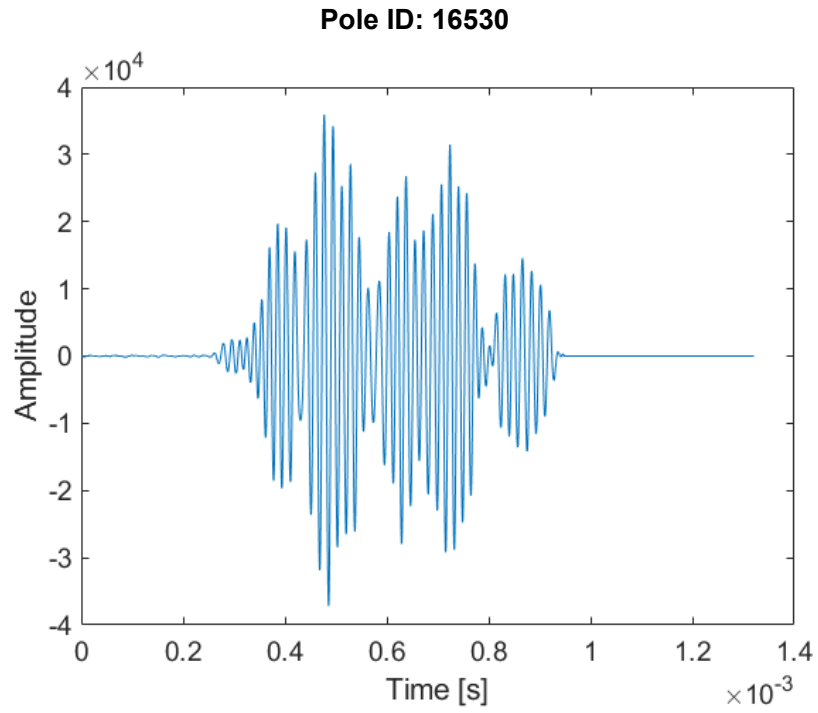


Figure 6.16: Raw ADC signal generated by the UB1000.

shown in Fig. 6.17b. In the time domain, the initial feature shows at around  $290 \mu\text{s}$  which is the first arrival (AW1) traveling radially. Using the expected TOF ratio of 1.5, the AW2 should appear at  $420 \mu\text{s}$  which is at the “valley” between two neighboring energy peaks. This is mainly due to the imperfect cylindrical symmetry of the wood and because the positioning of the two waveguides are not  $180^\circ$  apart. This results in a greater temporal separation of the same arrival mode. Thus, two separated energy peaks appear on either side of the expected arrival time in Fig. 6.17b. This is further evident in AW3, which is a normal encounter to see separating energy peaks in empirical data. The TOF can be estimated by taking the average of the neighboring peaks and using the highest peak as the energy response of respective arrival mode. The results of TOF and energy peak of Pole 16529 are shown in Table 6.3

Based on the performed hardness test using a shell-rot gauge, the inspection result of Pole ID 16530 indicates that the shell rot of 0.2 inch is measured at three equally spaced positions around the pole at the glsgl region. The calculated reduced circumference is 38.7 inches. With the obtained raw data shown in Fig. 6.16, a TF domain representation is illustrated in Fig. 6.18. The temporal location of AW1 is unclear. A close examination reveals an interference pattern occurs at around  $t = 300 \mu\text{s}$  (circled in dotted red). AW1 and AW2 may be interfering with each other. Since they formed a clearly composite signal, *decomposition* can be conducted to decouple the two arrival modes. Decomposition is a necessary extension of this work to compute the proper energy response level more precisely. At the moment, the arrival time and the amplitude of AW1 are unable to be resolved.

Another reason the AW2 region is determined to be between  $310$  and  $520 \mu\text{s}$  is due to the similarity of the frequency signature. When observing AW2 from Fig. 6.17, the spectral domain suggests a similar feature of two energy clusters with a distinct separation at a higher frequency. Due to the scope of this study, the details of the dispersive properties of the AW2 will not be further discussed, but will be mentioned in the future work. Finally,



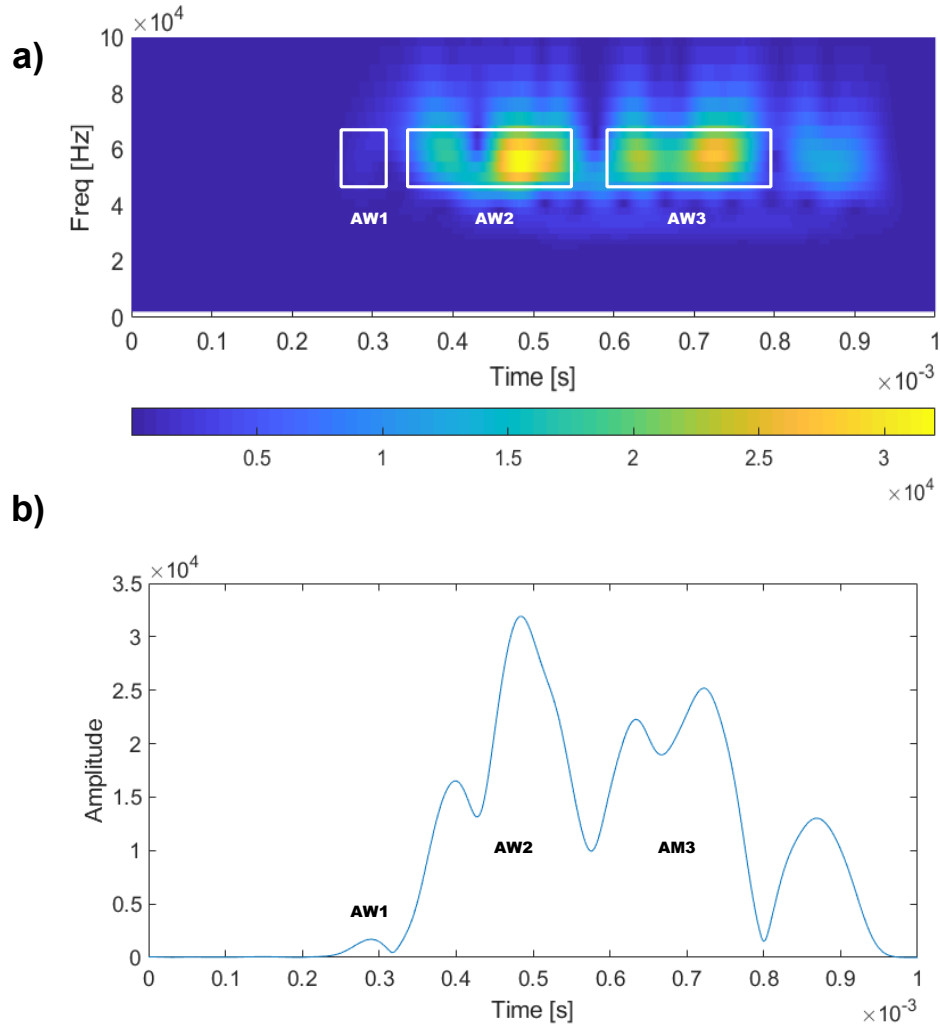


Figure 6.17: T-F domain representation of Pole ID: 16529. a) Gabor wavelet domain representation and b) temporal response at the resonant frequency.

another spike of energy occurs at a much later time. This spike of energy is determined to be AW3 based on the similar spectral signature of AW3 illustrated in Fig. 6.17. Fig. 6.19 depicts the similarities of AW and AW3 in the T-F domain between Pole 16529 and Pole 16530.

The results from the two specimens are summarized in Table 6.3. The AW1 was not detected in either case due to wave interference between AW1 and AW2 in Pole 16530. The AW2 is detected in both cases. The relative difference of TOF is about 3%. However,

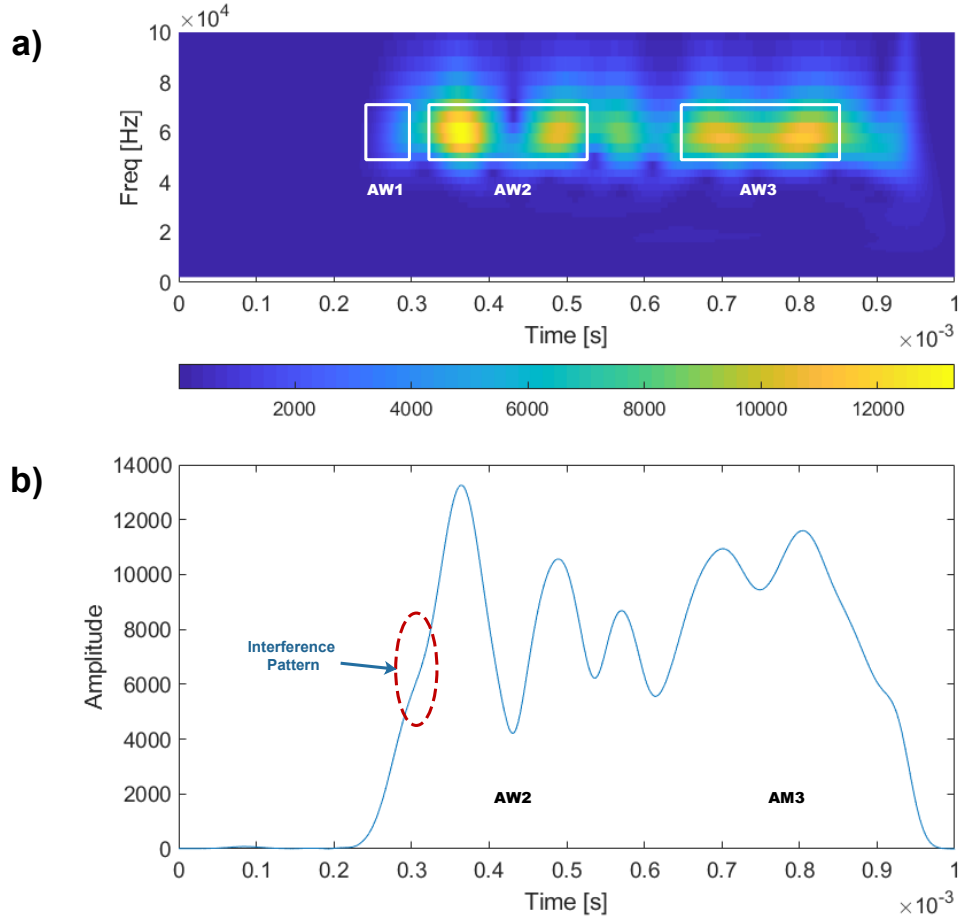


Figure 6.18: T-F domain representation of Pole ID: 16530. a) Gabor wavelet domain representation and b) temporal response at the resonant frequency.

I.D.	16529		16530	
	TOF	Energy Peak	TOF	Energy Peak
AW1	293	1980	n/a	n/a
AW2	438	32030	425	13250
AW3	678	27540	752	11590

Table 6.3: Extracted TOFs and peak energy levels between an healthy pole (16529) and a suspected shell rot pole (16530)

there is a strong attenuation in the energy peak between the poles. The strong energy attenuation combined with similar TOF values suggests the AW2 has traveled through high moisture content regions. Preliminary findings from Chapter 4 suggests that AW2 relates

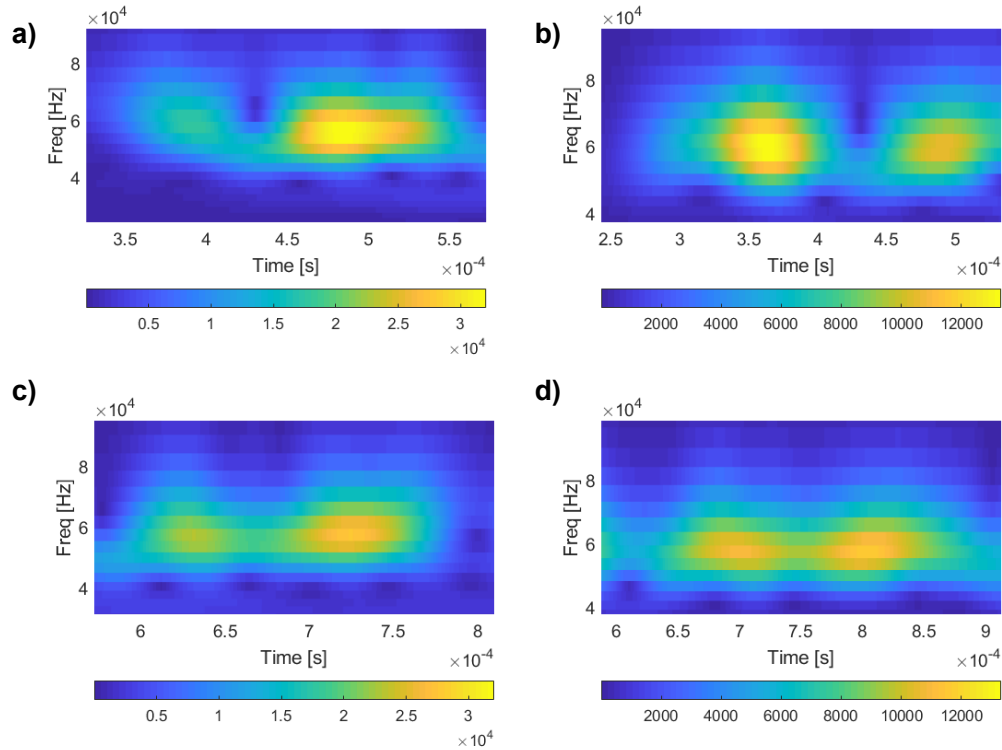


Figure 6.19: Feature comparison of the different arrival wavemode between the two cases. a) and c) are the TF representation of pole ID 16529. b) and d) are the TF representation of Pole ID 16530.

to the interior propagation, the strong attenuation combined with a similar TOF suggests high moisture content in the interior region. This remark supports the notion that decay of wood requires high moisture environment within the medium as suggested by (Green III et al., 1995).

The detected AW3 illustrates a very different picture. Pole 16530 has a greater attenuation compared to Pole 16529. The TOF also exhibits a greater delay with a relative difference of 11%. The combination of both delays in TOF and high moisture content rules out the possibility of only high moisture content within the shell region, but there is strong evidence that a mechanical degradation occurred in the shell region. Another indicator for potential mechanical issue can be inferred by examining the FWHM of the energy response.

According to the analytical result detailed in Chapter 3, the diffusive effect is related to the change in Poisson's ratio. By examining the width of the energy packets, the FWHM for Pole 16529 has a value of  $200 \mu\text{s}$ , and the FWHM for Pole 16530 is much greater to a value of  $300 \mu\text{s}$ . The latency of TOF, an increase of the FWHM, and the attenuation of energy point to a conclusion of a degradation of the mechanical properties and support the numerical and analytical findings. To better illustrate the FWHM in both cases, Fig. 6.20 superimposes the temporal energy plots of both specimens to better illustrate the difference in FWHMs.

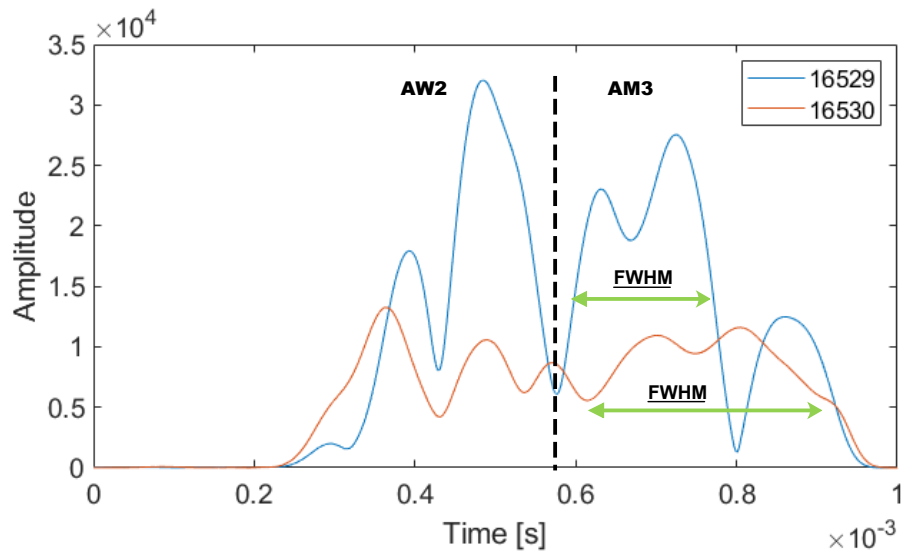


Figure 6.20: Temporal response at the resonance for pole 16530 (Marginal Pass) and 16529 (OK)

## 6.5 Possible Classification of the Selected Features

In order to further demonstrate the effectiveness of the proposed analysis, eighteen fielded utility poles with the same GL dimensions are used for this experiment. The GL conditions are assessed using the hardness test with a shell rot gauge. Each GL condition is determined based on a field inspector and the NESC Table listed in Fig. 6.14. Using the

extracted features of the peak energy TOF and the computed peak energy values from the Gabor Wavelet analysis for the AW3, the results are shown in Table 6.4. Passed, marginal passed and failed poles are designated with green, yellow and red, respectively. The corresponding values are plotted on a 2D feature plot depicted in Fig. 6.18. The labeled poles are colored in Green, yellow and red markers according to the NESC standard. The feature plot suggests that the pass or “green” poles tend to have higher group velocity and relatively stronger energy response. The failed or “red” and the marginally passed or “yellow” poles tend to have lower group velocity accompanied by weaker energy response. The characteristics of the TOF and the energy response result in a distinct division between the passed poles, the marginal passed, and the failed poles. This distinct difference allows a linear classifier to be developed to help distinguish the different poles. Two factors contribute to the sparsity of the feature plot in Fig. 6.20. Firstly, based on the previous findings, mechanically degraded poles possess a strong energy attenuation and slow propagation speed of the Rayleigh mode resulting in data clustering in the low energy and high arrival time region of the feature plot. Secondly, the sample size can affect the completeness of the feature plot. A more representative data collection and greater sample size reduce the sparsity and variation of the data clusters. If a single feature of either the peak energy TOF or the peak energy is used, this distinction might not be discovered.

Even though the focus of this study is strictly to uncover the characteristics and feasibility of the proposed physics-based signal analysis, it is a logical extension to further investigate the future development of utilizing advanced pattern classification techniques classify the GL condition. Chapter 7.3 will broadly discuss some potential approaches of employing linear classifier for this study.

Green			Yellow		
ID	TOF	Energy Peak	ID	TOF	Energy Peak
16337	722	1.01e3	16530	805	1.16e4
16529	680	2.75e4	15307	749	1.57e3
16581	702	2.08e4	17216	849	9.87e3
16583	749	3.48e4	39066	793	2.3e3
16584	706	5.77e3	96004	748	4.24e3
16587	744	6.04e3	Red		
16591	732	5.19e3	ID	TOF	Energy Peak
17214	718	8.29e3	15318	803	2.25e3
			17400	826	1.56e4

Table 6.4: A comparative result between the hardness test and the resultant TF domain analysis

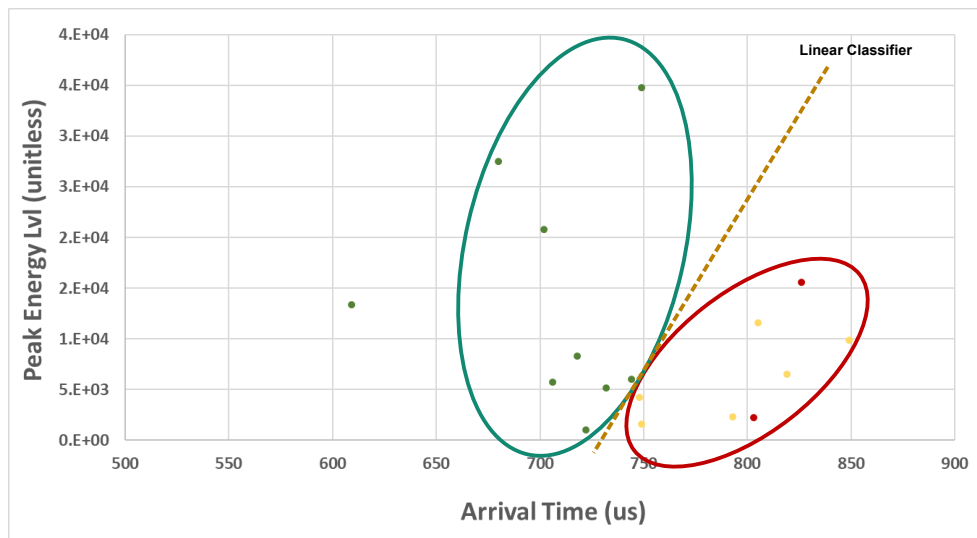


Figure 6.21: A feature plot of the extracted features and their resulted designation from the described expert assessment.

## 6.6 Summary and Discussion

This chapter focuses on the empirical validation of the physics-based extraction of the important features that help characterize the wooden medium using the developed UB1000 system. Using the proposed analysis algorithm based on Gabor continuous wavelet transformation and the expert labeling process of using the shell-rot gauge as a hardness test

and NESC standard of reduced circumference, the extracted peak energy time and the energy levels have produced classifiable clusters in the feature plot shown in Fig. 6.21. This finding is encouraging and suggests the possibility of employing binary classification. Fig. 6.21 also indicates a large scattering of the data cluster, which can be an indication of the signal variation. This variation can be contributed by several factors, including hardware and the assessment process. The consistency of the signal response is an important integral to examine the effectiveness of this technique, yet, it is not the focal point of this study. An additional experiment about the process variation will be analyzed in Appendix B to establish a confidence level in the GL assessment process and the UB1000 system. Accurate classification of the shell region at the GL GL relies on improving the following aspects. Based on the appendix, it offers a drastic improvement over the traditional ultrasonic assessment. It still possesses some variations that might warrant a further investigation to reduce the size of data scattering. Secondly, data collection according to geographical locations allows examining the pole population under a similar climate and soil conditions, reducing the data variation in the feature plot. To establish a confidence level for classification, the sample size can be determined by the estimated standard deviation of the population with a predetermined confidence level. According to (Kotrlik and Higgins, 2001), calculation such as the Cochran's formula can be employed for sample size determination. This consideration can result in a complete picture of the data cluster, giving greater confidence about performance of the classification.

# Chapter 7

## Conclusions and Future Work

This chapter summarizes this dissertation and includes the implications of the contributions highlighted in Chapter 1. The possible future work followed from the findings will be briefly discussed in a much broader sense.

### 7.1 Concluding Remarks

This study focuses primarily on the shell region assessment at the GL level ( $\approx 2$  inches above grade). Using the proposed embedded waveguide excitation, this study employs the elastodynamic principles and discovers the subsurface energy propagation closely resemble surface mode excited by contact-based excitation with enhanced energy deposition equal to the depth of insertion using the proposed waveguide. The diffusive property of the induced wave mode is found to be a function of the Poisson ratio of the medium. This finding was validated through a developed high-fidelity numerical model imposing the orthotropic and the poroelastic assumptions. The simulated waveguide response is studied and the arrival wave 3 (AW3) governed by the Rayleigh mode propagating within the shell region is discovered. By extracting the AW3 from the complex energy response, it allows the char-



acterization of the shell region condition. The developed numerical model also suggests that the incipient decay and moisture level are correlated with the TOF at the peak response and energy levels of the received ultrasonic signal. Built upon the findings of the numerical model, Sensitive features that characterize the material properties were discussed in Chapter 4 and selected for the TF-domain analysis. In Chapter 5, the STFT and Gabor CWT methods were compared. Based on the resulted TF-domain analysis technique and the findings from the physics model, the FWHM, peak energy TOF, and the attenuation information are selected to characterize the moisture content and the mechanical decay in the medium. Extensive empirical studies with known conditions are discussed in Chapter 6 using the developed UB1000 system. The proposed physics-based analysis technique was compared with the results from the standard invasive assessment. This finding validates the application of the proposed assessment method for characterizing wooden pole conditions. It establishes a scientific foundation for future studies as an extension of this work.

## **7.2 Contributions Summary of this work**

### **Contribution 1: Formulation of the Embedded Waveguide Excitation**

Based on embedded waveguide inserted directly into the medium as a novel ultrasonic radiation mechanism, this methodology bypasses the surface variation allowing the ultrasonic wave to be introduced directly into the wooden medium. Through systematic formulation and a numerical FEM model using the isotropic assumption under plane geometry, the analytical formulation is validated qualitatively by the numerical results. They both suggest the generation of a subsurface Rayleigh disturbance propagating along the half-space boundary (Chapter 3), which has never been previously studied. This work further reveals the trajectory if the disturbance following the half-space boundary, and discovers

the relationship between the diffusive property of the propagation wave and the Poisson's ratio of the medium.

### **Contribution 2: High-Fidelity Numerical Model of the GL region**

This dissertation developed a high-fidelity FEM model (Lee et al., 2020) of the cross-sectional region of a utility pole. This model is capable of simulating poroelastic propagation based on Biot's formulation. The inclusion of the solid and fluid motions under elastic disturbance allows the moisture saturation levels in wood and the incipient decay to be simulated. Under the orthotropic cylindrical symmetry assumption, the model uses the computational upscaling technique to transform a complex microscopic structure of wood into a set of manageable finite elements by determining the effective properties. The wave characteristics agree with the results produced previously by other theoretical and FEM numerical models. To further enhance its fidelity, the structural interaction between the wooden medium and the energy source of employing embedded waveguide excitation described in Contribution 1 is also modeled. It is the first holistic and high-fidelity model that numerically describes the poroelastic wave propagation in the orthotropic cross-sectional region of a wooden utility pole.

### **Contribution 3: Discovery of the arrival wave mode**

The high fidelity model forms a reliable scientific foundation to analyze the behavioral response of the receiving waveguide in the temporal domain under the imposed boundary conditions. The result suggests the resultant subsurface Rayleigh disturbance, which is termed AW3 can be detected and identified in the waveguide response due to its slow diffusive property as propagating along the half-space. As a result, the AW3 can be decoupled from the complex response obtained from the receiving waveguide. The numerical

model provides a complete picture to extract the expected region of the AW3 response. The extraction process is detailed in Chapter 4 and published in (Lee et al., 2020). This dissertation contributes to the discovery of the AW3 mode using the embedded waveguide approach that was not previously known.

#### **Contribution 4: Signal Analysis and Characterization of the Material**

By isolating the arrival mode (AW3) in the waveguide temporal response, it is found that the incipient decay in wood impacts both the TOF at the peak energy level and the energy attenuation of AW3, while high moisture content in the porous matrix correlates with energy attenuation of AW3. Combining the arrival wave mode extraction detailed in Chapter 4 and a chosen TF domain approach via the wavelet domain transformation, this technique extracts the temporal and energy information from the signal for characterization of the wooden medium. This method is validated through a numerical model detailed in Chapter 4. Consequently, this work produces a wavelet-based holistic approach for full-waveform analysis that was not previously employed for wooden shell region condition assessment.

#### **Contribution 5: Empirical Validation and Physics-based Feature Selection**

Extensive empirical study and testing using the patented UB1000 system were performed under both controlled and realistic field environments. The obtained raw signal was fed into the proposed holistic algorithm detailed in Chapter 5. The selected features produced from the Gabor wavelet transformation are plotted in Fig. 6.21. Using a condition assessment labeling system (green, yellow, and red) performed by the field expert assessment and in accordance with the NESC standards, a pronounced decision boundary

is illustrated in Fig. 6.21. The attempt of using pattern classification analysis of the shell region at the GL region has not been previously documented and published. The result has a profound implication for future research opportunity of using pattern classification techniques to characterize the shell region condition and ultimately determining the remaining strength of a wooden pole.

### **List of Journal Publications:**

- Y. Lee, M. Mahoor, and W. Hall. A 2D numerical model of ultrasonic wave propagation in wooden utility poles using embedded waveguide excitation technique. *Wood and Fiber Science*, 52(1):87–101, 2020.

### **List of Conference Proceedings:**

- Y. Lee, M. Mahoor, and W. Hall. Rayleigh mode excitation at the half-space boundary in wood using embedded elastic waveguides. In *Proceedings of the 2019 Society of Wood Science and Technology International Convention*, Tenaya Lodge, Yosemite, California USA, pages 212–219. Society of Wood Science and Technology, 2019.
- Y. Lee and W. Hall. Diffusive subsurface propagation of Rayleigh mode induced by embedded ultrasonic waveguide. In *Proceedings of the 2020 Acoustical Society of America 179th Meeting*. Acoustical Society of America ASA, 2020. Manuscript accepted for publication.

## List of Patents:

- Y. Lee, and W. Hall. Insertable waveguide to improve acoustic signal transmission in wooden specimen, Apr. 2 2020. US Patent App. 16/518,789
- D. Hall, Y. Lee, and W. Hall. Acoustic probe for inspection of wooden specimen, May 212020. US Patent App. 16/518,762.

## 7.3 Future Work

### 7.3.1 Contact-based Ultrasonic Waveguide Excitation

The development of the analytical formulation of the embedded ultrasonic waveguide excitation provides a comprehensive understanding of the radiation and propagational characteristics. The diffusive property due to the difference in phase speed between the *fast* and *slow* modes is closely related to the physical properties, which was not previously studied. A quantitative relation between the Poisson's ratio and the diffusive property was detailed in Chapter 3, provides a means for the later analysis using the FWHM metrics. This study did not link the Poisson's ratio to other more familiar quantities such as the MOE and MOR. However, through the use of the *Lamé* relations, a functional relationship can be derived, which could link the diffusive properties to MOE and MOR.

Through both analytical and numerical methodology, the excited subsurface Rayleigh mode is discovered and systemically validated. The radiation mechanism bypasses the surface of the medium, eliminates any influence of any surface irregularity . This in turn enhances the consistency of ultrasonic transmission and reception, which is evident in Chapter 6. A separate experiment detailed in the Appendix B was conducted to further evaluate the overall consistency of the proposed assessment techniques by examining the received waveform.

In some applications, a contact-based waveguide might be the only option. In that case, the mechanism of the ultrasonic radiation will be different due to the alteration of the boundary condition. This research is already underway (see Fig. 7.1) with the United State Forrest Product Laboratory (US-FPL) in Madison Wisconsin to examine the Glulam wood composites. Nevertheless, the proposed analysis process can be applied to the contact-based waveguide excitation to characterize the medium.

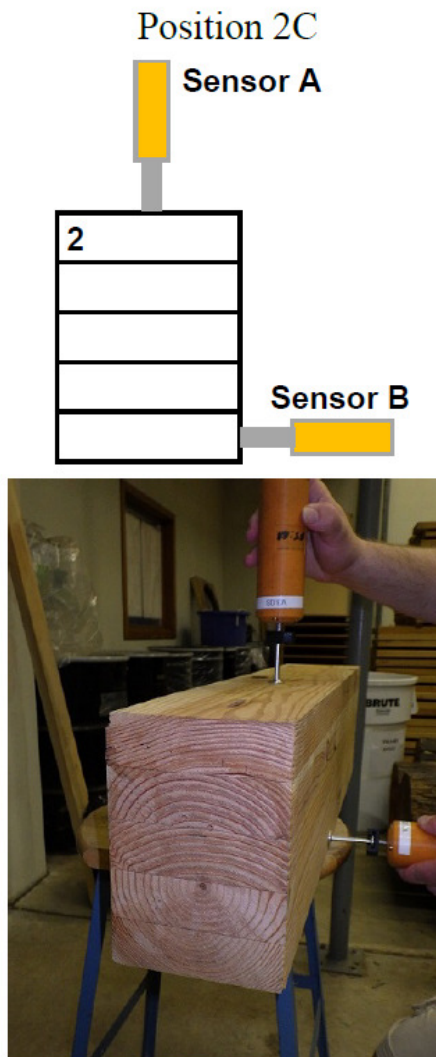


Figure 7.1: An example application using contact-based waveguide excitation with the UB1000 system

### **7.3.2 Narrow-band vs. broad-band analysis**

This study employs a narrow-band ultrasonic transducer based on two reasons. Firstly, the wooden medium has a strong energy dissipation and absorption properties. It requires a high-power transducer to pump a sufficient amount of energy into the medium. Since a narrow-band transducer focuses in a single spectral band, it is suitable in high-power applications. Secondly, narrow-band transducers have a relatively long decay rate compared to a broad-band transducer; Hence, the quasi-steady can be reasonably assumed. That allows the steady-state formulation detailed in Chapter 3 to be applied. Since this study focuses on the single-band excitation, the temporal understanding of the waveform characteristics becomes more manageable. In addition, the findings and the knowledge produced from this work may provide insight into future studies of employing the multi-band frequency ultrasonic excitation. The multi-band frequency excitation offers additional advantages of analyzing the dispersive relation of the medium by measuring the group speeds of AW1, AW2, and AW3 as functions of the different frequencies, further enhancing the capability of GL region characterization.

### **7.3.3 Analytical Formulation of Transient Poroelastic Wave**

This study has systematically formulated the EOM for the propagation and radiation of the elastic stress wave using the proposed embedded waveguide technique. The resultant closed form solutions in both surface (3.27) and subsurface (3.37) regions give an important understanding between the wave characteristics and the mechanical properties. The formulation is based on the assumption of isotropy. It is a logical extension and a more desirable approach to derive a closed-form formulation under the porous medium to explore other parametric relations between the wave and medium characteristics neglected in the isotropic domain.

The developed analytical formulation is built on the quasi-steady state assumptions. This is a valid assumption due to the narrow spectral response of the Langevin transducer. Due to the well-known dispersive property of wood in various conditions, wide spectral analysis can be desirable to develop the phase velocity dispersion curves through multi-mode analysis (Rose, 2003). The wide spectral analysis requires a amplitude modulation with rapid temporal change, making the presented quasi-steady state assumption and the associated formulation invalid. It is A logical extension to formulate a transient response of the embedded waveguide excitation based on the similar approach presented to reveal the rich information hidden in the phase velocity dispersion curve.

#### **7.3.4 Signal Decomposition and Arrival Wave Identification**

The shell region Rayleigh mode labeled AW3 was observed qualitatively based on the developed numerical model in Chapter 4. The model was derived quantitatively by the analytical finding from Chapter 3. This discovery and the detailed analyses yield the first shell region characterization in non-destructive evaluation. The trajectories of AW1 and AW2 also play important roles in the heart region characterization. In the waveform, AW1, AW2 and AW3 are close together temporally, inevitably induce composite interference. In larger poles, when times between arrivals are greater, the interference between waveforms will not as pronounced. Comparing a smaller pole, AW2 and AW3 interference can be quite dramatic. The impact of the interference in the received waveform can be alleviated by imposing a decomposition filter as an intermediate step before extracting each arrival wave.

This study has proposed a technique of determining the arrival wave based on the expected arrival regions in the time domain. The arrival region is selected qualitatively based on the developed finite-element model with the porous orthotropic formulation. The spec-



tral response of different wave modes is worth a further investigation using multi-band ultrasonic transmission. Its result can produce spectral signatures of different arrivals, in turn, it gives a more definitive identification of the arrival mode.

### **7.3.5 Ray Tracing and Tomographic Inversion**

This study establishes a numerical model allowing a qualitative determination of the shell region wave trajectory. By exploding the waveform in the TF-domain representation, the results agree with the NESC standards to characterize the shell region property from a population. The statistical significance between a healthy and rotted shell region establishes a confident level of the proposed methodology. The waveform trajectories of AW1 and AW2 enable the examinations of other regions in the cross-section. However, a quantitative determination of the wave trajectory might be desirable. This can be accomplished by the *ray tracing* technique, which has been thoroughly studied and extensively used in optics. This technique has been explored in ultrasonic applications, which is termed the *elastic wave ray tracing*. Prior studies by (Rathore et al., 2003), (Ogilvy, 1985) and (Pereyra, 2000) could establish the needed technical foundation for future work.

Another benefit of quantitative determination of wave trajectory is to improve the accuracy of the ultrasonic tomographic inversion. Traditional ultrasonic tomographic inversion focuses on the initial detectable arrival combine with *Radon transform* to produce an image of a cross-sectional region. This method has been used with UB1000 with some successes (see Fig. 7.2). However, elastic waves do not always propagate at a straight line, as shown in this study. The determination of the curved wave path can improve the inversion quality. Furthermore, the discovery of the different arrival modes gives trajectory information containing in each waveform. The advancements produced by this work can potentially relax the requirement by minimizing the total number of sensors.

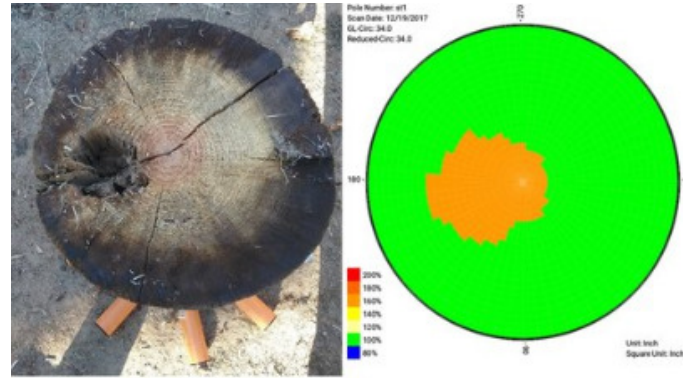


Figure 7.2: Tomographic Inversion using the UB1000 system (Hall, 2016).

### 7.3.6 Nonseparable Pattern Classification

This study has systematically explored different physical principles that characterize the wooden medium. The associated TF-domain analysis and an algorithm have been developed. This process leads to a set of selected features sensitive enough to detect the variation of the physical properties. As a result, a mix of various conditions of fifteen utility poles was used. Based on the selected features and a labeling process based on field expert knowledge and the well-established NESC industry standards, the produced feature plot Fig. 6.21 illustrates a clear decision boundary. However, Fig. 6.21 also illustrates close proximity between the two categories. It is expected that the intrinsic noise from the inspection variations and the measurement can perturb the sample set, resulting in *non-separable behavior* as more samples are collected. In that case, the error rate for a linear discriminant function can be high. Some of the approaches, including heuristic modifications to the error-correction rules (Roychowdhury et al., 1995), and perceptron learning algorithms (Duda et al., 2012) can be used to determine the optimal linear discriminant function.

# Bibliography

- J. D. Achenbach and H. I. Epstein. Dynamic interaction of a layer and a half-space. *Journal of the Engineering Mechanics Division*, 93(5):27–42, 1967. 42
- D. ANSI. O5. 1 wood poles. *Specifications and Dimensions*, 2017. 11
- F. Auger, P. Flandrin, Y.-T. Lin, S. McLaughlin, S. Meignen, T. Oberlin, and H.-T. Wu. Time-frequency reassignment and synchrosqueezing: An overview. *IEEE Signal Processing Magazine*, 30(6):32–41, 2013. 92
- H. M. Barnes. Wood preservation. *Encyclopaedia of pest management*, 2:719–721, 2007. 19
- F. Beall. Overview of the use of ultrasonic technologies in research on wood properties. *Wood Science and Technology*, 36(3):197–212, 2002. 34, 35
- K. Bernan, S. Campbell, and R. Petzold. Numerical solution of initial-value problems in differential algebraic equations. 1989. 70
- B. Bernhardt. Wood poles still best alternative for most uses. *Natural Gas & Electricity*, 34(2):9–14, 2017. 11
- G. S. Bhuyan. Condition based serviceability and reliability assessment of wood pole structures. In *ESMO'98-1998 IEEE 8th International Conference on Transmission and Distribution Construction, Operation and Live-Line Maintenance Proceedings ESMO'98 Proceedings. ESMO 98 The Power is in Your Hand*, pages 333–339. IEEE, 1998. 2
- M. Biot. Theory of elastic waves in a fluid-saturated porous solid. 1. low frequency range. *J. Acoust. Soc. Am.*, 28:168–178, 1956. 3, 82, 83

- R. A. Blanchette, B. W. Held, J. A. Jurgens, D. L. McNew, T. C. Harrington, S. M. Duncan, and R. L. Farrell. Wood-destroying soft rot fungi in the historic expedition huts of antarctica. *Appl. Environ. Microbiol.*, 70(3):1328–1335, 2004. xii, 85, 86
- B. Boashash. *Time-frequency signal analysis and processing: a comprehensive reference*. Academic Press, 2015. 90
- J. Bodig, G. E. Phillips, J. R. Goodman, and P. G. Landers. Reliability of wood transmission structures through nondestructive evaluation. *IEEE Transactions on Power Apparatus and Systems*, (8):2409–2414, 1982. 1
- C. A. Bolin and S. T. Smith. Life cycle assessment of pentachlorophenol-treated wooden utility poles with comparisons to steel and concrete utility poles. *Renewable and Sustainable Energy Reviews*, 15(5):2475–2486, 2011. 10
- K. E. Brenan, S. L. Campbell, and L. R. Petzold. *Numerical solution of initial-value problems in differential-algebraic equations*, volume 14. Siam, 1996. 49, 73
- V. Bucur. An ultrasonic method for measuring the elastic constants of wood increment cores bored from living trees. *Ultrasonics*, 21(3):116–126, 1983. 22, 36
- V. Bucur. *Acoustics of wood*. Springer Science & Business Media, 2006. x, 15
- V. Bucur and I. Böhnke. Factors affecting ultrasonic measurements in solid wood. *Ultrasonics*, 32(5):385–390, 1994. x, 24
- V. Bucur and F. Feeney. Attenuation of ultrasound in solid wood. *Ultrasonics*, 30(2):76–81, 1992. 23
- W. Bulleit and R. Falk. Modeling stress wave passage times in wood utility poles. *Wood science and technology*, 19(2):183–191, 1985. 3, 25

- K. S. G. Cartwright and W. Findlay. Timber decay. *Biological Reviews*, 18(4):145–158, 1943. 16
- C. Chen and J. Guey. On the use of wigner distribution in ultrasonic nde. In *Review of Progress in Quantitative Nondestructive Evaluation*, pages 967–974. Springer, 1992. 89
- H.-I. Choi and W. J. Williams. Improved time-frequency representation of multicomponent signals using exponential kernels. *IEEE Transactions on Acoustics, Speech, and Signal Processing*, 37(6):862–871, 1989. 89
- S. Cochran, C. Demore, and C. Courtney. Modelling ultrasonic-transducer performance: One-dimensional models. In *Ultrasonic Transducers*, pages 187–219. Elsevier, 2012. xi, 60, 61
- G. L. Comstock. Longitudinal permeability of green eastern hemlock. *Forest Products Journal*, 15(10):441–449, 1965. 84
- E. B. Cowling. *Comparative biochemistry of the decay of sweetgum sapwood by white-rot and brown-rot fungi*. Number 1258. US Department of Agriculture, 1961. 16, 17
- D. J. Cown. Variation in tracheid dimensions in stem of a 26-year-old radiata pine tree. *Appita*, 28(4):237–245, 1975. 84
- S. F. Curling, C. A. Clausen, and J. E. Winandy. Relationships between mechanical properties, weight loss, and chemical composition of wood during incipient brownrot decay. *Forest Products Journal*, 52(7/8):34–39, 2002. xi, 80
- U. Dackermann, B. Skinner, and J. Li. Guided wave–based condition assessment of in situ timber utility poles using machine learning algorithms. *Structural Health Monitoring*, 13(4):374–388, 2014. 4, 5, 36

- S. Datla and M. Pandey. Estimation of life expectancy of wood poles in electrical distribution networks. *Structural safety*, 28(3):304–319, 2006. 1
- J. Davis, R. Davies, P. Wells, and N. Benci. A field transportable computerized tomography scanner for the nondestructive testing of wooden power poles. *Materials evaluation*, 51(3):332–337, 1993. 8
- E. P. DeGarmo, J. T. Black, R. A. Kohser, and B. E. Klamecki. *Materials and process in manufacturing*. Prentice Hall Upper Saddle River, 1997. 118
- L. R. Dragonette, D. M. Drumheller, C. F. Gaumont, D. H. Hughes, B. T. OConnor, N. Yen, and T. J. Yoder. The application of two-dimensional signal transformations to the analysis and synthesis of structural excitations observed in acoustical scattering. *Proceedings of the IEEE*, 84(9):1249–1263, 1996. 89
- R. O. Duda, P. E. Hart, and D. G. Stork. *Pattern classification*. John Wiley & Sons, 2012. 142
- R. A. Eaton, M. D. Hale, et al. *Wood: decay, pests and protection*. Chapman and Hall Ltd, 1993. 15
- W. E. Eslyn. Utility pole decay. *Wood Science and Technology*, 4(2):97–103, 1970. 8
- Z. E. A. Fellah, M. Fellah, C. Depollier, E. Ogam, and F. G. Mitri. Wave propagation in porous materials. *Computational and experimental studies of acoustic waves*, pages 99–119, 2018. 83
- R. Filter. The influence of wood pole preservatives on wood fire and electrical safety. *IEEE transactions on power apparatus and systems*, (10):3089–3095, 1984. 20

- P. Flandrin. Non-destructive evaluation in the time-frequency domain by means of the wigner-ville distribution. In *Signal processing and pattern recognition in nondestructive evaluation of materials*, pages 109–116. Springer, 1988. 89
- M. R. Fleming, M. C. Bhardwaj, J. J. Janowiak, J. E. Shield, R. Roy, D. K. Agrawal, L. S. Bauer, D. L. Miller, and K. Hoover. Noncontact ultrasound detection of exotic insects in wood packing materials. 2005. 34
- M. H. Freeman. Wood pole and crossarm maintenance and remedial treatment: A state of the industry review. In *Proceedings,... annual meeting of the American Wood Protection Association*, 2007. 118
- D. Gabor. Theory of communication. part 1: The analysis of information. *Journal of the Institution of Electrical Engineers-Part III: Radio and Communication Engineering*, 93 (26):429–441, 1946. 90
- J. Gallego-Juarez. Piezoelectric ceramics and ultrasonic transducers. *Journal of Physics E: Scientific Instruments*, 22(10):804, 1989. x, 27, 28, 31, 32, 41, 59
- J. A. Gallego-Juárez, G. Rodriguez-Corral, and L. Gaete-Garreton. An ultrasonic transducer for high power applications in gases. *Ultrasonics*, 16(6):267–271, 1978. 30
- W. Galligan. A status report nondestructive testing of wood. *Forest Products Journal*, 14: 221–227, 1964. 2
- C. C. Gerhards. Longitudinal stress waves for lumber stress grading: factors affecting applications: state of the art. *Forest Products Journal*, 32(2):20–25, 1982. 21
- W. Gindl, H. Gupta, T. Schöberl, H. Lichtenegger, and P. Fratzl. Mechanical properties of spruce wood cell walls by nanoindentation. *Applied Physics A*, 79(8):2069–2073, 2004. x, 14, 18

- J. H. Goll. The design of broad-band fluid-loaded ultrasonic transducers. *IEEE Transactions on Sonics and Ultrasonics*, 26(6):385–393, 1979. 27
- J. Goodman and A. Stewart. Wood pole management: utility case studies. *IEEE transactions on power delivery*, 5(1):422–426, 1990. 3
- D. W. Green, J. E. Winandy, and D. E. Kretschmann. Mechanical properties of wood. *Wood handbook: wood as an engineering material*. Madison, WI: USDA Forest Service, Forest Products Laboratory, 1999. General technical report FPL; GTR-113: Pages 4.1-4.45, 113, 1999. 67, 73, 111
- F. Green III, T. A. Kuster, and F. W. I. Guadalupe. The international research group on wood preservation. 1995. 15, 127
- D. Hall, Y. Lee, and W. Hall. Acoustic probe for inspection of wooden specimen, May 21 2020. US Patent App. 16/518,762. xii, 106, 107
- W. Hall. URL <https://www.gridmgr.com/>, 2016. xiii, 122, 142
- W. Han and R. Birkeland. Ultrasonic scanning of logs. *Industrial metrology*, 2(3-4):253–281, 1992. 4, 23, 34
- J. G. Haygreen, J. L. Bowyer, et al. *Forest products and wood science: an introduction*. Number Ed. 3. Iowa state university press, 1996. x, 17
- G. Hayward. The influence of pulser parameters on the transmission response of piezoelectric transducers. *Ultrasonics*, 23(3):103–112, 1985. 32
- R. C. Hibbeler and S. Fan. *Statics and mechanics of materials*, volume 2. Prentice Hall Upper Saddle River, 2004. 11



- T. L. Highley. Biodeterioration of wood. *Wood handbook: wood as an engineering material*. Madison, WI: USDA Forest Service, Forest Products Laboratory, 1999. General technical report FPL; GTR-113: Pages 13.1-13.16, 113, 1999. 80
- F. Isik and B. Li. Rapid assessment of wood density of live trees using the resistograph for selection in tree improvement programs. *Canadian Journal of Forest Research*, 33(12): 2426–2435, 2003. x, 10
- K. E. Jansen, C. H. Whiting, and G. M. Hulbert. A generalized- $\alpha$  method for integrating the filtered navier–stokes equations with a stabilized finite element method. *Computer methods in applied mechanics and engineering*, 190(3-4):305–319, 2000. 49
- D. L. Johnson, J. Koplik, and R. Dashen. Theory of dynamic permeability and tortuosity in fluid-saturated porous media. *Journal of fluid mechanics*, 176:379–402, 1987. 83
- A.-K. Kassam and L. N. Trefethen. Fourth-order time-stepping for stiff pdes. *SIAM Journal on Scientific Computing*, 26(4):1214–1233, 2005. 73
- K. Keller. *Electrical Safety Code Manual: A Plain Language Guide to National Electrical Code, OSHA and NFPA 70E*. Butterworth-Heinemann, 2010. 12
- H. Kim and S. W. Heo. Time-domain calculation of spectral centroid from backscattered ultrasound signals. *IEEE transactions on ultrasonics, ferroelectrics, and frequency control*, 59(6):1193–1200, 2012. 35
- Y. Y. Kim and E.-H. Kim. Effectiveness of the continuous wavelet transform in the analysis of some dispersive elastic waves. *The Journal of the Acoustical Society of America*, 110(1):86–94, 2001. 94
- H. Kolsky. *Stress waves in solids*, volume 1098. Courier Corporation, 1963. 37

- J. Kotrlik and C. Higgins. Organizational research: Determining appropriate sample size in survey research appropriate sample size in survey research. *Information technology, learning, and performance journal*, 19(1):43, 2001. 131
- A. Koubaa, S. T. Zhang, and S. Makni. Defining the transition from earlywood to latewood in black spruce based on intra-ring wood density profiles from x-ray densitometry. *Annals of Forest Science*, 59(5-6):511–518, 2002. 13
- F. T. Krogh. Changing stepsize in the integration of differential equations using modified divided differences. In *Proceedings of the Conference on the Numerical Solution of Ordinary Differential Equations*, pages 22–71. Springer, 1974. 73
- D. Lafarge, P. Lemarinier, J. F. Allard, and V. Tarnow. Dynamic compressibility of air in porous structures at audible frequencies. *The Journal of the Acoustical Society of America*, 102(4):1995–2006, 1997. 83
- Y. Lee and W. Hall. Insertable waveguide to improve acoustic signal transmission in wooden specimen, Apr. 2 2020. US Patent App. 16/518,789. xii, 109
- Y. Lee, M. Mahoor, and W. Hall. A 2d numerical model of ultrasonic wave propagation in wooden utility poles using embedded waveguide excitation technique. *Wood and Fiber Science*, 52(1):87–101, 2020. ix, xi, 49, 70, 71, 72, 74, 75, 78, 79, 134, 135
- R. B. A. Loan and L. Guarantee. Rural utilities service. 2006. 2
- A. Louis, P. Maa, and A. Rieder. Wavelets (stuttgart: Teubner) and (1997), 1994. 94
- S. Mallat. *A wavelet tour of signal processing*. Elsevier, 1999. 93
- M. Matyka, A. Khalili, and Z. Koza. Tortuosity-porosity relation in porous media flow. *Physical Review E*, 78(2):026306, 2008. 84

- A. Mishiro. Effect of density on ultrasonic velocity in wood. *Mokuzai Gakkaishi*, 42(9): 887–894, 1996a. 22
- A. Mishiro. Effects of grain and ring angles on ultrasonic velocity in wood. *Mokuzai Gakkaishi*, 42:211–215, 1996b. 22
- J. Morrell, C. Freitag, H. Chen, and C. Love. Utility pole research cooperative. 2006. x, 18
- J. J. Morrell. Estimated service life of wood poles. *Technical Bulletin, North American Wood Pole Council*, 2008. x, 1, 19, 20
- J. J. Morrell. Wood pole maintenance manual: 2012 edition. Technical report, Oregon State University. Forest Research Laboratory, 2012. x, 2, 16, 68
- J. J. Morrell et al. Wood pole maintenance manual. 1996. 2, 119
- D. E. Newland. Harmonic wavelets in vibrations and acoustics. *Philosophical Transactions of the Royal Society of London. Series A: Mathematical, Physical and Engineering Sciences*, 357(1760):2607–2625, 1999. 93
- W. K. Ngui, M. S. Leong, L. M. Hee, and A. M. Abdelrhman. Wavelet analysis: mother wavelet selection methods. In *Applied mechanics and materials*, volume 393, pages 953–958. Trans Tech Publ, 2013. 93
- J. Ogilvy. Computerized ultrasonic ray tracing in austenitic steel. *NDT international*, 18(2):67–77, 1985. 141
- J. Okyere and A. Cousin. The design of a high voltage scr pulse generator for ultrasonic pulse echo applications. *Ultrasonics*, 17(2):81–84, 1979. 32
- R. G. Payton. Wave fronts in wood. *The Quarterly Journal of Mechanics and Applied Mathematics*, 56(4):527–546, 2003. x, 3, 25, 26

- H. v. Pechmann and O. Schaile. Über die änderung der dynamischen festigkeit und der chemischen zusammensetzung des holzes durch den angriff holzzerstörender pilze. *Forstw. Cbl*, 69:441–466, 1950. 17
- V. Pereyra. Ray tracing methods for inverse problems. *Inverse Problems*, 16(6):R1, 2000. 141
- R. Prakash. Non-destructive testing of composites. *Composites*, 11(4):217–224, 1980. 35
- A. Ramos-Fernández, P. Sanz-Sánchez, and F. M. de Espinosa. Broad-band driving of echographic arrays using 10 ns-500 v efficient pulse generators. *Ultrasonics*, 25(4):221–228, 1987. 32
- S. Rathore, N. Kishore, and P. Munshi. An improved method for ray tracing through curved inhomogeneities in composite materials. *Journal of nondestructive evaluation*, 22(1):1–9, 2003. 141
- L. Rayleigh. On waves propagated along the plane surface of an elastic solid. *Proceedings of the London Mathematical Society*, 1(1):4–11, 1885. 44
- F. Rinn, F. Schweingruber, and E. Schär. Resistograph and x-ray density charts of wood. comparative evaluation of drill-resistance profiles and x-ray density charts of different wood species. *Holzforschung*, 50(4):303–311, 1996. 9
- J. L. Rose. Dispersion curves in guided wave testing. *Materials Evaluation*, 61(1):20–22, 2003. 140
- J. L. Rose. *Ultrasonic waves in solid media*. ASA, 2004. 42, 75
- V. P. Roychowdhury, K.-Y. Siu, and T. Kailath. Classification of linearly nonseparable patterns by linear threshold elements. *IEEE Transactions on Neural Networks*, 6(2):318–331, 1995. 142

- J. Salazar, A. Turó, J. A. Chávez, J. A. Ortega, and M. J. Garcia. High-power high-resolution pulser for air-coupled ultrasonic nde applications. *IEEE Transactions on Instrumentation and Measurement*, 52(6):1792–1798, 2003. x, 33
- J. San Emeterio, A. Ramos, P. Sanz, A. Ruiz, and A. Azbaid. Modeling ndt piezoelectric ultrasonic transmitters. *Ultrasonics*, 42(1-9):277–281, 2004. 62
- S. J. Sanabria, C. Mueller, J. Neuenschwander, P. Niemz, and U. Sennhauser. Air-coupled ultrasound as an accurate and reproducible method for bonding assessment of glued timber. *Wood science and technology*, 45(4):645–659, 2011. 34
- J. Sandoz. Grading of construction timber by ultrasound. *Wood Science and Technology*, 23(1):95–108, 1989. x, 22, 23
- J. Sandoz and O. Vanackere. Wood poles ageing and non destructive testing tool. 1997. x, 12
- O. Schmidt. *Wood and tree fungi*. Springer, 2006. 80
- D. L. Schmoldt, D. Zhu, and R. W. Conners. Nondestructive evaluation of hardwood logs using automated interpretation of ct images. In *Review of progress in quantitative non-destructive evaluation*, pages 2257–2264. Springer, 1993. 8
- S. I. Schubert, D. Gsell, J. Dual, M. Motavalli, and P. Niemz. Rolling shear modulus and damping factor of spruce and decayed spruce estimated by modal analysis. *Holz-forschung*, 60(1):78–84, 2006. 80
- A. Senalik, F. C. Beall, and H. Reis. Detection and assessment of wood decay in glulam beams using a decay rate approach. *Insight-Non-Destructive Testing and Condition Monitoring*, 52(10):553–560, 2010. 3, 75

- C. Senalik. *Detection and assessment of wood decay—glulam beams and wooden utility poles*. PhD thesis, University of Illinois at Urbana-Champaign, 2013. x, 25, 26, 36
- W. Shangguan, H. Ren, J. Lv, B. Fei, Z. Chen, R. Zhao, and Y. Zhao. Cell wall property changes of white rot larch during decay process. *BioResources*, 9(3):4297–4310, 2014. 86
- C. E. Shannon. Communication in the presence of noise. *Proceedings of the IRE*, 37(1): 10–21, 1949. 72
- R. Shmulsky and P. D. Jones. *Forest products and wood science: an introduction*. John Wiley & Sons, 2019. 14
- H. Suzuki, E. Sasaki, et al. Effect of grain angle on the ultrasonic velocity of wood. *Journal of the Japan Wood Research Society*, 36(2):103–107, 1990. 3, 22
- R. Szymani and K. A. McDonald. Defect detection in lumber: state of the art. *Forest Products Journal*, 31(11):34–44, 1981. 21
- G. L. Taggart, S. J. Phifer, J. A. Nixon, and M. Wood. *Rubrics: A handbook for construction and use*. R&L Education, 1999. 69
- F. Tallavo, G. Cascante, and M. D. Pandey. A novel methodology for condition assessment of wood poles using ultrasonic testing. *Ndt & E International*, 52:149–156, 2012. 36
- K. Uchino. Piezoelectric ceramics for transducers. In *Ultrasonic Transducers*, pages 70–116. Elsevier, 2012. x, 29, 31, 41, 59
- J. Ultrasonics. Industrial applications of ultrasound—a review ii. measurements, tests, and process control using low-intensity ultrasound. *IEEE Transactions on sonics and Ultrasonics*, 1975. 27

- I. A. Viktorov. *Rayleigh and Lamb Waves: Physical Theory and Applications. Transl. from Russian. With a Foreword by Warren P. Mason.* Plenum press, 1967. 4, 42, 75, 77
- X. Wang, F. Divos, C. Pilon, B. K. Brashaw, R. J. Ross, and R. F. Pellerin. Assessment of decay in standing timber using stress wave timing nondestructive evaluation tools: A guide for use and interpretation. *Gen. Tech. Rep. FPL-GTR-147. Madison, WI: US Department of Agriculture, Forest Service, Forest Products Laboratory, 2004. 12 pages, 147, 2004.* 35
- C. Wassilieff. Sound absorption of wood-based materials. *Applied Acoustics*, 48(4):339–356, 1996. 58
- E. L. Wilson. Structural analysis of axisymmetric solids. *Aiaa Journal*, 3(12):2269–2274, 1965. 25
- J. E. Winandy and J. J. Morrell. Relationship between incipient decay, strength, and chemical composition of douglas-fir heartwood. *Wood and Fiber Science*, 25(3), 1993. x, 20, 35, 80
- J. E. Winandy, C. A. Clausen, and S. F. Curling. Predicting the effects of decay on wood properties and modeling residual service-life. In *Proc. 2nd annual conference on durability and disaster mitigation in wood-frame housing, Forest Products Society, Madison, WI*, pages 261–263, 2000. 17
- P. M. Winistorfer, W. Xu, and R. Wimmer. Application of a drill resistance technique for density profile measurement in wood composite panels. *Forest products journal*, 45(6): 90, 1995. 9
- R. Wolfe and R. Moody. Standard specifications for wood poles. *Morrell, JJ (Editor)*, 1997:6–7, 1997. 10

- R. W. Wolfe and R. C. Moody. Ansi pole standards: Development and maintenance. In *Proceedings of the first Southeastern pole Conference. For. Prod. Society. Madison, USA*, pages 143–149, 1994. 12
- A. Wyckhuysse and X. Maldague. A study of wood inspection by infrared thermography, part i: Wood pole inspection by infrared thermography. *Research in nondestructive evaluation*, 13(1):1–12, 2001. 9
- L. A. Zadeh. Fuzzy sets. *Information and control*, 8(3):338–353, 1965. 24
- H. Zhivomirov et al. On the development of stft-analysis and istft-synthesis routines and their practical implementation. *TEM Journal*, 8(1):56–64, 2019. xii, 91
- M. Zucker et al. X-ray pole inspection a new engineering tool. *Electrical World*, 113(12), 1940. 8



# Appendix A

## Navier's Equation for Elastic Model

The constitutive equation is the Navier's equations begins with the three-dimensional Hooke's law describing the linear elastic behaviors in solid. In the most general case for anisotropic medium, the Hooke's law is widely referred to as the stress-strain relation expressed using the index notation in the following,

$$\tau_{ij} = C_{ijkl}e_{kl}, \quad (\text{A.1})$$

where  $C$  is called the *Christoffel acoustic tensor*.  $\tau$  denotes the stress, and  $e$  denotes the strain. Since  $i, j, k, l$  range from one to three, the tensor contains eighty-one different elements characterizing material. For demonstrating the Navier's equation, we impose the isotropic assumption, which reduces the Christoffel tensor to only two scalar quantities.

$$C_{ijkl} = \lambda\delta_{ij}\delta_{kl} + 2\mu\delta_{jk}\delta_{il}, \quad (\text{A.2})$$

where  $\delta$  represents the Kronecker delta piece-wise function.  $\lambda$  and  $\mu$  are the Lamé constants. The isotropic simplification yields the following expression for (A.1),

$$\tau_{ij} = \lambda e_{kk}\delta_{ij} + 2\mu e_{ij} \quad (\text{A.3})$$

The constitutive equation for motion of any particle is the conservation of momentum

equation which is expressed in the following,

$$\frac{d}{dt} \iiint_V \frac{\partial u_i}{\partial t} \rho d\mathbf{x} = \iiint_V g_i \rho d\mathbf{x} + \iint_{\partial V} \tau_{ij} n_j da. \quad (\text{A.4})$$

As intimidating as it seems, the expression is another version of the familiar Newton's second law. Here,  $\rho$  is density,  $g$  represents any external bodily force,  $n$  is the unit normal vector ensure the effective component of the imposed stress and  $\tau$  is pointing at the direction of motion. Finally, the sum of the forcing contributes to the acceleration described by the first term. Using the divergence theorem and distribute the time derivative into the integrant, we arrive at the so-called *Cauchy's momentum equation* expressed as,

$$\rho \frac{\partial^2 u_i}{\partial t^2} = \rho g_i + \frac{\partial \tau_{ij}}{\partial x_j}, \quad (\text{A.5})$$

where the first term again is the acceleration term, the second term describes bodily forces, and the third term is the internal stresses within each differential element within the body. By differentiate (A.3) with respect to  $x_j$ , it yields,

$$\frac{\partial \tau_{ij}}{\partial x_j} = \lambda \delta_{ij} \frac{\partial e_{kk}}{\partial x_j} + 2\mu \frac{\partial e_{ij}}{\partial x_j}. \quad (\text{A.6})$$

By definition, the strain is expressed as,

$$e_{ij} = \frac{1}{2} \left( \frac{\partial u_i}{\partial X_j} + \frac{\partial u_j}{\partial X_i} + \frac{\partial u_k}{\partial X_i} \frac{\partial u_k}{\partial X_j} \right). \quad (\text{A.7})$$

In the elastic region when the displacement is *very small*, the quadratic contribution can be neglected yielding the following expression,

$$e_{ij} = \frac{1}{2} \left( \frac{\partial u_i}{\partial X_j} + \frac{\partial u_j}{\partial X_i} \right). \quad (\text{A.8})$$

Combining with the derived strain equation (A.8), (A.6) becomes,

$$\frac{\partial \tau_{ij}}{\partial x_j} = \lambda \delta_{ij} \frac{\partial^2 u_k}{\partial x_j \partial x_k} + \mu \frac{\partial^2 u_i}{\partial x_j \partial x_j} + \mu \frac{\partial^2 u_i}{\partial x_i \partial x_j}. \quad (\text{A.9})$$

In the first term, since the subscript  $k$  is a *dummy index*, (A.9) becomes,

$$\frac{\partial \tau_{ij}}{\partial x_j} = (\lambda + \mu) \frac{\partial^2 u_i}{\partial x_i \partial x_j} + \mu \frac{\partial^2 u_i}{\partial x_j \partial x_j}. \quad (\text{A.10})$$

By substituting (A.10) into the Cauchy's momentum equation (A.5), we arrive at the Navier's equation that describes the equation of motion describing motion of differential element within a solid volume when stresses are applied to the medium.

$$\rho \frac{\partial^2 u_i}{\partial t^2} = \rho g_i + (\lambda + \mu) \frac{\partial^2 u_i}{\partial x_i \partial x_j} + \mu \frac{\partial^2 u_i}{\partial x_j \partial x_j}. \quad (\text{A.11})$$

# Appendix B

## GL Signal Consistency Study

This appendix is to evaluate the consistency of the resulted AW3 characteristics, including the peak energy TOF and the energy level when the inspection process is repeated. It is a critical consideration, yet it is not the focus of this study. Hence, the information is placed here for the readers to examine the data reliability and the precision of characterizing the GL condition. The experiment is conducted in accordance with the following procedures:

- Determine the GL level by measuring vertically 2 inches above grade.
- Insert four waveguides at approximately 0, 90, 180 and 270 degrees around the pole circumference, as shown in Fig. B.1.
- Perform ten repeat measurements at 0-180 at the GL region. The repeat measurements were performed by unmounting and mounting the probes without altering the waveguide. This step is to evaluate effects of the entire process on the received raw signal characteristics.
- Perform another ten repeated measurements at 90-270.

The reason 0-180 and 90-270 configurations are used is that in the cross-section of the GL region of a healthy pole, the shell region material properties should be distributed homogeneously in the tangential direction. This concept is closely related to the orthotropic property of wood. The wave characteristics should be the same regardless of the location of the excitation and reception. Hence, the result of the assessment should be independent

of the absolute positions of the probes, but rather the relative positions of 180 degrees apart should be carefully maintained.

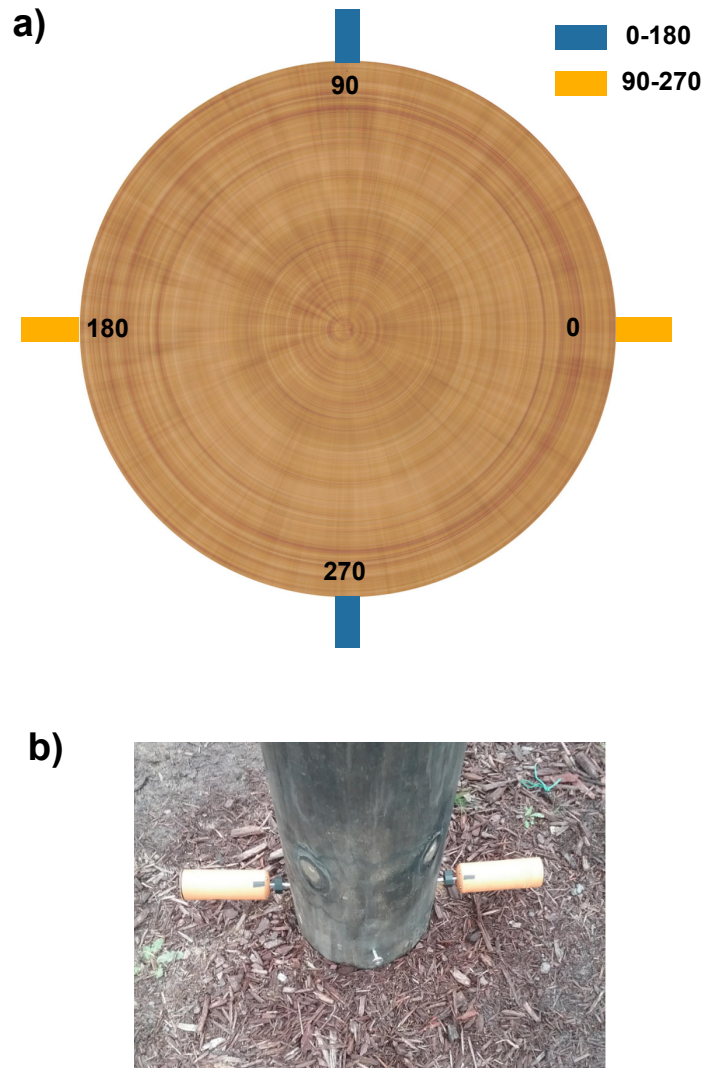


Figure B.1: Test Configuration from a) the top view and b) the actual setup.

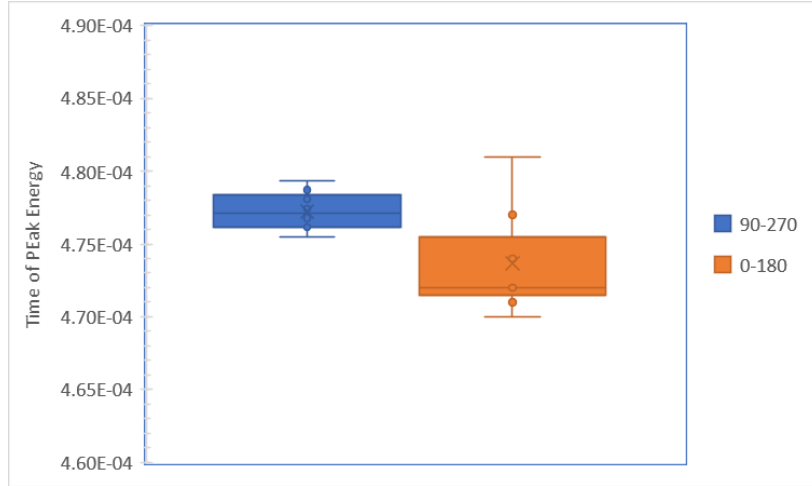
Statistical analysis of the extracted times at the energy peak and the peak energy values are depicted in box plots shown in Fig. B.2 a and b. In Fig. B.2a, the variation of 90-270 and 0-180 are different. The location of the median with respect to the standard deviation suggests that the 90-270 follows the Gaussian distribution, while the 0-180 exhibits left-skew distribution characteristics with a greater standard deviation and range (max. and

min). Based on the time scale, the relative difference of the average time values of the two configurations is only 2%. Since the latency of the TOF due to mechanical degradation is about 11%, statistically more significant than the 2% variation.

The variation in the energy domain of the two configurations is depicted in Fig. B.2b, the 90-270 has a smaller standard deviation, but it shows a greater span compared to the 0-180 configuration. By calculating the relative difference of the average energy response, the result is 20%. From the field data discussed in Chapter 6, the energy attenuation of at least 60% would be considered a potential mechanical degradation. The 20% could falsely identify a healthy pole. As mentioned in Chapter 2, the energy analysis of the waveform has become a challenge in many studies. One of the issues which it was not discussed is the hardware. The driving signal and the manufacturing tolerance of the transducers have not been thoroughly discussed due to the scope of this study. However, manufacturing process and a better feedback control of the full-bridge driving circuit can be an important research to further refine the UB1000 system.

By comparing the two configurations, it is apparent that the 90-270 configuration has a smaller variance than the 0-180. This can be explained by examining the signals generated from the two configurations. Theoretically, since the trajectory paths of AW3 of both configurations traveling are the same, the received waveform should be very similar. Using the proposed analysis technique, the resulted energy responses are shown in Fig. B.3. In the 0-180 configuration for GL dimension of 30 inches, the AW3 arrival region lies between 400 and 600  $\mu$ s. As expected, a peak occurs at around 500  $\mu$ s. In the 90-270 configuration in Fig. B.3b, there two peaks that lie within this region. This is quite possible that the two wavefronts are traveling circumferentially around the pole at different times due to imperfect geometric circular geometry, in-homogeneous material property and the imperfect 180-degree alignment. As a result, the two peaks interfere with each other. The interference pattern produces a smaller first peak and an enhanced second peak. In this situation,

a)



b)

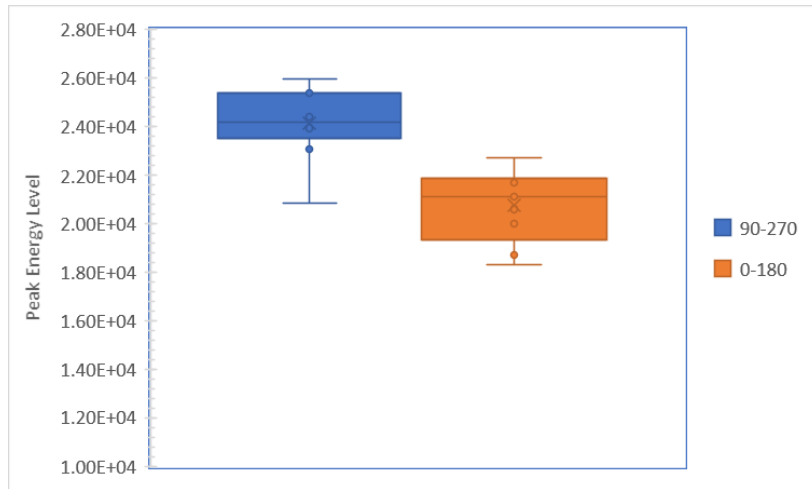


Figure B.2: Results from 10 different measurements.

the average time values of the two peaks are used to calculate the final time. However, the actual energy response is unable to recover unless a more advanced signal processing technique for signal decomposition is used. That is one of the primary reasons we see a much lower energy response in the 0-180 configuration in Fig. B.2. Nevertheless, this result establishes a certain level of confidence in the validity of the findings in this study.

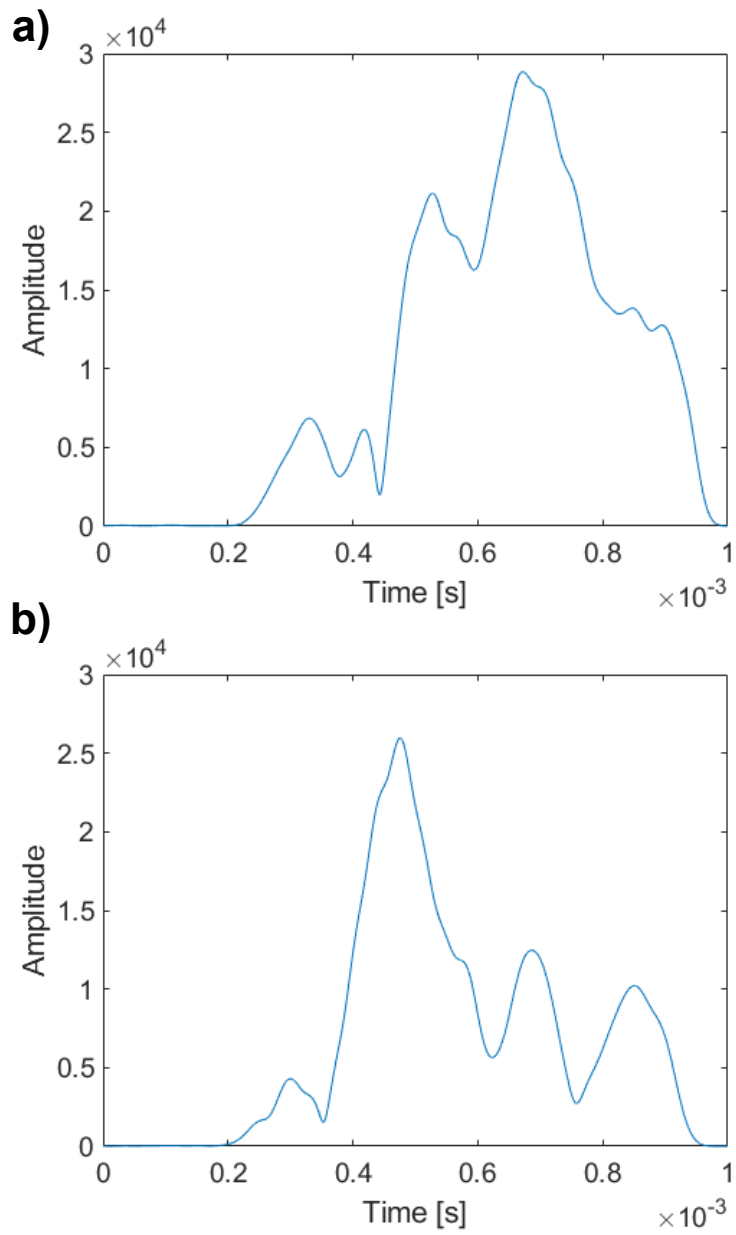


Figure B.3: Temporal energy response from a) 90-270 and b) 0-180